7-8-2024

# Optical Nonlinearities in Graphene Quantum Dots: High Harmonic Generation

Suresh Gnawali
*Georgia State University*

# Optical Nonlinearities in Graphene Quantum Dots: High Harmonic Generation

by

Suresh Gnawali

Under the Direction of Vadym Apalkov, Ph.D.

A Dissertation Submitted in Partial Fulfillment of the Requirements for the Degree of

Doctor of Philosophy

in the College of Arts and Sciences

Georgia State University

2024

ABSTRACT

The dissertation aims to study the light-matter interactions in graphene quantum dots (GQDs), investigating high-order harmonic generation (HHG), an extreme nonlinear frequency up-conversion process. We extended the study incorporating the variation of shape, size, geometry, and type of edges in GQD systems. We theoretically modeled the quantum dots system and developed the formulation employing quantum master equations and a density matrix approach. We explored ultrafast electron dynamics and optical nonlinearities in the system of GQDs, completing the four research projects: (i) Generation of high harmonics and its dependence on the relaxation process, (ii) HHG in triangular GQDs governed by edge states, (iii) Ellipticity dependence of HHG in GQDs (iv) HHG in GQDs with monovacancy or divacancy. We addressed nonlinearity in hexagonal GQDs placed in a short, linearly polarized optical pulse. At short finite dephasing times, the ultrafast electron dynamics show significant irreversibility with a significant residual population of the excited quantum dot levels. When dephasing time increases, intensities correspond to a low-frequency boost, while the cutoff energy decreases regarding the high harmonic spectra. In zigzag-edged triangular GQDs, the intensities of high harmonics show a strong dependence on the initial electron population of the edge states of the quantum dot. If a zigzag triangular quantum dot possesses an even number of edge states, then even high harmonics are strongly suppressed when half of the edge states of the quantum dots are populated before the pulse. The odd and even harmonics are of comparable intensities for any other populations of the edge states. The elliptically polarized ultrashort pulse interacts with the system of quantum dots to reveal unique nonlinear behavior different from the linearized polarized optical field. The generated high harmonics are sensitive to pulse ellipticity, frequency, amplitude, and GQDs' symmetry. Furthermore, we unraveled the influence of defects in HHG in GQDs with monovacancy or divacancy. Vacancy uplifts energy levels, provides additional channels

for multiphoton excitation, boosts even order harmonics, and disrupts symmetry-related suppression under circular polarization. These studies motivate the researchers to enhance, control, and optimize HHG in GQDs and other 2D materials.

INDEX WORDS: High-order harmonic generation, Nonlinear optics, Polarization of Light, Graphene, Quantum dots, Monovacancy, Divacancy

Optical Nonlinearities in Graphene Quantum Dots: High Harmonic Generation

by

Suresh Gnawali

Committee Chair: Vadym Apalkov

Committee: Unil Perera

Brian D. Thoms

Mukesh Dhamala

Electronic Version Approved:

Office of Graduate Services

College of Arts and Sciences

Georgia State University

August 2024

## DEDICATION

To my loving wife Mamta, son Suramya, daughter Manasha, and my Parents

## ACKNOWLEDGMENTS

I would like to express my sincere gratitude and appreciation to Professor Dr. Vadym Apalkov for his continuous guidance and support during the Ph.D. journey at Georgia State University. He has closely supervised this work through significant ideas, pertinent discussions, and recommendations. Under his supervision, I sharpened my critical thinking, problem-solving, and analytical skills. I am highly indebted to the Late Dr. Mark I. Stockman, whose guidance, instruction, and motivation prepared me as an independent researcher. My sincerest gratitude and thanks go to my committee members, Dr. Unil Perera, Dr. Mukesh Dhamala, and Dr. Brian Thoms, for their inquiry, constructive comments, and suggestions to prepare the current version of my dissertation for communicating the findings among the broad scientific community.

I thank Professors Dr. Murad Sarsour (Physics Graduate Director), Dr. Steven T. Manson, Dr. Sebastien Lepine (Chair of physics and astronomy), Dr. Gary Hastings, and all physics faculty members at GSU for enriching classes, motivating, and encouraging me. I thank my present and former research group members- Rupesh, Krishna, David, Aranyo, Jawad, Sayed, Fatemeh, Thakshila, Pardeep, Cody, Jhih-Sheng, Azar, and my friends Uttam, Sushma, Tara, Rameshwor, and Hemendra for their support and motivation during this journey.

Most importantly, my sincere gratitude goes to my parents and my entire family, including my wife, son, daughter, brothers, and sisters, for not just their endless love, prayers,

unwavering support, and constant encouragement but also for creating a supportive environment that allowed me to focus on my academic journey. Their unwavering support and constant encouragement have been the pillars of my educational journey, and I am grateful for having such a great, supporting, and motivating family.

# TABLE OF CONTENTS

# LIST OF TABLES

# LIST OF FIGURES

# CHAPTER 1
# CHAPTER 1 INTRODUCTION

## 1.1 Graphene

Graphene, an allotrope of carbon, consists of a single layer of atoms arranged in a two-dimensional honeycomb lattice with exceptional electronic, optical, mechanical, and thermal properties. It is one of the thinnest, lightest, and super strong materials. Graphene was first isolated and characterized by scientists Andre Geim and Konstantin Novoselov in 2004. They used a simple method of peeling off thin graphite flakes with sticky tape and then examined them under a microscope. They were awarded the Nobel Prize in Physics in 2010 for this groundbreaking discovery [1].

The electronic structure of an isolated carbon atom is $(1s)^2(2s)^2(2p)^2$. In a solid-state environment, the $1s$ electrons remain more or less inert, but the $2s$ and $2p$ electrons hybridize. One possible outcome is four $sp^3$ orbitals, which naturally tend to establish a tetrahedral bonding pattern that uses all the electrons: that is precisely what happens in the best solid form of C, namely diamond, which is an excellent insulator having a bandgap of around 5 $eV$. Another possibility is to form three $sp^2$ orbitals, leaving over a more or less pure $p$-orbital. In that case, the natural tendency is for $sp^2$ orbitals to arrange themselves in a plane at 120° angles, and the lattice thus formed is the honeycomb lattice.

The graphene hexagonal lattice comprises two interpenetrating triangular lattices, as shown in Fig. 3.1 [2]. Here, two inequivalent sublattices are in the environments of the corresponding atoms, which are mirror images of one another. It is convenient to express the

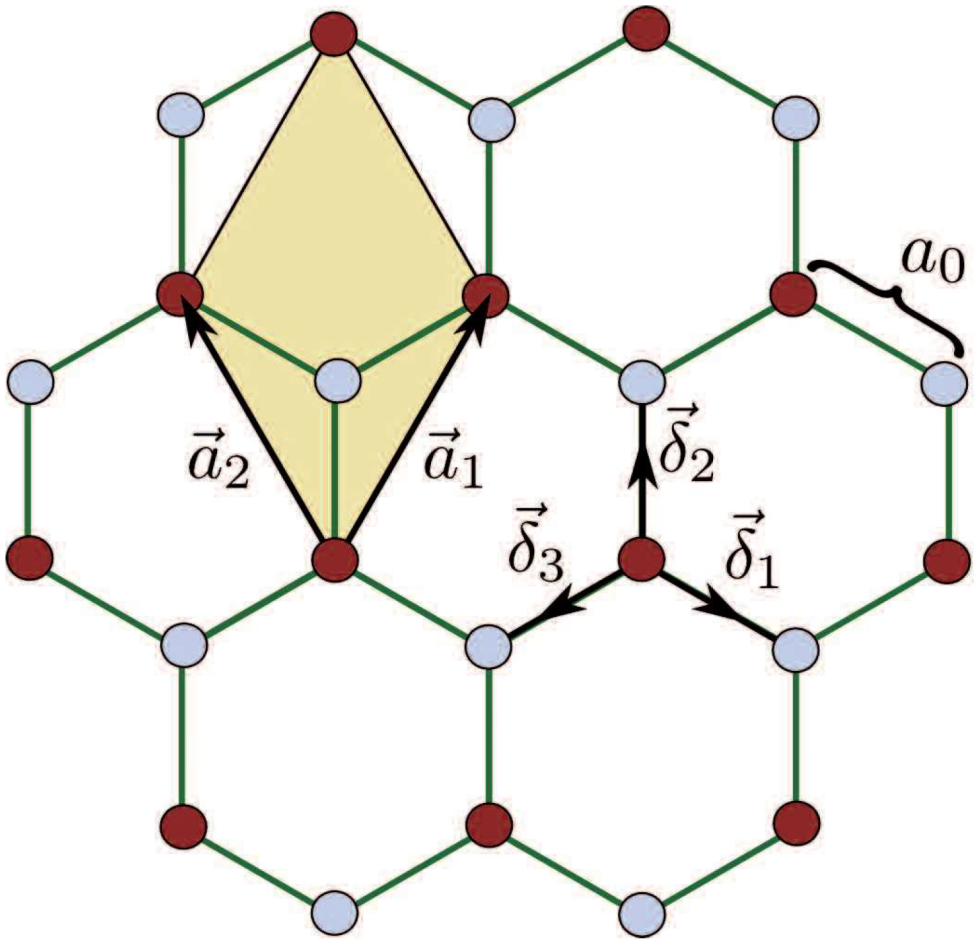


Figure 1.1 Graphene hexagonal lattice made of two interpenetrating triangular lattices. The nodes of each triangular lattice define the carbon atoms of type $A$ (red) and $B$ (blue). Arrows represent unit cell vectors $\vec{a_1}$ and $\vec{a_2}$.

Bravis lattice to have the primitive lattice vectors $\vec{a}_1$ and $\vec{a}_2$ with the notation in rectangular coordinates system by,

$$\mathbf{a}_1 = \frac{a}{2}(3, \sqrt{3}), \quad \mathbf{a}_2 = \frac{a}{2}(3, -\sqrt{3}), \tag{1.1}$$

where a is the nearest-neighbor carbon-carbon distance. The nodes of each triangular lattice define the carbon atoms of type A (red) and B (blue). Arrows represent unit cell

vectors $\mathbf{a}_1$ and $\mathbf{a}_2$. The reciprocal lattice vectors $\mathbf{b}_1$ and $\mathbf{b}_2$ defined by the condition $\mathbf{a}_i \cdot \mathbf{b}_j = 2\pi\delta_{ij}$ are given by

$$\mathbf{b}_1 = \frac{2\pi}{3a}(1, \sqrt{3}), \quad \mathbf{b}_2 = \frac{2\pi}{3a}(1, -\sqrt{3}). \tag{1.2}$$

We define the first Brillouin Zone (FBZ) of the reciprocal lattice in the way bounded by the planes bisecting the vectors to the nearest reciprocal lattice points representing the FBZ similar to hexagons of honeycomb lattice but rotated by $\pi/2$ as shown in Fig. 1.2 [3].

It is often convenient to express for $A$-sublattice atom by three nearest-neighbor vectors in real space given by

$$\delta_1 = \frac{a}{2}(1, \sqrt{3}), \quad \delta_2 = \frac{a}{2}(1, -\sqrt{3}), \quad \delta_3 = -a(1, 0). \tag{1.3}$$

Those vectors for $B$-sublattice are the negatives of Eq.(1.3).

We can study the electronic band structure by a tight binding approach with the nearest neighbor hopping. If we denote the orbital on atom $i$ with spin $\sigma$ by $(i, \sigma)$, and the corresponding creation operator by $a^\dagger_{i\sigma}(b^\dagger_{i\sigma})$ for an atom on the $A(B)$ sublattice, then the nearest -neighbor tight-binding Hamiltonian in the form

$$H_{TB,nn} = -t \sum_{<ij>} (\hat{a}^\dagger_{i\sigma} \hat{b}_{j\sigma} + h.c.), \tag{1.4}$$

where $t$ is the nearest-neighbor hopping matrix element $\approx 2.8$ eV.

Let us include the tight binding eigenfunctions in the form of spinor, whose components

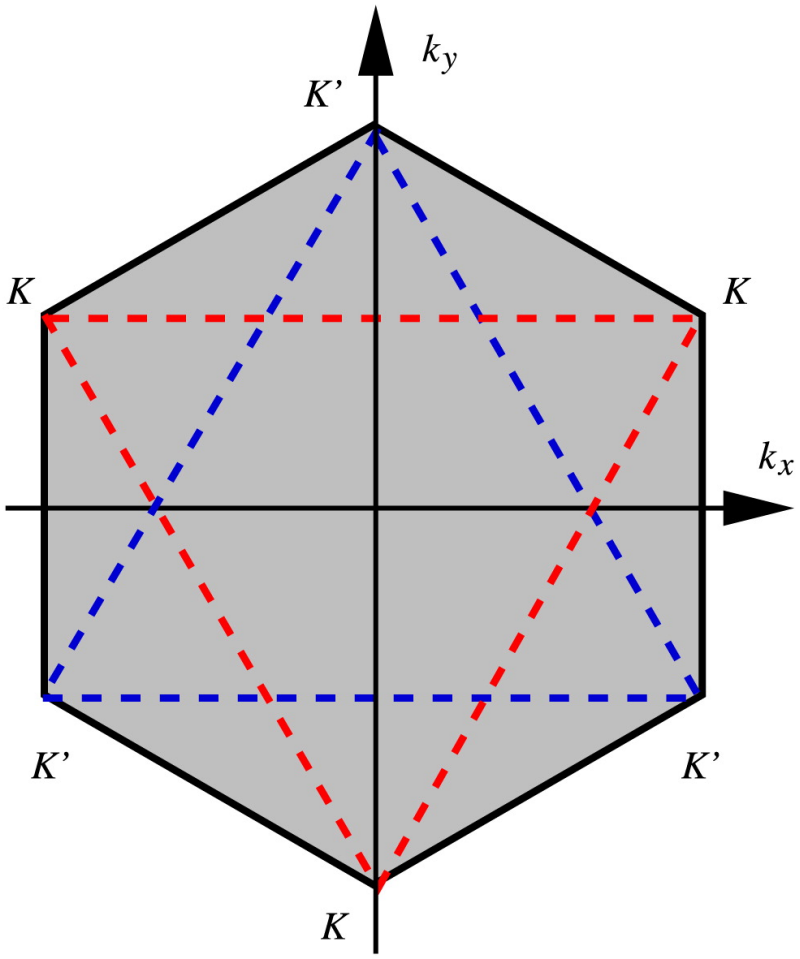


Figure 1.2 The FBZ of the graphene. The Dirac cones are located at the corners of the Brillouin zone. The six cones can be divided into two equivalent classes (cones within the same class are connected by dashed lines). These classes are commonly referred to as $K$ and $K'$.

correspond to the amplitudes on the $A$ and $B$ atoms, respectively, from a reference point $\mathbf{R}_i^0$

$B$ separated from $A$ by $\delta_i$ and $R_i$ at the position have the form given by

$$\begin{pmatrix} \alpha_{\mathbf{k}} \\ \beta_{\mathbf{k}} \end{pmatrix} = \sum_i exp\ i\mathbf{k}\cdot\mathbf{R}_i^0 \begin{pmatrix} a_i^\dagger e^{-i\mathbf{k}\cdot\delta_1/2} \\ b_i^\dagger e^{i\mathbf{k}\cdot\delta_1/2} \end{pmatrix} \tag{1.5}$$

where $b_i^\dagger$ creates an electron on the $B$ atom in cell $i$. The exponential factor $e^{i\mathbf{k}\cdot\delta_1/2}$ intro-

duced in spinor to simplify the subsequent expressions. The Hamiltonian in **k**-representation is purely off-diagonal in this representation

$$H_{\mathbf{k}} = \begin{pmatrix} 0 & \Delta_{\mathbf{k}} \\ \Delta^*_{\mathbf{k}} & 0, \end{pmatrix}, \quad \Delta_{\mathbf{k}} \equiv -t \sum_{l=1}^{3} exp\ i\mathbf{k} \cdot \delta_l. \tag{1.6}$$

Using Eq.(1.3) the nearest neighbor vectors $\delta_l$ becomes

$$\Delta_{\mathbf{k}} = -t\ exp\ ik_x a \left(1 + 2\ exp(i\frac{3k_x a}{2} cos\frac{\sqrt{3}}{2} k_y a\right), \tag{1.7}$$

and the eigenvalues $\epsilon_{\mathbf{k}}$ are given by

$$\epsilon_{\mathbf{k}} = \pm|\Delta_{\mathbf{k}}| = \pm - t \left(1 + 4cos\frac{3k_x a}{2} cos\frac{\sqrt{3}}{2} k_y a + 4cos^2\frac{\sqrt{3}}{2} k_y a\right)^{1/2}, \tag{1.8}$$

We are interested in instigating whether there are any values of **k** for which $\Delta_{\mathbf{k}}$ (hence $\epsilon_{\mathbf{k}}$) is zero, Any such states must satisfy

$$\frac{3K_x a}{2} = 2n\pi, \quad cos\frac{\sqrt{3}}{2} k_y a = -\frac{1}{2} \quad \text{or} \frac{3K_x a}{2} = 2(n+1)\pi, \quad cos\frac{\sqrt{3}}{2} k_y a = \frac{1}{2}. \tag{1.9}$$

Here, the first choice takes $k_y$ outside the FBZ while the second option ($n = 0$) exactly defines the corner points **K** and **K′** called the Dirac points. To discuss the nature of the energy spectrum and eigenfunctions for **k** close to a Dirac point, for instance, **K** it is convenient to define a 2D vector $\mathbf{k} - \mathbf{K}$ as **q** and expanding the expression around $\mathbf{q} = 0$, we get

$$\Delta(\mathbf{q}) = -2t\ e^{ik_x a}\mathbf{q}\cdot\nabla_{\mathbf{k}}\left(e^{(}i\frac{3k_x a}{2}cos\frac{\sqrt{3}}{2}k_y a\right)_{\mathbf{k}=\mathbf{K}} = -\frac{3ta}{2}exp(-iK_x a)(iq_x - q_y). \quad (1.10)$$

Extracting the constant factor $-iexp(-iK_x a)$ we write

$$\Delta(\mathbf{q}) = \hbar\upsilon_F(iq_x - q_y), \upsilon_F \equiv 3ta/2\hbar \cong 10^6 m/s. \quad (1.11)$$

If we expand around $\mathbf{K}$ for which $K'_x = K_x, K'_y = -K_y$ we find

$$\Delta_{K'}(\mathbf{q}) = \hbar\upsilon_F(iq_x - q_y) = \Delta^*_K(\mathbf{q}), \quad (1.12)$$

Now, we define the Hamiltonian in the following form,

$$H_{\mathbf{k}} = \begin{pmatrix} 0 & q_x + iq_y \\ q_x - iq_y & 0 \end{pmatrix}, \quad \equiv \hbar\upsilon_F\sigma\cdot\mathbf{q}, \quad \hat{\epsilon}(q) = \pm\upsilon_F|q|. \quad (1.13)$$

Here, the components of the operator $\hat{\epsilon}$ are the Pauli matrices. Also, the eigenvalues depend only on the magnitude of $\mathbf{q}$. The corresponding eigenfunctions obtained are expressed as

$$\psi^{\pm}_K(\mathbf{q}) = \frac{1}{sqrt2}\begin{pmatrix} exp(i\theta_{\mathbf{q}/2}) \\ \pm exp(i\theta_{\mathbf{q}/2}) \end{pmatrix}, \quad \theta_{\mathbf{q}} \equiv tan^{-1}(q_x/q_y). \quad (1.14)$$

When $\mathbf{q}$ rotates around the Dirac point, the phase of $\psi^{\pm}_K(\mathbf{q})$ changes by $\pi$, not by $2\pi$, as is the characteristics of spin-half particles.

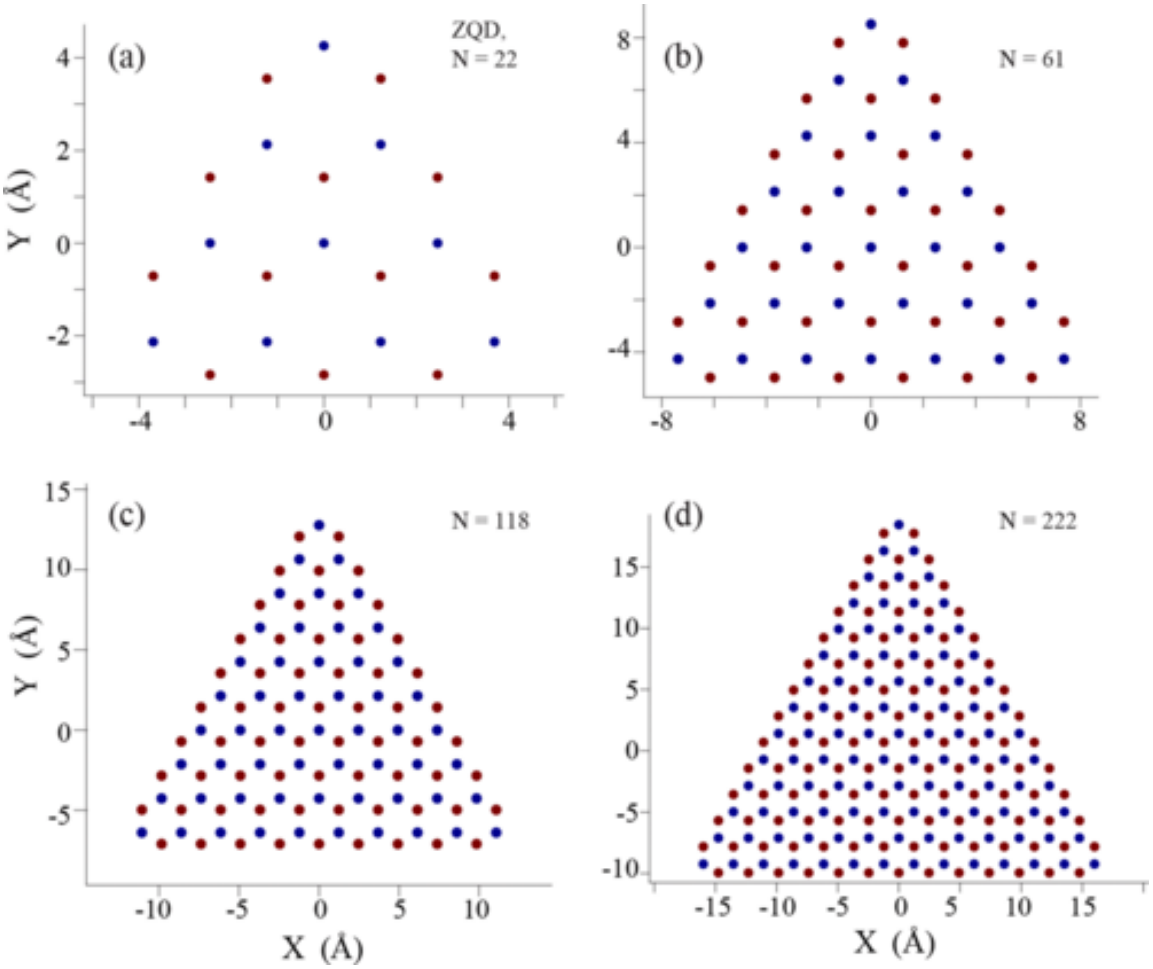


Figure 1.3 Typical zigzag-edged triangular GQDs with different numbers of atoms. The corresponding numbers of atoms are depicted in each panel.

### 1.2 Graphene quantum dots (GQDs)

Graphene Quantum Dots (GQDs) are graphene nanoparticles of finite size (a few nanometers to 100 nanometers) containing a finite number of graphene nanoparticles. They can have different shapes, sizes, edges, and geometry, significantly changing their optical and electronic properties. Typical GQDs of triangular shapes with zigzag edges having different numbers of dots are shown in Fig. 1.3 [4].

## 1.3 Ultrafast lasers

Over the past decade, ultrafast lasers, which generate ultrashort optical pulses in the orders of femtoseconds, have progressed from complicated and specialized laboratory systems to compact, reliable instruments suitable for a wide range of applications [5; 6]. With their ability to produce high-power peaks, these lasers are helpful in diverse fields, such as spectroscopy, material processing, signal processing, diagnostic imaging, and radiation therapy [7; 8; 9]. Their versatility and adaptability are a testament to their potential in shaping the future of these fields. The advancement of the fastest process has been the subject of several Nobel prizes. In 1999, Ahmed Zewail was honored for his work in femtosecond spectroscopy to measure the real-time motion of atomic nuclei. Pierre Agostini, Anne L'Huillier, and Frenec Krausz shared the Nobel prize two dozen years later for recognition for bringing the attosecond regime- the natural unit of time 1000 times faster than femtoseconds under experimental control. One facet of this research is that attosecond-scale light pulses could be made and characterized with ordinary tabletop experiments.

Lasers that generate intense, coherent beams of light enable us to investigate the fastest processes in condensed matter physics, such as phase transitions, structural electron and molecular dynamics, and chemical reactions [10; 5; 11].

## 1.4 Light matter interaction

Light-matter interaction is vital in many areas, such as laser, spectroscopy, quantum information processing, light-emitting diodes and solar cells, biological structures like photosystem

II, potential quantum devices, and sensing [12; 13; 14]. In the background of the physics of light, optical resonators and light-matter interactions, including absorption, emission, transmission, reflectance, and polarization, are essential both in classical and quantum physics. The absorption or emission of light is predominant on a subnanometer scale, typically coupling light into or extracting light from the tunnel junction [12]. Electromagnetic radiation couples with matter through the interaction with charge carriers, leading to excitons such as electronic or optical transitions. This section briefly discusses the light-matter interaction, focusing on the two-level system.

An electric dipole $e\mathbf{r}$ is an essential observable in light-matter interaction, which provides the bridge between the quantum mechanical description of the system and the polarization of the medium $\mathbf{P}$ used as a source in Maxwell's equations for the electromagnetic field. The expectation value of $e\mathbf{r}$ is given by,

$$\langle e\mathbf{r}\rangle = \int d^3r \ \mathbf{r} \ e| \ \psi(\mathbf{r},t) \ |^2. \tag{1.15}$$

In nonrelativistic quantum mechanics, the evolution of $\psi(\mathbf{r},t)$ is governed by the Schrodinger equation

$$i\hbar\frac{\partial}{\partial t}\psi(\mathbf{r},t) = H\psi(\mathbf{r},t), \tag{1.16}$$

where $H$ is the Hamiltonian of the system and $\hbar = 1.054 \times 10^{-34}$ joule-seconds. The Hamiltonian of an unperturbed system is the sum of its potential and kinetic energies

$$H = \frac{p^2}{2m} + V(\mathbf{r}), \tag{1.17}$$

where $p$,$m$, and $V(\mathbf{r})$ are the system momentum, mass, and potential energy. The time and space dependencies in Eq.(1.17) can be separated as

$$\psi(\mathbf{r}, t) = u_n(\mathbf{r})\ e^{-i\omega_n t} \tag{1.18}$$

for which the $u_n(\mathbf{r})$ satisfy the energy eigenvalue equation

$$H(\mathbf{r}) = \hbar\omega_n u_n(\mathbf{r}). \tag{1.19}$$

The eigenfunctions $u_n(\mathbf{r})$ can be shown to be orthonormal and complete, which provides the basis to write the function as a superposition of the $u_n(\mathbf{r})$. In particular, the wavefunction $\psi(\mathbf{r}, t)$ itself can be written as the superposition

$$\psi(\mathbf{r}, t) = \sum_n C_n(t)\ u_n(\mathbf{r})\ e^{-i\omega_n t}. \tag{1.20}$$

Here the expansion coefficients $C_n(t)$ are constants for the problem described by a Hamiltonian satisfying the eigenvalue Eq. (1.19). We include the time dependence in anticipation of adding interaction energy to the Hamiltonian. The modified Hamiltonian wouldn't quite satisfy Eq. (1.19), thereby causing the $C_n(t)$ to change in time.

The Eq. (1.20) satisfies the normalization condition using the orthonormality of $u_n(\mathbf{r})$.

Therefore, $C_n^2$ can be interpreted as the probability that the system is in the $n$th energy state. The $C_n$ are complex probability amplitudes that can completely determine the wave function. In terms of the $C_n(t)$ the expectation value of the operator $\theta$ is given by

$$\langle\theta\rangle = \sum_n \sum_m C_n(t)\ u_n(\mathbf{r})\ e^{-i\omega_n t}\theta_{mn}, \tag{1.21}$$

where $\theta_{mn}$ is the matrix elements $\int d^3r\ u_m^*(r)\theta\ u_n(r)$.

To address the light-matter-interaction, we add appropriate interaction energy to the Hamiltonian, that is

$$H = H_0 + V \tag{1.22}$$

Expanding the wavefunction in terms of the wavefunctions of the unperturbed Hamiltonian, the probability amplitudes $C_n(t)$ change in time. Substituting the wavefunction (1.20) and Hamiltonian (1.22) into Eq. (1.16) we get

$$\dot{C}_n(t) = -\frac{i}{\hbar}\sum_m < n|V|m > e^{-i\omega_{mn}t}\ C_m(t), \tag{1.23}$$

where the $< n|V|m >$ and $\omega_{mn}$ are the interaction energy matrix element and frequency difference.

The First-order-perturbation theory can solve Eq. (1.23) approximately. The interaction energy matrix element has a time-dependent form

$$< n|V|m >= V_{nm}(0)\ cos(\omega_0 t), \tag{1.24}$$

where $\omega_0$ is an optical frequency. At time $t = 0$ the system is in the initial level $i$ with $(C_i(0) = 1, C_{m\neq i}(0) = 0))$, we integrate Eq. (1.23) with $C_m(t) \simeq C_m(0)$ to find

$$C_n(t) \simeq C^(1)_n(t) = -i\frac{V_{ni}(0)}{2\hbar}\left[\frac{e^i(\omega_{ni}+\omega_0)t-1}{i(\omega_{ni}+\omega_0)} + \frac{e^i(\omega_{ni}-\omega_0)t-1}{i(\omega_{ni}-\omega_0)}\right]. \tag{1.25}$$

The superscript (1) says the interaction energy is first in order. For the case $\omega_{ni} > 0$, the denominator $\omega_{ni}+\omega_0)$ is always positive and larger than $\omega_{ni}$. This is not case for denominator $\omega_{ni} - \omega_0)$ which vanishes if the resonance condition

$$\omega_0 \simeq \omega_{ni} \tag{1.26}$$

is satisfied. For interactions near resonance, the term with a relatively small denominator $(\omega_{ni} - \omega_0)$ is larger than that with $(\omega_{ni} + \omega_0)$, allowing us to neglect the latter, an approximation known as rotating wave approximation (RWA).

### *1.4.1 Two-level approximation*

We can neglect transitions to levels with energies very different from $\omega_0$; for two-level approximation, we neglect all except two levels, those satisfying Eq.(1.26).In this case, the wavefunction in Eq.(1.20) reduces to

$$\psi(\mathbf{r}, t) = C_a(t)e^{-i\omega_a t}u_a((r)) + C_b(t)e^{-i\omega_b t}u_b((r)). \tag{1.27}$$

According to Eq. (1.23), the probability amplitudes obey the equations of the motion

$$\dot{C}_a(t) = -\frac{i}{\hbar}V_{ab}\ e^{-i\omega t}C_b, \tag{1.28}$$

$$\dot{C}_b(t) = -\frac{i}{\hbar} V_{ba}\ e^{i\omega t} C_a, \tag{1.29}$$

where the transition frequency $\omega \equiv \omega_{ab}$.

### *1.4.2 Electric-Dipole Interactions*

The electric dipole operator serves two important tasks: (i) provides the link between Maxwell's equations and (ii) yields the light-matter interaction energy $V$. The light-matter interaction energy is

$$V = -e\mathbf{r} \cdot \mathbf{E}(\mathbf{R}, t), \tag{1.30}$$

where $\mathbf{R}$ is the position of the center of mass of the dipole. In Eq.(1.31), we approximated $\mathbf{E}(\mathbf{r}, t)$ by $\mathbf{E}(\mathbf{R}, t)$ since our focus is in electromagnetic fields with wavelengths much larger than atomic dimensions. Therefore, we can approximate the electric field by a constant over the dimension of the dipole. This approximation is popularly termed as dipole approximation. Then, we can write the electric-dipole interaction energy matrix elements as

$$V_{ab} = -\wp \mathbf{E}(\mathbf{R}, t), \tag{1.31}$$

where $\wp$ is the component of $e\mathbf{r}_{ab}$ along $\mathbf{E}$. For simplicity, we ignore the spatial dependence and use the electric field

$$\mathbf{E}(t) = \mathbf{E_0}\ cos(\omega_0 t),$$

which gives the interaction energy matrix element

$$V_{ab} = -e\wp\mathbf{E_0}\ cos(\omega_0 t). \tag{1.32}$$

In Eqs.(1.32) and (1.25) in RWA we keep the term $e^{-i\omega_0 t}$ term for $\omega_{ni} > 0$. Here, $\omega \equiv \omega_{ab} > 0$ and hence in RWA we keep only

$$V_{ab} \simeq -\frac{1}{2}\ \wp\mathbf{E_0}e^{-i\omega_0 t}, \tag{1.33}$$

and $V_{ba} = {V_{ab}}^*$. For the exact resonance, i.e., $\omega_0 = \omega$, substituting the complex conjugate of Eq.(1.33) into Eq.(1.29),differentiating with respect to time, and substituting Eq.(1.28),we get

$$\ddot{C_b} = -\frac{1}{4}{R_0}^2 C_b, \tag{1.34}$$

where $R_0$ is the Rabbi flopping frequency

$$R_0 = \frac{\wp\mathbf{E_0}}{\hbar} \tag{1.35}$$

after Rabi. Eq.(1.34) is a differential equation for sinusoids. If at time $t = 0$ the system is in the lower state $(C_b(0) = 1, C_a(0) = 0))$, then

$$C_b(t) = cos\frac{1}{2}R_0 t, \tag{1.36}$$

which from Eq.(1.36) gives

$$C_a(t) = isin\frac{1}{2}R_0t. \tag{1.37}$$

The probability that the system is in the lower level $|C_b(t)|^2 = cos^2\frac{1}{2}R_0t = (1+cosR_0t)/2$, while $|C_a(t)|^2 = sin^2\frac{1}{2}R_0t = (1-cosR_0t)/2$. Thus, the wave function oscillates sinusoidally between the lower and upper states at the frequency $R_0$, a phenomenon known as Rabi flopping.

## 1.5 High harmonic generation (HHG)

High harmonic generation (HHG) is a highly nonlinear frequency upconversion process in which intense radiation of a specific frequency converts into a series of high-order harmonics through ionization and collision processes. In this phenomenon, the incident light of frequency $\omega_0$ is used to produce new frequencies integral multiples of the frequency of incident light. As the process is coherent, it is a prerequisite of attosecond and femtosecond physics. The nonlinear plasmonics in nanographene with the generation of high harmonics reported by the researcher is shown in Fig. 1.4 [15].

HHG in gases is a well-studied research area, as evidenced by significant research publications within a short period. In addition to gases, HHG is studied in atoms, crystals, solids, and even liquids today. The typical HHG process in atoms includes a three-step process: tunnel ionization, where the incident light overcomes the coulomb forces to knock out the electrons, acceleration of the carrier, and recombination of the ion to its original atom, resulting in the emission of radiation [16; 17; 18]. The typical solid state and atomic HHG

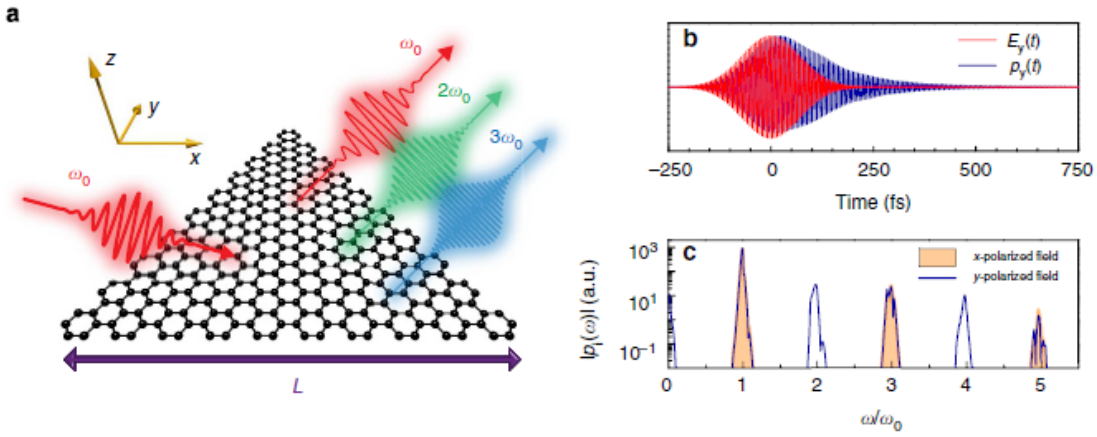


Figure 1.4 Nonlinear response of nanographene. (a) Illustration of doped nanotriangle (the armchair edge with 330 carbon atoms, L=4.1 nm side length, doped with Q=2 additional charge carriers) irradiated by short optical pulse (166 full width at half maximum (FWHM) duration, $10^{12} Wm^{-2}$ peak intensity, $\omega_0 = 0.68$ eV) tuned to one of the graphene plasmons. (b) Time variations of the incident electric field and the induced graphene dipole. (c) Harmonic analysis of the graphene dipole for polarizations along $x$ and $y$ directions.

process is shown in which is depicted in Fig. 1.5 described in ref. [19]. In this dissertation, We will study the HHG process in detail.

The rest of the dissertation is organized as follows: Chapter 2 discusses the theoretical formulation. Chapter 3 explains the generation of harmonics and delves further into the relaxation process. Chapter 4 investigates the HHG in triangular GQDs governed by the presence of edge states. Chapter 5 studies the HHG in the elliptically polarized optical pulse pulse field. Chapter 6 explores the HHg in GQD with vacancies, particularly monovacancy and divacancy. We summarize the essential results in Chapter 7.

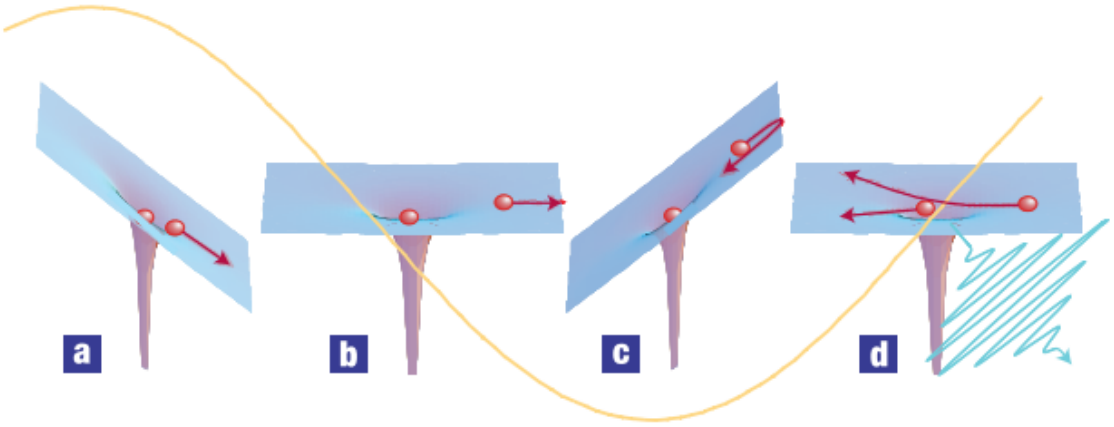


Figure 1.5 Three step model for HHG prcess. Initially, an electron is pulled away from the atom, overcoming Coulomb's force (a and b); the electron is driven back in a parabolic field after the field reverses (c), where the electron can recollide during a small fraction of the laser oscillation cycle to emit the photon

# CHAPTER 2

# CHAPTER 2 METHODOLOGY

## 2.1 Theoretical Formulation

This chapter is devoted to theoretical formulation. Here, theoretical formulation involves introducing the density matrix, writing the time-dependent Hamiltonian of the system, incorporating tight-binding Hamiltonian to describe the neutral QD system and external perturbation Hamiltonian as an ultrafast optical pulse using dipole approximation, deriving the density matrix equations, and obtaining expressions for finding the Dipole moment and intensity of high harmonics for the GQDs system of exploration.

### *2.1.1 Density matrix*

According to the postulates of quantum mechanics, the wavefunction $\psi(\mathbf{r}, t)$ provides the best possible knowledge about a single quantum system. Although $\psi(\mathbf{r}, t)$ has no direct physical meaning, it allows us to calculate the expectation values of all observables of interest. To study the laser media, we must consider the ensembles of the quantum systems involving pumping and damping, which are inherently irreversible processes, unlike the processes entirely determined by the Schrodinger equation. Although some limited examples of decay processes can be described using wavefunctions, they cannot address the two essential kinds that frequently occur in semiconductors: level probability decay, which involves decay from upper to lower levels, and dipole decay, which describes the decay of electric dipole processes. As the pumping processes are incoherent and only level probabilities are

pumped, we need a more general description to address the partial incoherent superposition in quantum systems involving these pumping and dephasing mechanisms. The density matrix provides the quantum system's most general quantum mechanical description to address these situations[20; 21; 22].

The density matrix is formally defined as the outer product of the wavefunction and its conjugate,

$$\rho = |\psi(t)\rangle\langle\psi(t)|. \tag{2.1}$$

The Eq.(2.1) represents the pure state density. For a complex system involving mixed states described in terms of an ensemble average of pure states, we need to consider all the possible states under the study. In this case, we define the mixed state density matrix as a convex sum (weighted with sum with $\sum_i p_i = 1$) of the pure states density matrix,

$$\rho_{mix} = \sum_i p_i \rho_i^{pure} = \sum_i p_i |\psi(t)\rangle\langle\psi(t)|. \tag{2.2}$$

.

In the following section, We will highlight important properties of the density matrix.

*2.1.1.1 Properties of density matrix*

The density matrix has the following important properties.

1)

$$\rho^*{}_{nm} = \rho_{mn} \quad (Hermiticity). \tag{2.3}$$

2)

$$\rho^2 \begin{cases} = \rho, & \text{for pure states} \\ \neq \rho, & \text{for mixed states} \end{cases} \tag{2.4}$$

3)

$$\rho^*{}_{nm} = \rho_{mn} \quad (Hermiticity). \tag{2.5}$$

4)

$$Tr(\rho) = 1 \quad (Normalization). \tag{2.6}$$

5)

$$\rho \geq 0 \quad (Positivity). \tag{2.7}$$

6)

$$Tr(\rho^2) \begin{cases} = 1, & \text{for pure states} \\ > 1, & \text{for mixed states} \end{cases} \tag{2.8}$$

*2.1.1.2 Time evolution of density matrix*

Time evolution of density matrix Consider a physical system with a wavefunction $\psi(\mathbf{r}, t)$ which satisfies the equation

$$i\hbar \frac{\partial \psi}{\partial t} = H\psi, \tag{2.9}$$

Let $\psi(\mathbf{r})$ be a complete set of orthonormal time-independent functions. In the Schrodinger representation, we may write

$$\psi(\mathbf{r},t) = \sum_k a_k(t) H\psi_k(\mathbf{r}), \tag{2.10}$$

Then equation (2.9) can be written as follows

$$i\hbar \sum_k \dot{a}_k \psi_k = \sum_k a_k H\psi_k, \tag{2.11}$$

If we multiply by $\psi_m^*$ on the left hand of each term and integrate over the space coordinates, we obtain

$$i\hbar \dot{a}_m = \sum_k a_k H_{mk}, \tag{2.12}$$

Similarly,

$$i\hbar \dot{a}_n = \sum_k a_k H_{nk}, \tag{2.13}$$

Consider the following,

$$\frac{d}{dt}(a_m a_n^*) = \dot{a}_m a_n^* + a_m \dot{a}_n^*, \tag{2.14}$$

$$\begin{aligned}\frac{d}{dt}(a_m a_n^*) &= \dot{a}_m a_n^* + a_m \dot{a}_n^* \\ &= \sum_k H_{mk}(a_k a_n^*) + a_m(\frac{1}{i\hbar}\sum_k a_k H_{nk})^* \\ &= \frac{1}{i\hbar}\sum_k \Big(H_{mk}(a_k a_n^*) - (a_m a_k^*)H_{kn}\Big), \end{aligned} \tag{2.15}$$

Let,

$$\rho = a_m a_n^*, \tag{2.16}$$

then,

$$\dot{\rho}_{mn} = \frac{i}{\hbar}\sum_k (\rho_{mk}H'_{kn} - H'_{mk}\rho_{kn}). \tag{2.17}$$

.

In general,

$$\frac{d\rho}{dt} = \frac{i}{\hbar}\left[\rho, H\right], \tag{2.18}$$

represents the time evolution of the density matrix. This equation is also called the Liouville-Von-Neumann equation. It is isomorphic to the Heisenberg equation of motion for internal variables since $\rho$ is also an operator.

### *2.1.2 Formulation of Hamiltonian*

The system of a GQD placed in the field of a short optical pulse is described by the time-dependent Hamiltonian of the following form

$$H(t) = H_0 + H'(t), \tag{2.19}$$

where $H_0$ is the field-free Hamiltonian that describes the GQD system within the scope of the tight-binding model,

$$H_0 = -t \sum_{<ij>} (\hat{c}_i^\dagger \hat{c}_j + h.c.), \tag{2.20}$$

where $i$ and $j$ label the sites of the QD, $\hat{c}_i^\dagger$ and $\hat{c}_i$ are creation and annihilation operators for an electron at site $i$, and $t = -2.8$ eV is the hopping integral. We also assume that the on-site energies are zero. Numerical diagonalization of the tight binding Hamiltonian for the GQD consisting of $N$ atoms gives $N$ levels with the wave functions $\psi_n$ and the corresponding energies $E_n$. The wave functions and the energy spectra are obtained numerically.

The Hamiltonian $H'(t)$ describes the interaction of the electron system with the optical field as follows

$$H'(t) = -e \sum_i \hat{c}_i^\dagger \hat{c}_i \mathbf{r}_i \cdot \mathbf{F}(t), \tag{2.21}$$

where $\mathbf{r}_i$ is the position of the $i$th atom and $\mathbf{F}(t)$ is the time-dependent electric field of the optical pulse. Below we consider an elliptically polarized pulse, for which the time-dependent electric field is defined as

$$\mathbf{F}(t) = F_x(t)\hat{\mathbf{e}}_x + F_y(t)\hat{\mathbf{e}}_y, \tag{2.22}$$

where

$$\begin{aligned} F_x(t) &= F_{0,x} e^{-(t/\tau_0)^2} \cos(\omega_0 t), \\ F_y(t) &= F_{0,y} e^{-(t/\tau_0)^2} \sin(\omega_0 t) \end{aligned} \tag{2.23}$$

and

$$F_{0,x} = \frac{F_0}{\sqrt{1+\epsilon^2}}, \\ F_{0,y} = \frac{\epsilon F_0}{\sqrt{1+\epsilon^2}}. \tag{2.24}$$

Here $F_0$, $\epsilon$, $\omega_0$, and $\tau_0$, are the amplitude, ellipticity, frequency, and duration of an elliptically polarized optical pulse. The pulse is linearly (circularly) polarized for $\epsilon$=0 ($\epsilon$=1). Thus, the driver ellipticity $\epsilon$ corresponding to the incident laser pulse is defined as

$$\epsilon = \frac{F_{0,y}}{F_{0,x}}. \tag{2.25}$$

### *2.1.3 Formulation of Density Matrix equations*

We study the electron dynamics of the electron system of GQD using the time evolution of the density operator $\hat{\rho}$, which is determined by the following density matrix equation

$$\frac{d\hat{\rho}}{dt} = \frac{i}{\hbar}\left[\hat{\rho}, H\right] = \frac{i}{\hbar}\left[\hat{\rho}, H_0\right] + \frac{i}{\hbar}\left[\hat{\rho}, H'\right], \tag{2.26}$$

where $[\hat{A}, \hat{B}]$ is the commutator of operators $\hat{A}$ and $\hat{B}$.

Taking the matrix elements of the left- and right-hand sides of Eq. (2.26) between the states $\psi_n$ of field-free Hamiltonian $H_0$, we obtain the following matrix equation

$$\dot{\rho}_{mn} = i\omega_{mn}\rho_{mn} + \frac{i}{\hbar}\sum_k (\rho_{mk}H'_{kn} - H'_{mk}\rho_{kn}), \tag{2.27}$$

where $\omega_{mn} = \frac{(E_n - E_m)}{\hbar}$, $E_n$ is the energy corresponding to the state $\psi_n$, $\rho_{mn} =< \psi_m|\hat{\rho}|\psi_n >$, $H'_{kn} = -D_{kn}F(t)$, and $D_{kn} = e < \psi_k|\hat{r}|\psi_n >$ is the dipole matrix element of the dipole operator $e\hat{r}$.

Employing the density matrix approach provides an opportunity to incorporate the relax-

ation process into our model through the corresponding phenomenological relaxation rates. To address the relaxation process corresponding to dipole decay we introduce the dephasing time, $\tau$, which we assume is the same for all nondiagonal matrix elements of the density matrix. Below we set the dephasing time at $\tau$=10 fs. With the relaxation processes, the density matrix equation (2.27) takes the following form

$$\begin{aligned} \dot{\rho}_{mn} &= i\omega_{mn}\rho_{mn} + \frac{i}{\hbar}\sum_k (\rho_{mk}H'_{kn} - H'_{mk}\rho_{kn}) \\ &\quad -(1-\delta_{nm})\rho_{mn}/\tau, \end{aligned} \tag{2.28}$$

where $\delta_{nm}$ is the Kronecker delta symbol.

With the density matrix expressed in the interaction representation,

$$\tilde{\rho}_{mn} = \rho_{mn}e^{-i\omega_{mn}t}, \tag{2.29}$$

the system of equations (2.28) takes the following form

$$\begin{aligned} \dot{\tilde{\rho}}_{mn} &= \frac{i}{\hbar}\sum_k \left[\tilde{\rho}_{mk}e^{i\omega_{nk}t}H'_{kn} - H'_{mk}\tilde{\rho}_{kn}e^{i\omega_{km}t}\right] \\ &\quad -(1-\delta_{nm})\tilde{\rho}_{mn}/\tau. \end{aligned} \tag{2.30}$$

We solve the system of differential equations (2.30) numerically using the ODEINT library, which is a collection of different numerical algorithms to solve initial value problems of ordinary differential equations [23]. The initial conditions are that, before the pulse, all the valence band (VB) states are occupied and all the conduction band (CB) states are empty,

i.e., $\tilde{\rho}_{nn} = 1$ if $n \in$ VB and $\tilde{\rho}_{nn} = 0$ if $n \in$ CB.

### *2.1.4 Dipole Moment*

With the known solution of the density matrix equation (2.30), the time-dependent dipole moment can be calculated from the following expression

$$d(t) = \sum_{mn} \tilde{\rho}_{mn}(t) e^{i\omega_{mn}t} D_{nm}. \tag{2.31}$$

### *2.1.5 Intensity of High Harmonics*

The time variation of the dipole moment determines the radiation of the system. At a given frequency $\omega$, the intensity of the corresponding radiation is obtained from the following expression

$$I(\omega) = I_x(\omega) + I_y(\omega), \tag{2.32}$$

where

$$\begin{aligned} I_x(\omega) &= \frac{\mu_0 \omega^2}{12\pi c} [|\mathcal{F}_\omega[\dot{d}_x]|^2, \\ I_y(\omega) &= \frac{\mu_0 \omega^2}{12\pi c} |\mathcal{F}_\omega[\dot{d}_y]|^2]. \end{aligned} \tag{2.33}$$

Here $\mathcal{F}_\omega[\dot{d}_x]|^2$ and $\mathcal{F}_\omega[\dot{d}_y]|^2]$ are frequency Fourier transforms of the time derivatives of the corresponding components of the dipole moment.

The order of the generated high harmonic is defined in units of $\omega_0$, i.e.,

$$N_\omega = \frac{\omega}{\omega_0}. \tag{2.34}$$

### *2.1.6 Harmonic Ellipticity*

The generated high harmonics in the field of an elliptically polarized pulse are also elliptically polarized. We define the corresponding ellipticity $\epsilon(N_\omega)$ of the $N_\omega^{th}$ harmonics by the following expression

$$\epsilon(N_\omega) = \frac{\widetilde{F}_y(N_\omega)}{\widetilde{F}_x(N_\omega)} = \sqrt{\frac{I_y(\omega)}{I_x(\omega)}}. \tag{2.35}$$

where, $\widetilde{F}_x(N_\omega)$ and $\widetilde{F}_y(N_\omega)$ are the $x$ and $y$ components of the electric field of generated $N_\omega^{th}$ harmonics.

## 2.2 Numerical Solution

The theoretical study of the electron dynamics in the two-dimensional QD system involves several steps, including designing the Hamiltonian of the system, obtaining the eigenvalues and eigenfunctions by diagonalization of the time-independent Hamiltonian that describes the neutral QD system, using total Hamiltonian incorporating perturbation Hamiltonian to solve the ordinary differential equations (ODEs). Solving the large set of coupled nonlinear ODEs requires significant effort in terms of time and accuracy.

The ODE describes a wide variety of physical phenomena. However, the ODE can be solved analytically in only a few systems. Indeed, an analytic solution of an ODE is available in minimal cases, indicating that numerical methods have to be employed in most cases. Obtaining numerical solutions for ODEs is a long-established trend and has gained significant popularity with the rise of computers.

In mathematical terms, we express the ordinary differential equation (ODE) in the fol-

lowing form,

$$\frac{dy}{dt} = f(y(t), t), \qquad y(t_0) = y_0. \tag{2.36}$$

Here, the time t is used as the independent variable. An initial value problem (IVP) of an ODE is to find a solution given an initial value $x_0(t_0)$.The beginning point is to start with $x_0(t_0)$ and iteratively create a sequence $x(t_i)$ where every $x(t_i)$ is obtained from previously calculated values of $x$.

### *2.2.1 Solution of Coupled Nonlinear Differential Equations*

Runge-Kutta solvers are the most famous for ODEs in equation (2.36). These solvers are easy to implement and can easily be applied to various problems. They come with step-size control, and some algorithms possess dense output functionality. Another class of solvers is implicit solvers, which are essential for stiff problems; hence, ODEs have two or more scales of the independent variables. In this current work, we use the Scipy odeint library to solve the coupled nonlinear ODEs of the GQD system.

Odeint is a modern library for numerically solving ODEs. The Odeint is available in several programming languages, including C++, Fortran, Python, and Matlab. This results in the library's incredible applicability, especially in non-standard environments supporting matrix types and arbitrary precision arithmetics, and can even be efficiently run on CUDA GPUs.

### *2.2.2 Fourier Transform*

Fourier transform is an integral component across several disciplines, including signal processing, differential analysis, and quantum mechanics, where the Fourier transform is used to relate the position and momentum space,

$$\psi(x,t) = \frac{1}{\sqrt{2\pi}} \int_{-\infty}^{\infty} \phi(k,t) e^{ikx} dk, \tag{2.37}$$

$$\phi(k,t) = \frac{1}{\sqrt{2\pi}} \int_{-\infty}^{\infty} \psi(x,t) e^{-ikx} dx. \tag{2.38}$$

We don't need the continuous Fourier transform when a signal is discrete and periodic. Instead, we use the discrete Fourier transform or DFT.

#### *2.2.2.1 Discrete Fourier Transform*

Discrete Fourier Transform (DFT) is a significant discrete transform that can transform sharply between two discrete and periodic data sets. DFT is used when we have a discrete, periodic function $f_n$, resulting in a discrete, periodic transform $F_m$. The DFT and inverse DFT are given by

$$F_m = \sum_{n=0}^{N-1} f_n e^{-2\pi imn/N} \quad \Leftrightarrow \quad f_n = \frac{1}{N} \sum_{m=0}^{N-1} F_m e^{2\pi imn/N}. \tag{2.39}$$

Here, DFT contains two finite summations; it accepts an input function with N discrete points and provides the output containing N discrete points.

#### *2.2.2.2 Fast Fourier Transform*

While solving problems in quantum physics, we prefer the efficient numerical techniques. To solve the $N$-point DFT, acting on input $f_n$ of size $N$ in equation (2.39) we perform $N$ multiplication of $f_n$ with $e^{2\pi imn/N}$. Furthermore, we repeat another $N$ time for each value of $m$, so in total performing $N^2$ multiplications which result in the DFT scales like $\sim N^2$ with the input of size $N$. This calculation involves a large number of repeated calculations, increasing complexity. The Fast Fourier Transform (FFT) is the significantly more efficient algorithm obtained by updating the DFT to remove redundant calculations by taking advantage of such recurring symmetries in DFT. The most common implementation of the FFT is the Cooley-Tuckey algorithm [24].

Our work (See Eq. (2.33)) uses the FFT using the SciPy module in Python programming language [25]. The SciPy uses the algorithms provided by FFTPACK to calculate highly efficient FFTs.

# CHAPTER 3

# CHAPTER 3 GENERATION OF HIGH HARMONICS AND ITS DEPENDENCE ON THE RELAXATION PROCESS

This chapter focuses on understanding the ultrafast electron dynamics of GQD, the HHG mechanism in GQD, the effect of relaxation on HHG, and mainly, how sensitive the emission spectra introduce finite dephasing. The significant findings presented in this chapter are published in a Physical Review B journal titled Ultrafast electron dynamics of graphene quantum dots in graphene quantum dots: High harmonic generation [26].

## 3.1 Introduction

Strong optical pulses, the amplitudes of which are comparable to internal electric fields in solids, are intensively used to probe and control both the transport and optical properties of electron systems[27; 28; 29; 30; 31; 32; 33; 34; 35; 36; 37; 38; 39; 40]. The electron dynamics in such pulses is highly nonlinear, which results in such nonlinear optical effects as nonlinear absorption and high harmonic generation[41]. The High Harmonic Generation (HHG) has a special role since it allows to convert a low frequency pulse in the visible or infrared range into the high frequency radiation, for example, extreme ultraviolet or soft X-ray[42; 43; 44; 18; 45; 46; 47; 48; 49]. The mechanism, which is responsible for generation of high frequency harmonics, is different for a system of randomly positioned atoms and a system of a crystalline solid. High harmonic generation in atomic or molecular gases occurs through a three step process, which consists of a tunnel ionization of an electron, its acceleration in the laser field, and a subsequent recollision with an atom[50]. Such process

results in unique linear dependence of the HHG cutoff on the energy of the pulse[42].

In solids, the HHG occurs through the combination of two types of dynamics induced by the field of the pulse: interband and intraband dynamics[18; 45; 46; 51; 52; 53]. Due to the interband dynamics, the electrons are redistributed between the bands of a solid, while, due to the intraband dynamics, the electrons are transferred through the non-parabolic bands, which results in nonlinear optical response. Both of these dynamics contribute to the generation of high harmonics. Which dynamics provides the main contribution depends on the band gap of a solid and the parameters of the pulse, e.g., its frequency. The unique property of HHG in solids is that the HHG energy cutoff has linear dependence on the pulse amplitude[18], while in gases, the HHG cutoff has linear dependence on the pulse intensity [42].

HHG is one of the characteristics of the nonlinear optical response of solids. Their nonlinear optical properties strongly depend on the band structure, impurity level, and other internal characteristics of solids. For example, tin sulphide (SnS) has shown excellent nonlinear optical properties due to tunable bandgap and fast carrier mobility[54], a system consisting of a few layer of bismuthene has shown strong nonlinear refraction effect and all optical switching[55], graphdiyne has demonstrated relatively large nonlinear refractive index[56]. A new family of two dimensional (2D) materials, 2D transition metal carbides or nitrides (MXenes), has shown promising nonlinear optical properties, which can be tuned by varying the ratios of M or X elements and their surface terminations[57].

Nonlinear optical properties of solids can also be tuned by changing their dimensionality,

making them two dimensional, one dimensional, or zero dimensional systems. Zero dimensional systems, which are called quantum dots (QDs) or artificial atoms[58; 59], consist of a finite number of atoms of the corresponding solid. The QDs have many applications in different fields of science[60; 61; 62; 63; 64]. Due to dimensional quantization, the energy spectra of QDs are discrete, which is similar to spectra of regular atoms. At the same time, the QDs still have the features of the crystal structure of the corresponding solid. Namely, within the region of a QD, the atoms are placed periodically and the discrete energy levels of the QD can be usually identified as belonging to different bands of the solid. Thus, the HHG spectra of QDs can resemble the ones of the corresponding solids. In Ref. [65], a transformation of the HHG spectrum from the atomic one to the spectrum of the crystalline solid is traced within the one dimensional model. It was shown that such a transformation occurs for the QD consisting of just six nuclei.

In the present work, we consider HHG in QDs, which are based on graphene[66; 67; 68; 69]. Graphene is a monolayer of carbon atoms with honeycomb crystal strucure[70; 71]. It has unique transport and optical properties, which are related to its specific relativistic low-energy dispersion of the Dirac type[72; 73; 74; 75]. In the strong field of an ultrashort optical pulse, such dispersion results in interference patterns in the conduction band population distribution in the reciprocal space[76]. In graphene with broken inversion symmetry, ultrashort circularly polarized optical pulse results in ultrafast valley polarization[77], which occurs due to the valley-dependent topological resonance[37; 77]. Graphene QDs, interacting with a short optical pulse, have also shown nonlinear absorption properties[78]. The

nonlinear absorption of other monolayer QD systems, transition-metal dichalcogenide QDs, has also been reported in Ref. [79]. Such nonlinear optical response has been studied for ultrashort pulses, the duration of which is much less than the characteristic dephasing or relaxation time. In this case, the electron dynamics during the pulse is coherent. In the present paper, we address the problem of a finite relaxation rate and study how the relaxation processes can modify graphene QD's nonlinear optical response, such as HHG. It has been previously shown that the HHG is sensitive to the relaxation rate in three-dimensional solids[53].

The relaxation processes result in non-coherent electron dynamics in the field of the pulse. Such dynamics is described within the density matrix approach[21; 20], which is used below in the present paper. We also consider only the internal electron dynamics within the QD region without taking into account the possibility of ionization of the QD.

### 3.2 Results and Discussion

We consider a graphene QD, which consists of $N = 24$ carbon atoms, see Fig. 3.1. The distance between the nearest neighbor atoms is $a = 1.42$Å. The electron system of such a QD is described within the tight-binding model with the Hamiltonian defined in eq.(2.20).

We consider a graphene QD, the structure of which is shown in Fig. 3.1. It consists of 24 carbon atoms and has $D_{6h}$ symmetry. The energy spectrum of such a QD is obtained within the tight-binding model and consists of singly, doubly, and triply degenerate levels. The corresponding energy spectrum is shown in Fig. 3.2. Twelve levels with the negative

energies are initially occupied and belong to the VB. The levels with the positive energies belong to the CB. The band gap for the QD is 3 eV. The maximum energy difference between the CB and the VB levels is around 16 eV. In this case, if the high harmonics are generated through transitions between QD levels then 16 eV should be the maximum frequency that can be generated in such a QD. The time variations of populations of QD levels, i.e., "dressing" of the QD states due to electron-pulse interactions, result in harmonics with the frequencies larger than 16 eV, as discussed below.

We consider graphene QD of a small size only, i.e., QD with 24 atoms. Such QD has

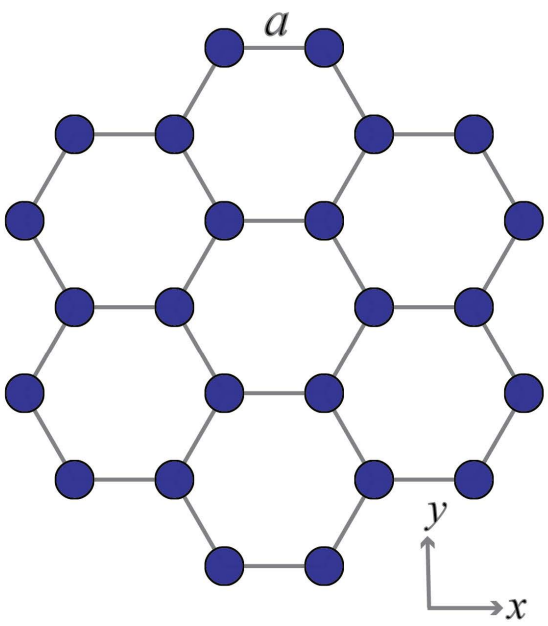


Figure 3.1 Graphene quantum dot consisting of 24 carbon atoms. The incident laser pulse is linearly polarized along the $x$-direction. The distance between the nearest neighbor atoms is $a = 1.42$Å.

relatively large band gap, 3 eV, so for the optical pulse with the frequency of 1-2 eV there is no resonant transitions within the system. With increasing the QD size, the band gap due to dimensional quantization decreases, resulting in resonant transitions at relatively small frequencies of the pulse. At the same time, the main effects of the relaxation processes on the HHG in graphene QDs are already captured by the QDs of a small size.

We apply a linearly polarized pulse, the profile of which is shown in Fig. 3.3(a) for the

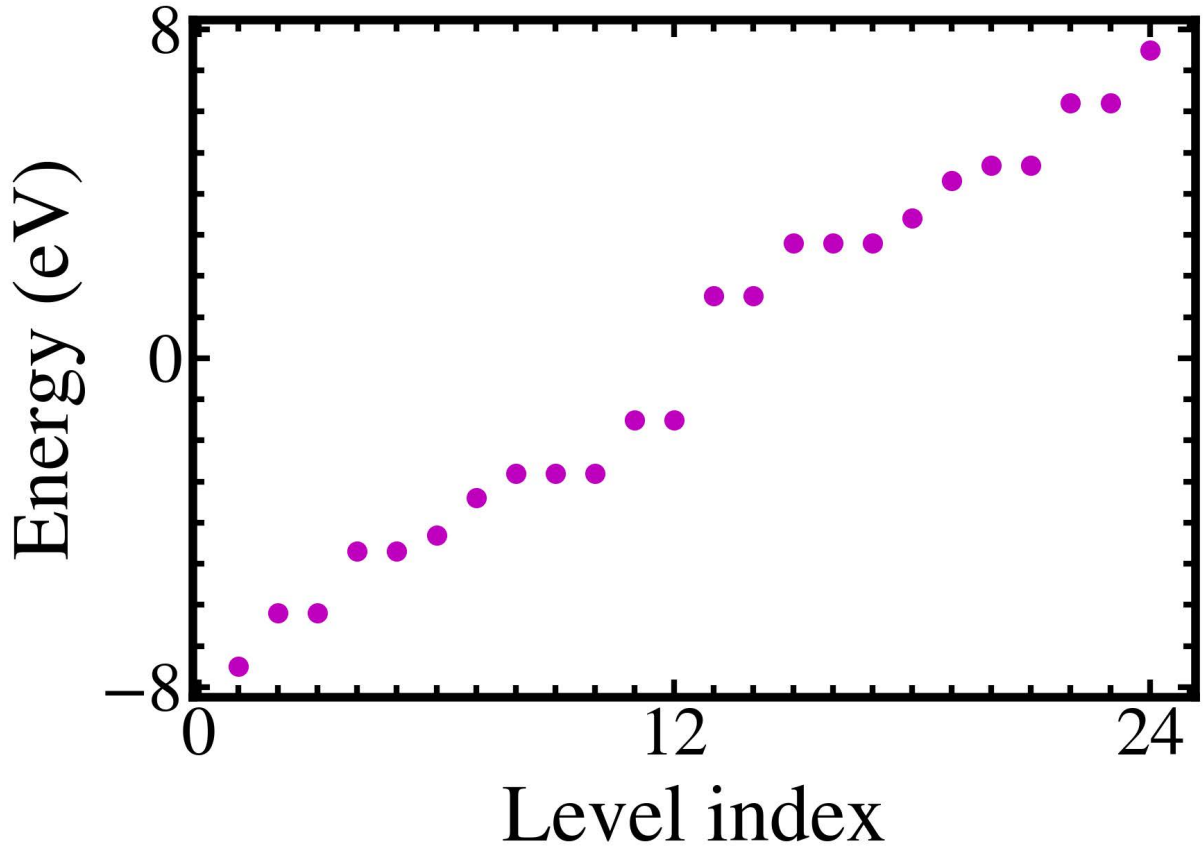


Figure 3.2 Energy spectrum of graphene QD shown in Fig. 3.1. The spectrum consists of singly, doubly, and triply degenerate levels. Levels with the negative energy correspond to the valence band while the levels with the positive energy correspond to the conduction band. Before the pulse, all valence band levels are occupied.

field amplitude of $F_0 = 0.5$ V/Åand the pulse frequency of $\hbar\omega_0 = 1$ eV. From the solution of the density matrix equation, we obtain the CB population $N_{CB}$,

$$N_{CB}(t) = \sum_{m \in \mathrm{CB}} \tilde{\rho}_{mm}(t), \tag{3.1}$$

and the time-dependent dipole moment of the electron system. Their typical time depen-

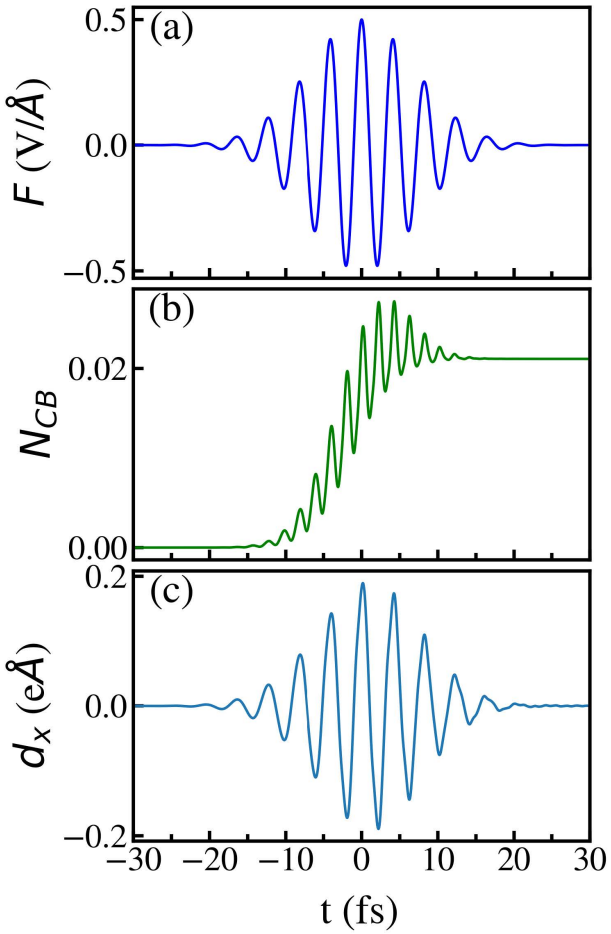


Figure 3.3 Panel (a): profile of a linearly polarized pulse. The pulse amplitude is 0.5 V/Å, and the frequency of the pulse is $\hbar\omega_0 = 1$ eV. Panel (b): conduction band population $N_{CB}$ as a function of time. The QD is in the field of the pulse shown in panel (a). The conduction band population is normalized by the number of electrons, i.e., it is divided by 12. The corresponding dipole moment is shown in panel (c). Only $x$ component of the dipole moment is nonzero. The dipole moment roughly follows the profile of the electric field shown in panel (a).

dences are shown in Fig. 3.3(b) and (c). In Eq. (4.1), the sum is over all QD CB states. The CB population [see Eq. (4.1)] illustrates highly irreversible electron dynamics when the residual CB population, i.e., the population after the pulse, is comparable to the maximum CB population during the pulse. The positions of the maxima of $N_{\rm CB}$ are correlated with the maxima of $|F(t)|$.

The typical profile of the dipole moment of QD is shown in Fig. 3.3(c). It is roughly proportional to the electric field of the pulse, but with some nonlinear features, which finally determine the nonlinear optical response of the system and generation of high harmonics in the radiation spectrum.

The electron dynamics in the field of the optical pulse strongly depends on the relaxation processes. To illustrate such dependence we show in Fig. 3.4 the CB population for different relaxation times, $\tau$. The field amplitude is 0.5 V/Å. Here, we consider two frequencies of the pulse, which are both below the band gap of graphene QG: $\hbar\omega_0 = 1$ eV, which is almost three times less than the QD band gap, and $\hbar\omega_0 = 2$ eV. One of the characteristics of the electron dynamics is its reversibility, i.e., returning of the system to its initial state after the pulse. We introduce quantitative characteristics of the reversibility, $\eta$, as the ratio of the CB population after the pulse and the maximum CB population during the pulse,

$$\eta = \frac{N_{CB}^{\rm residual}}{N_{CB}^{\rm max}}. \tag{3.2}$$

The ratio $\eta$ is between zero and one, where $\eta = 0$ corresponds to a perfectly reversible dynamics, while $\eta = 1$ corresponds to a highly irreversible dynamics.

For small frequency of the pulse, see Fig. 3.4(a), with increasing the relaxation time, the

electron dynamics becomes more reversible. Here, the reversibility parameter $\eta$ decreases from 0.98 for $\tau = 4$ fs to 0.6 for $\tau = 20$ fs. Thus, for $\tau = 4$ fs, the electron dynamics is highly irreversible, while, for $\tau = 20$ fs, the electron dynamics is partially reversible. Such partial reversibility of the electron dynamics is related to its coherence, which is more preserved for larger values of $\tau$.

Different situation occurs at larger frequency of the pulse, see Fig. 3.4(b), where the frequency of the pulse is $\hbar\omega = 2$ eV. In this case, the electron dynamics is much less sensitive to the relaxation time and the dynamics is highly irreversible for all values of $\tau$, see Fig. 3.4(b). Here, for all cases, the parameter $\eta$ is close to 0.99. At the same time, the whole CB population is much larger than the CB population for the low frequency case, see Fig. 3.4(a). For example, for $\hbar\omega_0 = 1$ eV and $\tau = 4$ fs the residual CB population is around 0.04,

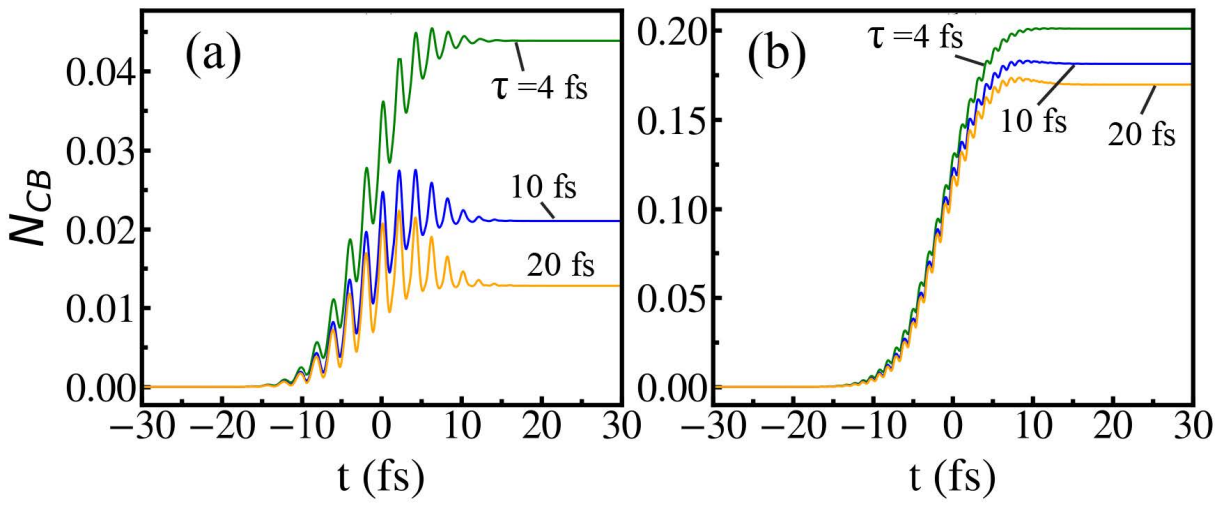


Figure 3.4 Conduction band population as a function of time. The conduction band population is normalized by the number of electrons, i.e., it is divided by 12. The corresponding relaxation times are shown next to the lines. The frequency of the pulse is $\hbar\omega_0 = 1$ eV (a) and $\hbar\omega_0 = 2$ eV (b). The pulse amplitude is 0.5 V/Å.

see Fig. 3.4(a), while for $\hbar\omega_0 = 2$ eV and $\tau = 4$ fs it is around 0.2, see Fig. 3.4(b).

The total CB population shown in Fig. 3.4 describes the net effect of the pulse on the QD. To clarify how different levels of the QD respond to the optical field we show in Fig. 3.5 the residual populations of different CB levels. As expected, the levels with the lower energies are generally more populated compared to the higher energy levels, but this dependence is not monotonic and some higher energy levels are more populated than the lower energy levels. This is due to properties of the dipole matrix elements, which do not show monotonic dependence on the energy of the levels.

The dependences of the populations of individual levels on the relaxation time are sensitive to the frequency of the pulse. For the pulse frequency of 1 eV, see Fig. 3.5(a), with increasing the relaxation time, the populations of CB levels are suppressed. Such suppression is more pronounced for the higher energy levels. For example, when the relaxation time increases from 4 fs to 20 fs, the population of the lowest CB level decreases by a factor of $\approx 2.5$, while the population of the highest energy level decreases by almost 11 times. When the frequency of the pulse becomes close to the band gap, see Fig. 3.5(b), the populations of the energy levels have weak dependence on the relaxation time. When the relaxation time increases from 4 fs to 20 fs, the populations of the levels change by less than $\approx 20$ %. Also, for all CB levels except one, with increasing the relaxation time, the populations decrease, but for the second CB level we observe a different behavior. For this level, when the frequency of the pulse is 2 eV, with increasing $\tau$, its population slightly increases. This is related to triple degeneracy of the second CB level, see Fig. 3.2, which results in large

density of states associated with this level.

The radiated power $P(\omega)$ of corresponding emission spectra of the QD is calculated from Eq. (3.3)

$$P(\omega) = \frac{\mu_0 \omega^2}{12\pi c} |\mathcal{F}_\omega[\dot{d}_x]|^2, \tag{3.3}$$

and normalized power, $P_N(\omega)$, of the spectra is obtained from Eq (3.4)

$$P_N(\omega) = \frac{P(\omega)}{P(\omega_0)}. \tag{3.4}$$

Since polarization of the pulse is along the axis of symmetry of graphene QD, i.e., along the $x$-axis, there is no induced dipole moment along the $y$ direction and the dipole radiation

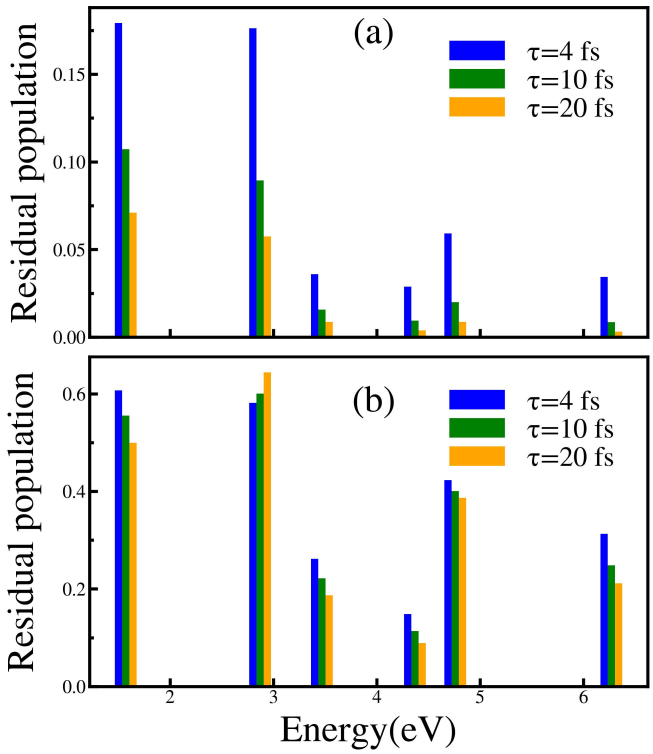


Figure 3.5 Residual population of conduction band levels. The pulse amplitude is 0.5 V/Å. The corresponding dephasing times are marked in each panel. The frequency of the pulse is $\hbar\omega_0 = 1$ eV (a) and $\hbar\omega_0 = 2$ eV (b).

from the system is linearly polarized along the $x$ direction. In Fig. 3.6, we show the radiation spectra for three different frequencies of the pulse and different values of the relaxation time. Here, we added the results for the frequency of $\hbar\omega_0 = 3.1$ eV, which is a little large than the band gap. We did not study the electron dynamics at this frequency in great details, since,

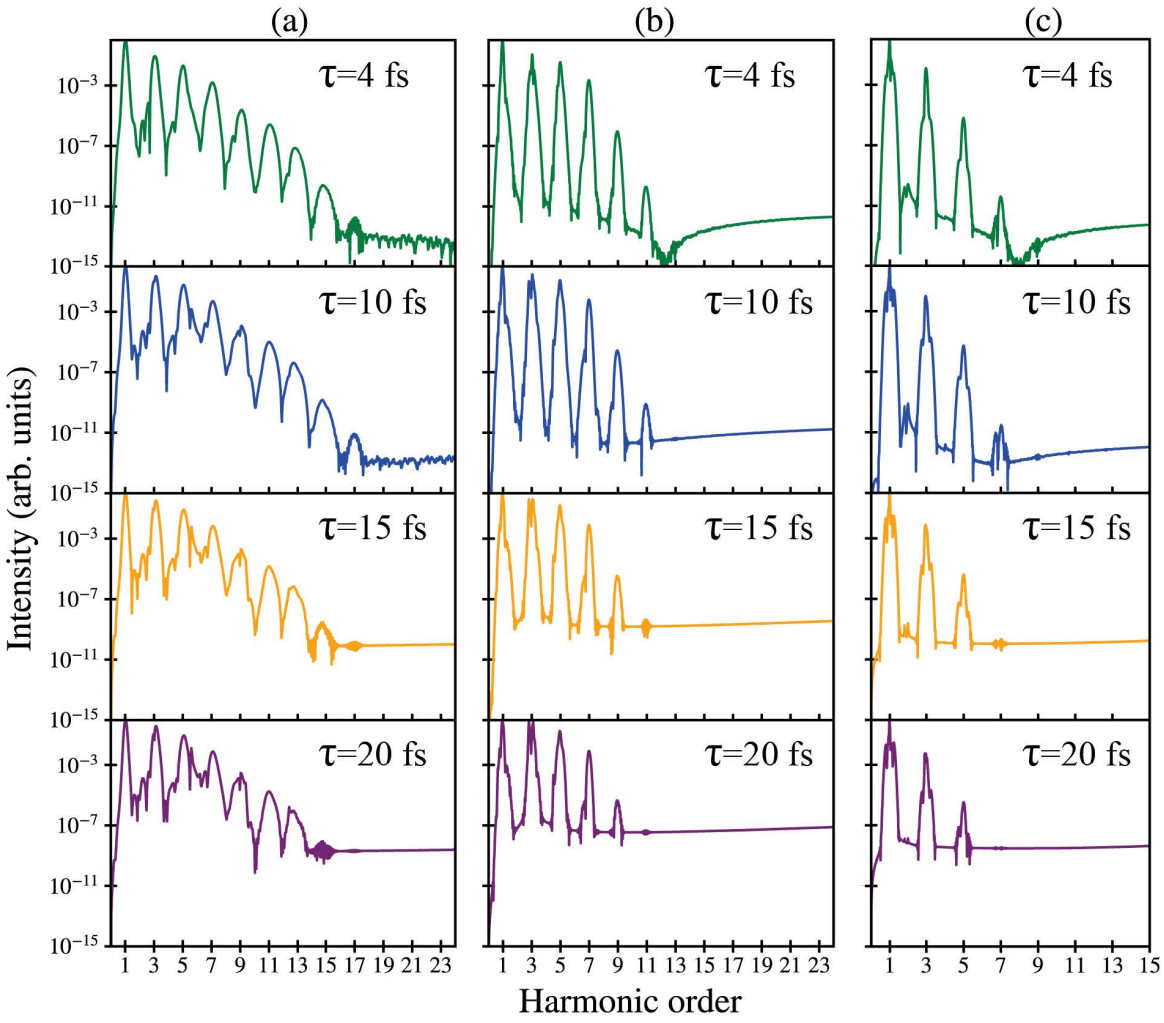


Figure 3.6 Emission spectrum of graphene QD. High harmonics with well-defined cutoffs are clearly visible in the spectrum. The corresponding relaxation times are marked for each graph. The frequency of the pulse is $\hbar\omega_0 = 1$ eV in column (a), $\hbar\omega_0 = 2$ eV in column (b), and $\hbar\omega_0 = 3.1$ eV in column (c). With increasing the relaxation time, the emission spectrum becomes more noisy with less defined high harmonic peaks. The pulse amplitude is $F_0 = 0.4$ V/Å.

as we can see from Fig. 3.6, there are only a few high harmonics that are generated in this case, see column (c) in Fig. 3.6. For example, at the relaxation time of 20 fs, the maximum harmonic that is generated at $\hbar\omega_0 = 3.1$ eV is 5, while at the frequency of 1 eV, it is 13.

Since the QD has an inversion symmetry, only odd harmonics are generated[80]. The radiation spectra have clear cutoff frequencies, which depend both on the relaxation time and the frequency of the pulse. Namely, with increasing the frequency of the pulse, the maximum harmonic order that is generated decreases and, with increasing the relaxation time, the cutoff frequency also decreases. Thus, when the electron dynamics becomes incoherent, i.e., at small relaxation times, the system generates more high harmonics, see Fig. 3.6, compared to the coherent case, $\tau = 20$ fs. Such behavior is correlated with the population of the CB levels shown in Fig. 3.5, where with increasing $\tau$, the higher energy levels become less populated, which results in suppression of the high harmonics.

Comparing the results for different frequencies of the pulse, see columns (a)-(c) in Fig. 3.6, we can say that, with increasing the frequency of the pulse, the energy cutoff increases. For example, for the relaxation time of $\tau = 4$ fs, the highest harmonic that is generated by the pulse with the frequency of 1 eV [see column(a)] is 15 with the corresponding energy of 15 eV. For the same relaxation time, the highest harmonic for the pulse with the frequency of 2 eV [see column (b)] is 11, the energy of which is 22 eV. At the same time, when the frequency of the pulse reaches the band gap, see column (c) in Fig. 3.6, the maximum harmonics is 7 with the corresponding energy of 21.7 eV, which suggests that the energy cutoff reaches a saturated value when the frequency of the pulse approaches the band gap.

Similarly, looking at the results for the relaxation time of 20 fs, see Fig. 3.6, we can find that the maximum energies of the high harmonics are 13 eV, 18 eV, and 15.5 eV, for the pulse frequencies of 1 eV, 2 eV, and 3.1 eV, respectively. In this case, there is even a small suppression of the energy cutoff when the frequency of the pulse becomes close to the band gap.

Thus, the laser pulse with the higher frequency, but below the band gap, strongly perturbs the system, resulting in generation of higher frequency harmonics and higher energy cutoff comparing to the case of the low frequency pulse. Such behavior is correlated with the results shown in Fig. 3.5, where the populations of the CB levels with high energies are larger for the higher frequency pulse.

Another property of the emission spectra shown in Fig. 3.6 is that, with decreasing the relaxation time, the emission spectra become less noisy and with well defined harmonic peaks. For example, for the relaxation time of $\tau = 20$ fs, the emission spectrum between the fifth and the seventh harmonics has extra noisy features which disappear at the relaxation time of $\tau = 4$ fs. The reason for such behavior is that, for a shorter relaxation time, fewer trajectories contribute to a given harmonic [81; 82], while for a longer relaxation time, multiple trajectories, which occur during the coherent electron dynamics, result in extra interference effects and complex emission spectra[83].

The dependencies of the intensities of high harmonics on the pulse amplitude are shown in Fig. 3.7 for different relaxation times and different frequencies of the pulse. Only the first four lowest harmonics are shown. When the frequency of the pulse is 1 eV, see Fig. 3.7(a)-

(d), the intensities of the high harmonics monotonically increase with $F_0$. With increasing the harmonic order, the dependence of its intensity on $F_0$ becomes stronger. For example, for $N_\omega = 3$, the intensity has a weak dependence on $F_0$ and is almost constant at $10^{-3}$, while for $N_\omega = 9$, the intensity changes from $10^{-8}$ at small $F_0$ to $10^{-3}$ at large $F_0$. Such behavior is similar for all relaxation times.

When the frequency of the pulse becomes close to the band gap, see Fig. 3.7(e)-(h), where the frequency of the pulse is 2 eV, the intensities of high harmonics become non-monotonic functions of the field amplitude for low harmonics. Namely, the intensities of the third and the fifth harmonics have maxima at the field amplitude close to 0.4 V/Å. At the same time, the intensities of the higher harmonics, $N_\omega = 7$ and 9, have monotonic dependence on $F_0$.

Another difference between the low and the high frequencies of the pulse is that the ninth harmonic ($N_\omega = 9$) has much smaller intensity for the case of $\hbar\omega_0 = 2$ eV compared to the

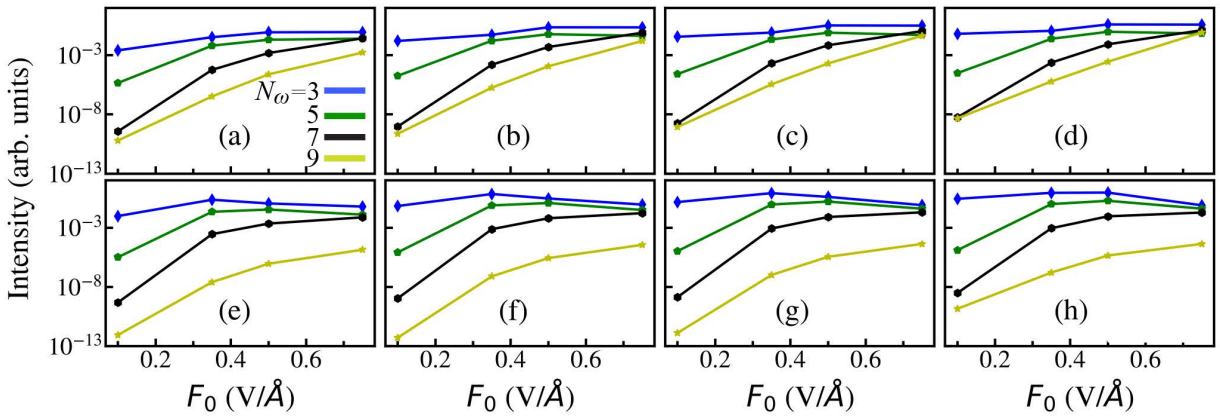


Figure 3.7 Intensity of the first four high harmonics ($N_\omega$ = 3, 5, 7, and 9) versus the amplitude of the optical pulse, $F_0$. The frequency of the pulse is $\hbar\omega_0$ = 1 eV in panels (a)-(d) and 2 eV in panels (e)-(h). The relaxation time is 4 fs (a) & ( e), 10 fs (b) & (f), 15 fs (c) & (g), and 20 fs (d) & (h).

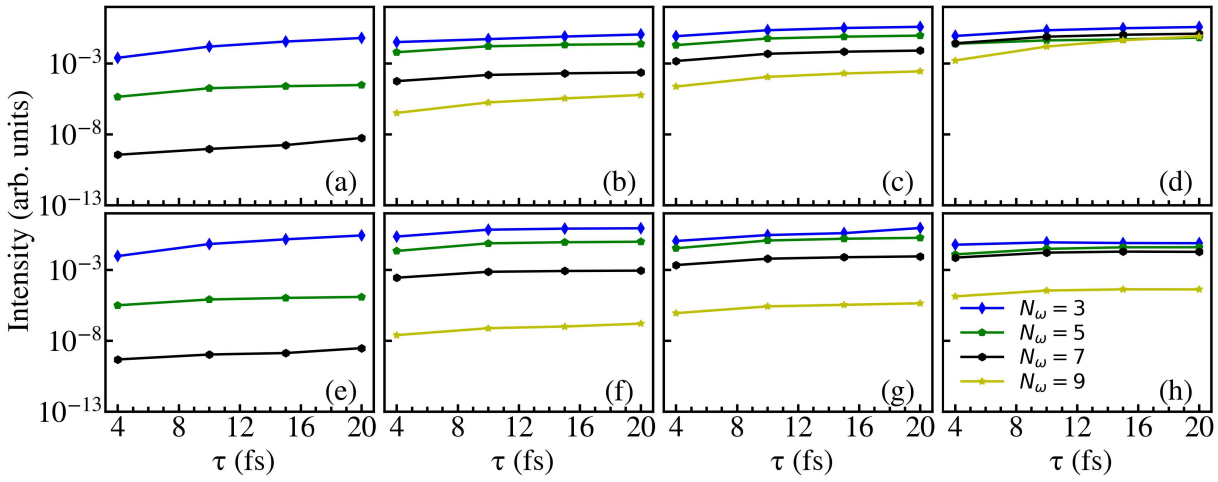


Figure 3.8 Intensity of the first four high harmonics ($N_\omega$ = 3, 5, 7, and 9) versus the relaxation time. The frequency of the pulse is $\hbar\omega_0$ = 1 eV in panels (a)-(d) and 2 eV in panels (e)-(h). The pulse amplitude is 0.1 V/Å(a) & ( e), 0.35 V/Å(b) & (f), 0.5 V/Å(c) & (g), and 0.75 V/Å(d) & (h).

one of $\hbar\omega_0 = 1$ eV. This is related to the fact that, for the pulse frequency of 2 eV, the ninth harmonics has the energy of 18 eV, which is larger than the maximum range of singe particle energies within the QD, see Fig. 3.2, where this range is around 16 eV. As a result the ninth harmonic is generated due to collective transitions between many levels, which results to its low intensity for the pulse with 2 eV frequency.

To clarify the effect of relaxation time on the radiation spectra, we show in Fig. 3.8 the intensities of the first four harmonics as functions of the relaxation time. In panels (a) and (e), which correspond to the low field amplitude of 0.1 V/Å, only first three harmonics are shown since the fourth harmonics ($N_\omega = 9$) is not generated in this case. For all cases, shown in Fig. 3.8, the intensities monotonically increase with the relaxation time. Thus, the largest intensities of the high harmonics are realized for the coherent electron dynamics,

i.e., for the large relaxation time. The radiation spectra also show a stronger sensitivity to the relaxation processes at small field amplitude. Namely, at $F_0 = 0.1$ V/Å, the intensities of the high harmonics change by almost two orders of magnitude when $\tau$ increases from 4 fs to 20 fs, see Fig. 3.8(a) and (e), while at $F_0 = 0.75$ V/Å, the corresponding variations of the intensities are ten times smaller, see Fig. 3.8(d) and (h).

The intensities of the high harmonics in Figs. 3.6-3.8 are shown in units of the intensity of the main peak at the frequency $\omega_0$. The intensity of the main peak can be estimated from the calculated dipole moment and its Fourier transform. For example, for the field amplitude of 0.5 V/Å, the frequency of the pulse $\hbar\omega_0 = 1$ eV, and relaxation time of 4 fs, the power radiated by the QD at frequency $\omega_0$ is around 10 W/cm$^2$. Then, as follows from Figs. 3.6-3.8, the power radiated by the QD at the frequencies of high harmonics is a few orders of magnitude smaller.

One of the important characteristics of the radiation spectrum is its high harmonic cutoff, which is defined as the maximum harmonic order that can be generated during the pulse. In Fig. 3.9, the high harmonic cutoff is shown as a function of the pulse amplitude, $F_0$, for different frequencies of the pulse and different relaxation times. The curve for the relaxation time of 10 fs coincides with the one for $\tau = 4$ fs. When the relaxation time increases to 20 fs then, as we mentioned above, the corresponding harmonic cutoff decreases. The dependence of the harmonic cutoff on the field amplitude is different for different frequencies of the pulse. For small frequency, $\hbar\omega_0 = 1$ eV, the dependence of the harmonic cutoff on $F_0$ is almost linear, see Fig. 3.9(a). The linear dependence of the HHG cutoff on the field amplitude is

also observed in solids, both two dimensional and three dimensional[18].

Different behavior is observed for larger frequencies of the pulse, $\hbar\omega_0 = 2$ eV and 3.1 eV, see Fig. 3.9(b) and (c). In this case, there is a clear deviation from the linear dependence. Namely, at small field amplitudes, $F_0 < 0.35$ V/Å, there is almost linear dependence of the harmonic cutoff on $F_0$, while at larger field amplitudes, $F_0 > 0.35$ V/Å, the harmonic cutoff becomes suppressed. Here, for the relaxation time of 20 fs, there is a saturation behavior and the harmonic cutoff is constant, while for the smaller relaxation times, 4 fs and 10 fs, the harmonic cutoff is constant within small range of $F_0$, up to 0.5 V/Å, and then it increases with the slope that is less then the one at small field amplitudes, $F_0 < 0.35$ V/Å.

When the frequency of the pulse becomes almost equal to the band gap, $\hbar\omega_0 = 3.1$ eV, the harmonic cutoff as the function of the field amplitude, see Fig. 3.9(c), also shows dependence with the variable slope. Here, the slope is large at small field amplitude, $F_0 < 0.1$ V/Å, then it decreases for $0.1 < F_0 < 0.35$ V/Å, becomes zero within some range of $F_0$, and increases again.

Thus, for the high frequencies of the pulse, $\hbar\omega_0 > 2$ eV, there is a suppression of the harmonic cutoff at large field amplitudes. Such property can be attributed to a finite number of energy levels within graphene QD, which results in finite energy range of around 16 eV, [see Fig. 3.2]. The harmonic cutoff in the HHG spectrum determines also the corresponding energy cutoff, which, for $\hbar\omega_0 = 2$ eV, is around 18 eV for the relaxation time of 20 fs and 26 eV for $\tau = 10$ fs. These values are larger than the QD energy range of 16 eV, which means that, at large field amplitude, the harmonic cutoff is determined by simultaneous transitions

between many single particle levels.

For all frequencies of the laser pulse, the harmonic cutoff is larger for the system with the smaller relaxation time, i.e., for the less coherent system. It is related to the fact that, for the coherent system, the electron dynamics is more reversible, see Fig. 3.4, which results in less population of the high-energy CB levels and correspondingly in smaller harmonic cutoff.

### 3.3 Conclusion

Due to dimensional quantization, a graphene QD has an intrinsic band gap, which depends on the size of the dot. As a result, in the QD of a small size, an ultrafast electron dynamics in the field of a strong optical pulse can be both reversible and irreversible depending on the frequency of the pulse. If the frequency of the pulse is much less than the band gap of the QD then the electron dynamics is almost reversible, i.e., after the pulse, the electron system returns to its initial state. But if the frequency of the pulse is comparable to the

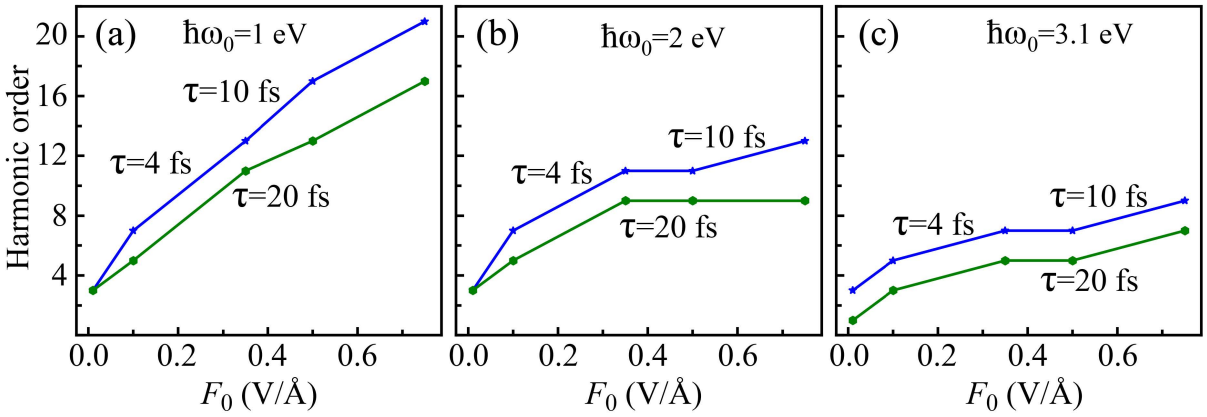


Figure 3.9 Harmonic cutoff versus the amplitude of the optical pulse. The frequency of the pulse is $\hbar\omega_0 = 1$ eV (a), 2 eV (b), and 3.1 eV (c). The relaxation time is shown next to the corresponding line in each panel. The first data point in all panels correspond to the field amplitude of 0.01 V/Å.

band gap then the electron dynamics is highly irreversible, i.e., the residual population of the excited QD states is almost the same as their maximum population during the pulse. The reversibility of electron dynamics is strongly affected by the dephasing processes. The dephasing processes make the electron dynamics incoherent and more irreversible. Since the electron dynamics completely determines the nonlinear optical response of the system, such as high harmonic generation, then the nonlinear optics of graphene QDs strongly depends on the dephasing processes.

The dephasing, which is introduced through relaxation of the nondiagonal elements of the density matrix, affects both the intensities of the high harmonics and the harmonic cutoff. With increasing the relaxation time, i.e., when the electron dynamics becomes more coherent, the intensities of harmonics increase. This can be attributed to the fact that for the coherent dynamics more paths can contribute to formation of high harmonics coherently, resulting in larger intensity.

The effect of relaxation on the harmonic cutoff is also related to the reversibility of electron dynamics. Namely, with increasing the relaxation time the electron dynamics becomes more reversible with less population of the highly excited quantum dot levels. As a result the harmonic cutoff decreases with increasing the relaxation time. As a function of the field amplitude, the harmonic cutoff shows almost linear dependence at small frequencies of the pulse when the corresponding energy cutoff is less than the energy range introduced by the lowest and the highest energy levels in the quantum dot. When this energy range becomes comparable to the energy cutoff, which happens at large frequencies of the pulse, then the

cutoff shows a saturated behavior as a function of the pulse amplitude.

For experimental verification of the high harmonic generation from graphene QDs, an array of QDs should be prepared to enhance the intensity of the corresponding radiation. The measurements can be done following the standard experimental setup, where the emitted radiation is routed to a spectrometer[84]. An array of graphene QDs can be also used for generation of high frequency optical pulses. Although the intensity of such pulses can be low, the pulses can be generated in the hard ultraviolet region.

# CHAPTER 4

# CHAPTER 4 HIGH HARMONIC GENERATION GOVERNED BY EDGE STATES IN TRIANGULAR GRAPHENE QUANTUM DOTS

This chapter investigates the role of zero energy in-gap edge states in triangular GQDs and how these edge states modify the HHG process on the zigzag-edged triangular GQDs, considering the cases having even and odd numbers of edge states. We studied the ultrafast electron dynamics in the triangular GQDs. We observed the significant suppression of even high-order harmonics in the triangular GQDs, which have an even number of edge states. The findings presented in this chapter are published in a Physical Review B journal titled High harmonic generation in triangular graphene quantum dots [85].

## 4.1 Introduction

Interaction of optical pulses with solids and gases is characterized by nonlinear effects, such as nonlinear absorption and high harmonic generation (HHG) [42; 43; 44; 18; 45; 46; 47; 48; 49].The generation of high harmonics, which is due to highly nonlinear electron dynamics in the field of the pulse, results in efficient frequency conversion, for example, conversion of visible light into extreme ultraviolet light. The HHG has been observed experimentally both in gases, i.e., in systems with randomly positioned atoms, and in solids, where the atoms have periodic spatial arrangements. The physics behind the generation of high harmonics in these two systems is different. HHG in gases occurs through a three-step process, which is a tunnel ionization of an electron, its acceleration in a laser field, and a subsequent recollision with the same atom [42; 50].In solids, the distance between the atoms is small

enough and the recollision after electron excitation can occur with a different atom. Also, in solids, the generation of high harmonics is usually described in terms of interband and intraband electron dynamics [18; 45; 46; 51; 52; 53].Within this picture, the field of a pulse redistributes electrons between the bands of a solid, which is described by the interband dynamics, and the excited electrons are transferred through the nonparabolic bands, which results in nonlinear intraband electron dynamics. The high harmonics are generated during both of these processes and depending on the band gap of a solid and the frequency of a pulse, either interband or intraband dynamics gives the main contribution to HHG. One of the differences in HHG in solids and gases is the dependence of the HHG energy cutoff on the amplitude of the pulse. While, for solids, such dependence is linear [18], for gases, the HHG energy cutoff has linear dependence on the pulse intensity [42].

To observe the high harmonics in solids, which are generated by a short optical pulse, the intensity of the pulse should be relatively large, with the corresponding amplitude that is comparable to internal electric fields in solids. Such strong and short pulses were intensively used to control the transport and optical properties of solids [27; 28; 29; 30; 31; 32; 33; 34; 35; 36; 37; 38; 39; 40]. Such control is determined by ultrafast nonlinear electron dynamics in the field of the pulse. The nonlinear electron dynamics and correspondingly the generation of high harmonics can be tuned by changing the band gap of the material, the level of the internal disorder, and also by changing the dimensionality of solids going from 3D to 2D, then to 1D, and finally to zero-dimensional systems. Zero-dimensional systems or quantum dots (QDs) [58; 59] have a finite size and a finite number of atoms of the corresponding

solid. They can be also considered as very large artificial atoms with quasiperiodic spatial structure. Due to dimensional quantization, the energy spectra of QDs are discrete, which results in unique optical properties of QDs and the possibility to use them as an energy storage [60; 61; 62; 63; 64]. Although the energy spectra of QDs are discrete; generally, the corresponding QDs' states can be identified as belonging to the conduction of valence bands of the original solid. The electron dynamics in a QD in the field of an optical pulse can be described as transitions between QD states. Thus, such a dynamics can be also described as a combination of intraband and interband dynamics. Generation of high harmonics in quantum dots is a manifestation of nonlinear features of both intraband and interband dynamics. For small QDs, electron transitions to continua that are similar to the ones in gases become important. Thus, by varying the size of a QD, it is possible to trace a transformation of a HHG spectrum from the atomic one to the crystalline solid one [65]. In Ref.[65], it was shown that such a transformation occurs for a QD that consists of just six atoms.

In addition to discrete energy spectra of QDs, QDs of topological materials can have some other interesting features. Namely, under some conditions, there are in-gap edge states, which can change the nonlinear optical response of such QDs. One of the topological materials with nontrivial in-gap edge states is graphene [66; 67; 68; 69]. Graphene is a monolayer of carbon atoms with honeycomb crystal structure [70; 71], which results in a specific relativistic low-energy dispersion of the Dirac type [72; 73; 74; 75]. A graphene monolayer placed in a strong optical pulse shows interference patterns in the conduction band population distribution in the reciprocal space [76]. When the inversion symmetry of graphene is broken, e.g., in

graphene-like materials such as transition-metal dichalcogenides, an ultrashort circularly polarized optical pulse produces a finite residual valley polarization [37; 77]. In graphene QDs, the nonlinear optical response, which depends on the size and the shape of QDs, is also expected. For example, the nonlinear absorption by graphene QDs of different sizes has been reported theoretically in Ref. [78], while the HHG from a small hexagonal graphene QD with just 24 atoms has been studied numerically in Ref. [26], where the dependence of the HHG spectra on the relaxation rate has been reported. In graphene QDs considered in Ref. [26], there are no edge states due to the hexagonal shape of the QDs. At the same time, if a graphene QD has zigzag edges, then there are corresponding in-gap degenerate edge states. Such edge states can be populated by electrons, for example, by applying a gate potential. The population of the edge states follows the atomic physics Hund's rule, which is also valid for graphene QDs; see Ref. [86]. The dependence of HHG in CdSe and CdS quantum dots has been studied experimentally in Ref. [87] for quantum dots of small sizes, 2 and 3 nm.

In the present work, we consider nonlinear optical properties of graphene QDs with zigzag edges, which can be partially occupied. We characterize the nonlinear optical response of such graphene QDs in terms of HHG. The population of the in-gap edge states before the optical pulse increases the in-gap electron density, which can change the nonlinear electron dynamics in the field of the pulse and correspondingly affect the generation of high harmonics.

## 4.2 Results and Discussion

We consider graphene QDs of triangular shape with zigzag edges. Such QDs are shown in Fig. 4.1 for two QD sizes, with 22 and 46 atoms in the dot. The energy spectra of TGQDs are obtained within the tight-binding model and are shown in Fig. 4.2. For all sizes of QDs, the edge states are clearly visible. They have zero energy and are degenerate. The number of edge states depends on the size of TGQD, where for 22-atom and 46-atom QDs, the number of edge states is even, while for 33-atom QD, this number is odd. Below, we will mainly study the QDs with an even number of edge states. In QDs, due to dimensional quantization, the energy spectra have a finite band gap, which separates the valence and conduction band states. Here, we define the valence band states as the states with negative energies, while the conduction band states are the states with positive energies. For the sizes of the QDs that we consider below, the band gap between the conduction and valence band states is around 4 eV. There are also degenerate in-gap edge states with zero energy. The edge states are mainly localized near the edges of QDs. The triangular graphene QDs have $D_{3h}$ symmetry group, and the corresponding energy states are characterized by the irreducible representation of $D_{3h}$, which are 1D $A_1^{''}$ and $A_2^{''}$ and 2D $E^{''}$. All edge states belong to $A_2^{''}$ representation, while the bulk conduction band and valence band states are mainly $A_1^{''}$ and $E^{''}$. There is a strong dipole coupling between the edge states and lowest CB and VB states, which belong to either $A_1^{''}$ or $E^{''}$ representations.

The edge states lower the effective band gap, making it close to 2 eV. Each level in Fig. 4.4 is double-degenerate due to spin. Below, we are interested in the effects of edge state on the

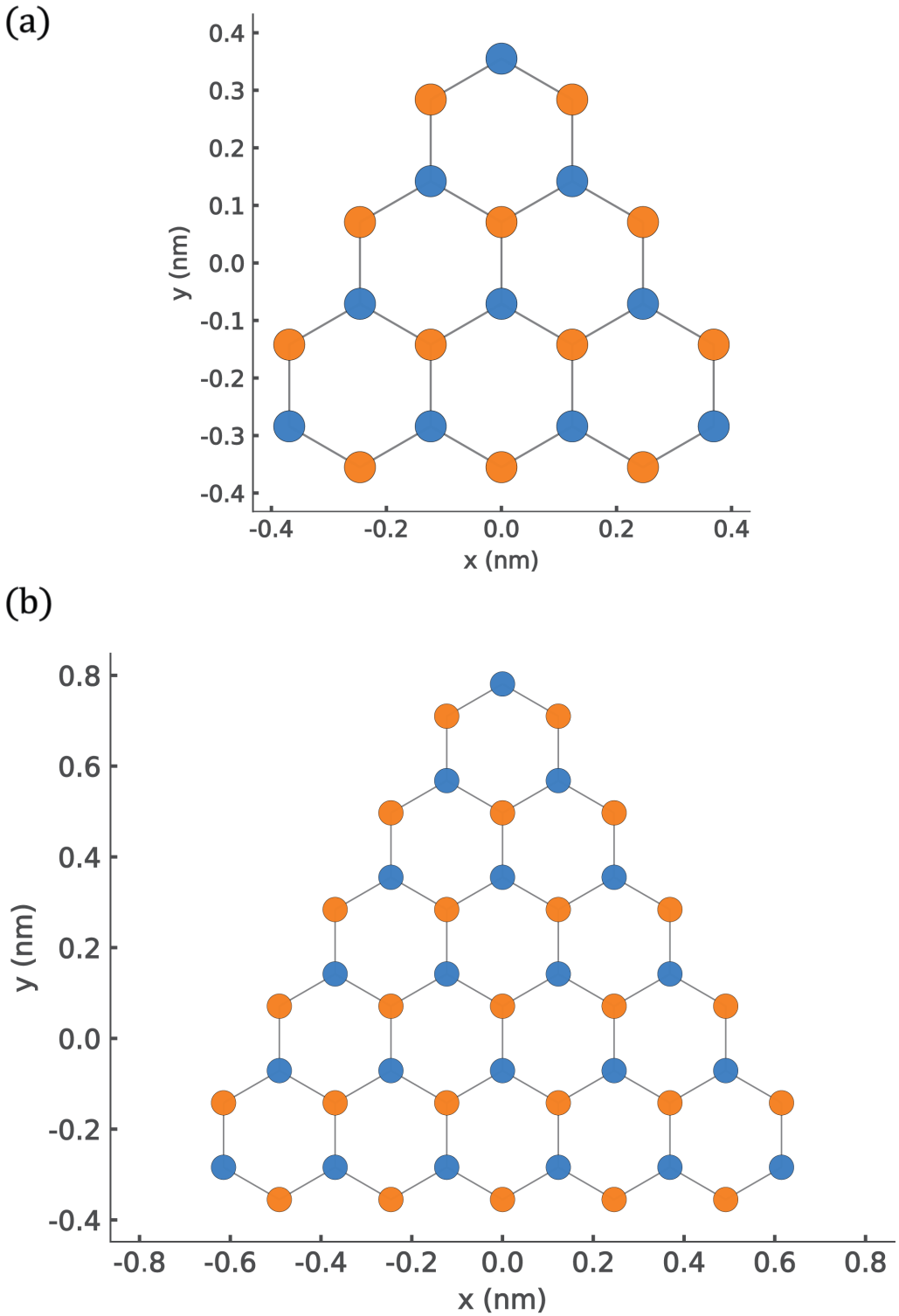


Figure 4.1 Triangular graphene quantum dots with zigzag edges. The quantum dots consist of 22 atoms (a) and 46 atoms (b). The distance between the nearest neighbor atoms is $a = 1.42$Å.

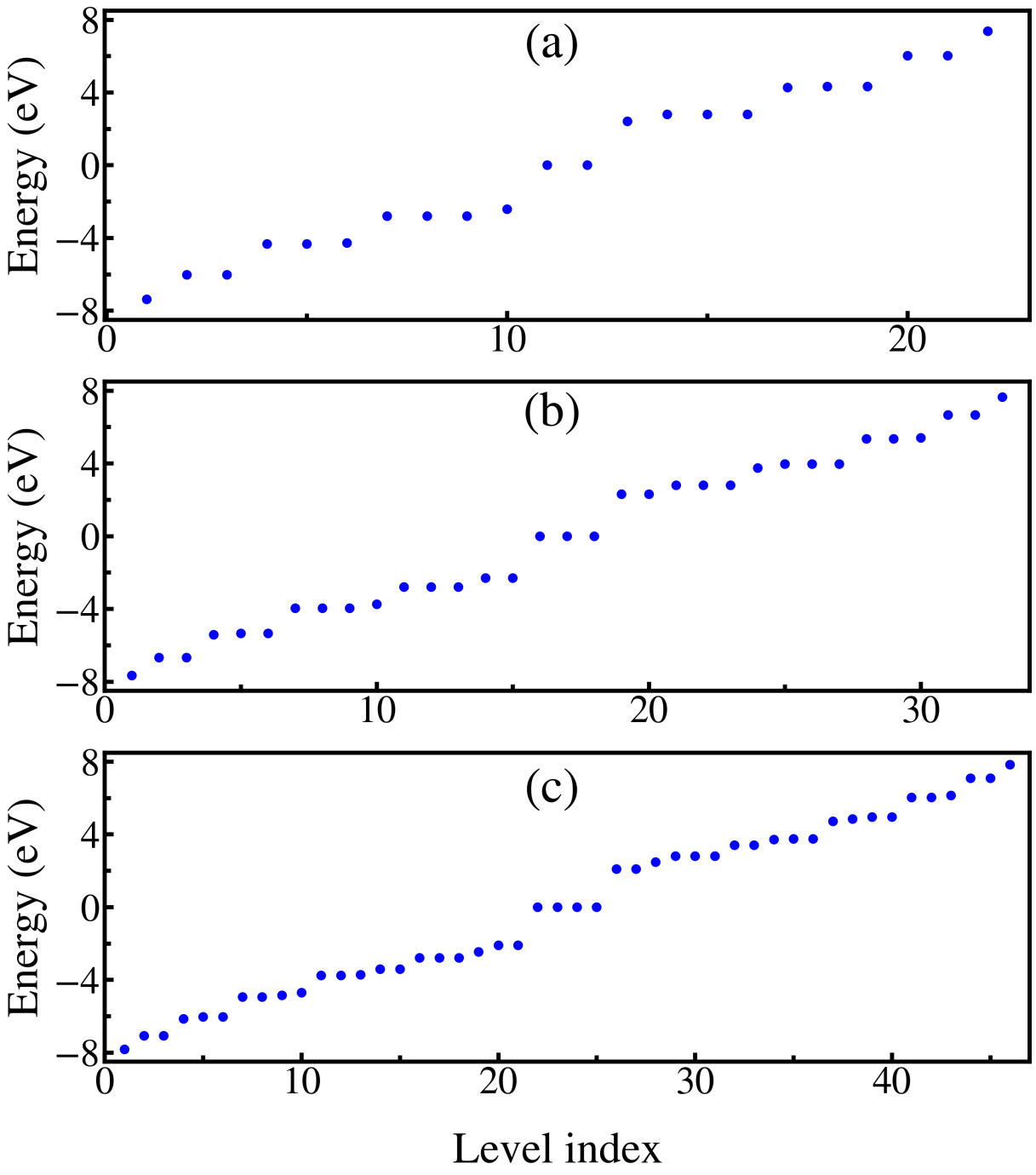


Figure 4.2 Energy spectra of TGQDs consisting of 22 atoms (a), 33 atoms (b), and 46 atoms (c). States with positive energies belong to the conduction band, states with negative energies correspond to the valence band, and zero-energy degenerate states are the edge states. The number of edge states is two, three, and four for 22-,33-, and 46-atom TGQDs, respectively.

nonlinear optical properties of TGQDs. Thus, we consider the cases when all valence band states are fully occupied and the in-gap edge states are partially occupied. Therefore, all valence band states, i.e., both spin-up and spin-down states, are occupied, and the population of the edge states follows the Hund's rule, which means that extra electrons first populate the degenerate edge states with one spin component, for example, a spin-up component. Thus, below, we consider the following situation: for a spin-down component, all valence band states are populated and edge states are empty, while for a spin-up component, all valence band states and $N_{PES}$ edge states are populated. We change the population of the edge states to see their effect on the nonlinear optical response of graphene QDs. Since the populations of the spin-down electron states remain the same; below, we study only the response due to spin-up states with variable populations of the edge states. For triangular graphene QDs shown in Fig. 4.1, only the $y$ axis is the axis of symmetry. In this case, if a linearly polarized incident optical pulse is $y$ polarized then the generated dipole moment has only the $y$ component, while if an incident pulse is x polarized, then both $x$ and $y$ components of the generated dipole moment are nonzero. First we analyze the response of the system to the pulse polarized in the $x$ direction. The profile of the corresponding electric field and the $x$ and $y$ components of the generated dipole moment are shown in Fig. 4.3. While the $x$ component of the dipole moment follows the profile of the electric field of the pulse, the y component of the dipole moment shows high-frequency oscillations.

The interaction of an optical pulse with the electron system of the TGQD results in a redistribution of electrons between the states of the TGQD. To characterize such a redis-

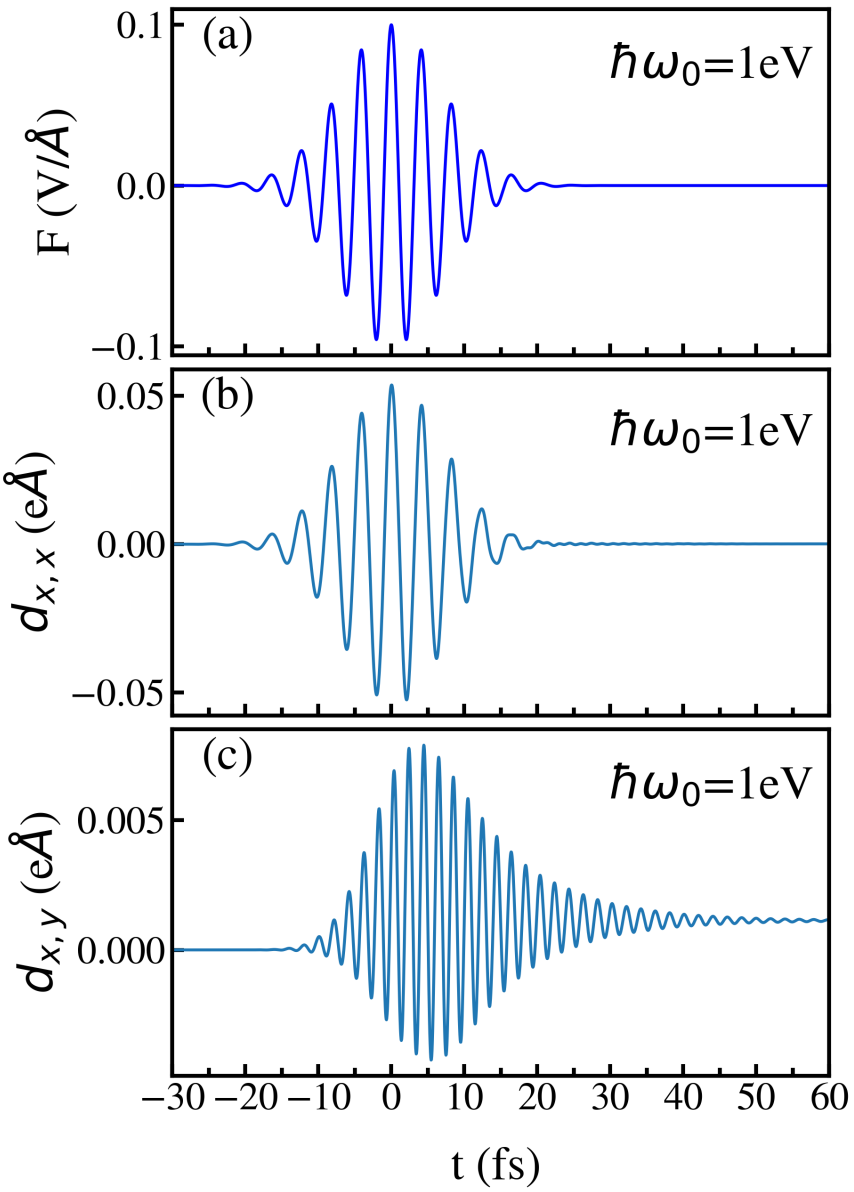


Figure 4.3 Panel (a): Profile of a linearly polarized optical pulse. The pulse amplitude is 0.1 V/Å, and the frequency is $\hbar\omega_0 = 1$ eV. The pulse is polarized in the $x$ direction.The corresponding generated dipole moment is shown in panels (b) ($x$ component) and (c) ($y$ component) as a function of time. The number of atoms in the quantum dot is 46. No edge states are populated before the pulse.

tribution, we introduce two characteristics that determine the electron populations of the excited states. The first one defines the number of excited electrons in the conduction band states,

$$N_{EE,CB}(t) = \sum_{m\in \mathrm{CB}} \tilde{\rho}_{mm}(t). \tag{4.1}$$

Here the sum is over all TGQD CB states.

Another characteristic of the level of excitation is defined as the number of excited electrons in CB states and in the initially empty edge states,

$$N_{EE}(t) = N_{EE,CB}(t) + \sum_{m\in \mathrm{ES},\ m\notin \mathrm{PES}} \tilde{\rho}_{mm}(t), \tag{4.2}$$

where $ES$ means the edge states and $PES$ means initially, i.e, before the pulse, populated edge states.

The strongest interlevel coupling and the corresponding interlevel electron transfer is realized between the states with the smallest energy separation, i.e., between the valence band states and the edge states and between the edge states and the conduction band states. Such couplings determine the leading contribution to the nonlinear electron dynamics in the field of the pulse. To illustrate this property we show in Fig. 4.4 the time-dependent populations $N_{EE}(t)$ and $N_{EE,CB}(t)$ for different values of $N_{PES}$. The results are shown for a 22-atom QD with two edge states but similar results are expected for other sizes of TGQD. When the edge states are not initially populated, see Fig. 4.4(a), then the main electron

transfer occurs between the valence band states and the edge states; i.e., the total population of the conduction band states is small, around 0.01, while the population of the edge states is relatively large, around 0.1. Here the number 0.1 describes the electron transfer to the two edge states, which means that the electron transfer to one edge state is 0.05. If only one edge state is populated, see Fig. 4.4(b), then the total number of electrons transferred to the conduction band is 0.05, which is similar to the number of electrons transferred from the valence band states to the edge states in case (a). If both edge states are occupied, see Fig. 4.4(c), then the number of electrons transferred from the edge states to the conduction band states is around 0.1, which is similar to the total number of electrons transferred from the valence band states to the edge states in case (a).

The strength of the interlevel electron transfer depends on the frequency of the pulse. In Fig. 4.5, the residual populations of the conduction band states and the edge states are shown for two different frequencies of the pulse and its different amplitudes. The QD consists of 22 atoms and has two edge states. Initially, all edge states are populated. For all parameters of the pulse, the residual populations of the edge states remain the same, which means that the electron transfer from the edge states to the conduction band states is compensated by the electron transfer from the valence band states to the edge states. Also, for a larger frequency of the pulse, $\hbar\omega_0 = 2$ eV, which is almost in resonance with the edge states to the conduction band states transitions, the residual populations of the conduction band states are relatively large. As expected, mainly the lower-energy conduction band states are populated.

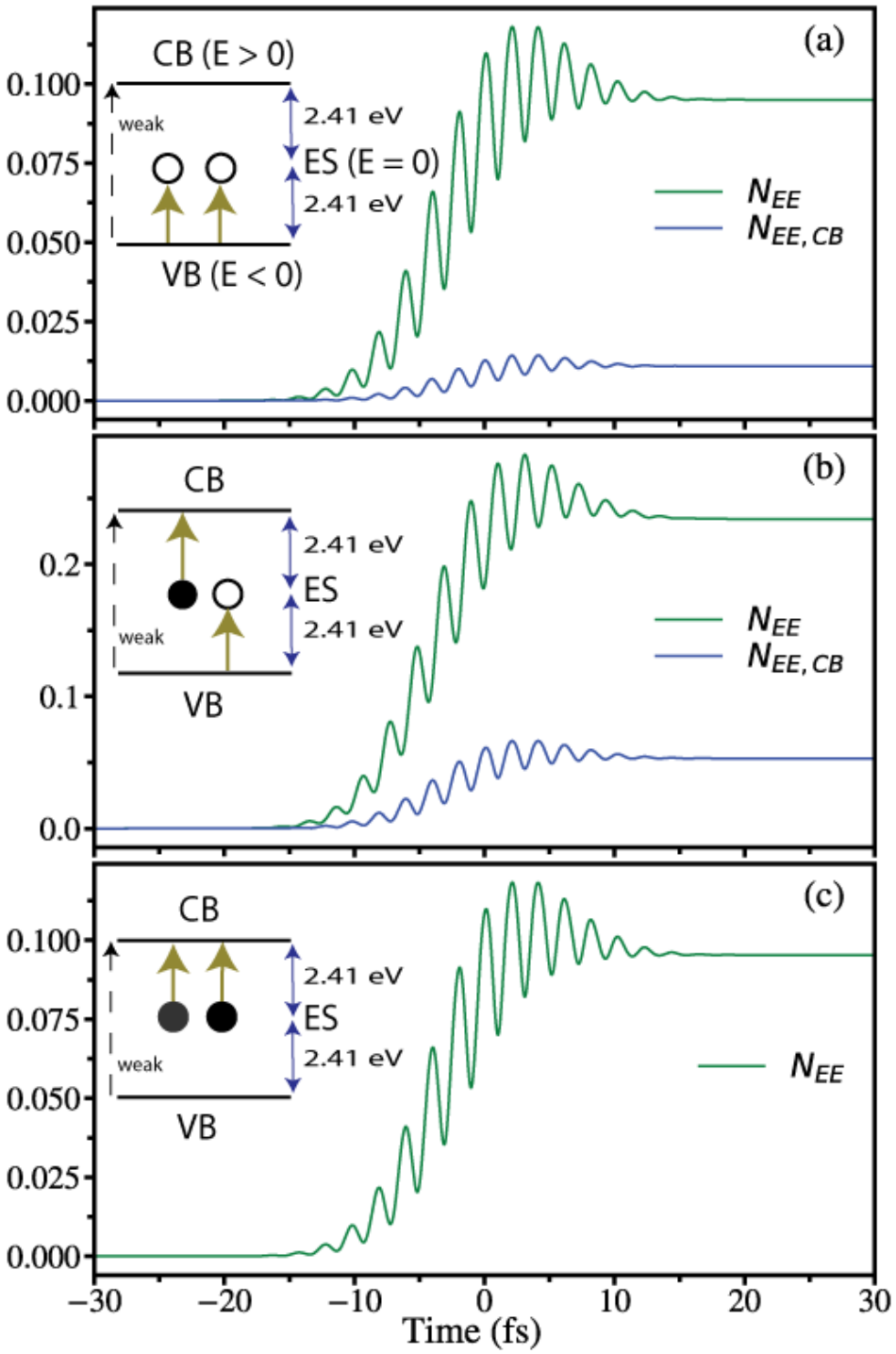


Figure 4.4 Population of the excited states,$N_{EE}$ and $N_{EE,CB}$, as a function of time. Panel (a): No edge states are initially populated. Panel (b): One edge state is populated before the pulse. Panel (c): All edge states are populated before the pulse. The filled dots in the inset represent the populated edge states, and the open dots describe the empty edge states. The frequency of the pulse is $\hbar\omega_0 = 1$ eV and the pulse amplitude is 0.3 V/Å.The number of atoms in the quantum dot is 22.

The emission spectra of TGQDs for a linearly polarized pulse in the x direction are shown in Fig. 4.6 for different sizes of TGQDs and different initial populations of the edge states. Due to the particle-hole symmetry of the system, the results when $N_{PES}$ and $N_{edge} - N_{PES}$ edge states are populated are the same. Here $N_{edge}$ is the total number of edge states. For example, for a 46-atom QD with four edge states, the emission spectra for the systems with 1 edge state populated and 3 edge states populated are identical. Therefore, in Fig. 6 and in all other figures below, only the data for $N_{PES} \leq N_{edge}/2$ are shown. The general tendency that can be seen in Fig. 4.6 is suppression of generation of even harmonics when the edge states are populated, i.e., when $N_{PES} > 0$. Such suppression is very strong when half of the edge states are initially populated. This is the case for 22-atom QDs with two edge states, see Fig. 4.6(a), where for $N_{PES} = 1$, there is a strong suppression of even harmonics compared to the NPES = 0 case. Also, for 46-atom QDs with four edge states, strong suppression of even harmonics is realized for $N_{PES} = 2$; see Fig. 4.6(c). Population of half of the edge states is possible only for the systems with even number of edge states, e.g., for 22-atom and 46-atom QDs, but not for 33-atom QDs with three edge states.

In Fig. 4.7, the HHG spectra are shown for the systems with even number of edge states and for different amplitudes of the optical pulse with the frequency of the pulse $\hbar\omega_0 = 1$ eV. For all cases, the even harmonics are strongly suppressed when the edge states are initially half filled. The suppression is more pronounced for smaller field amplitudes when mainly the lowenergy conduction band states are populated during the pulse and strongly contribute to generation of high harmonics. Thus, the suppression of high harmonics is mainly determined

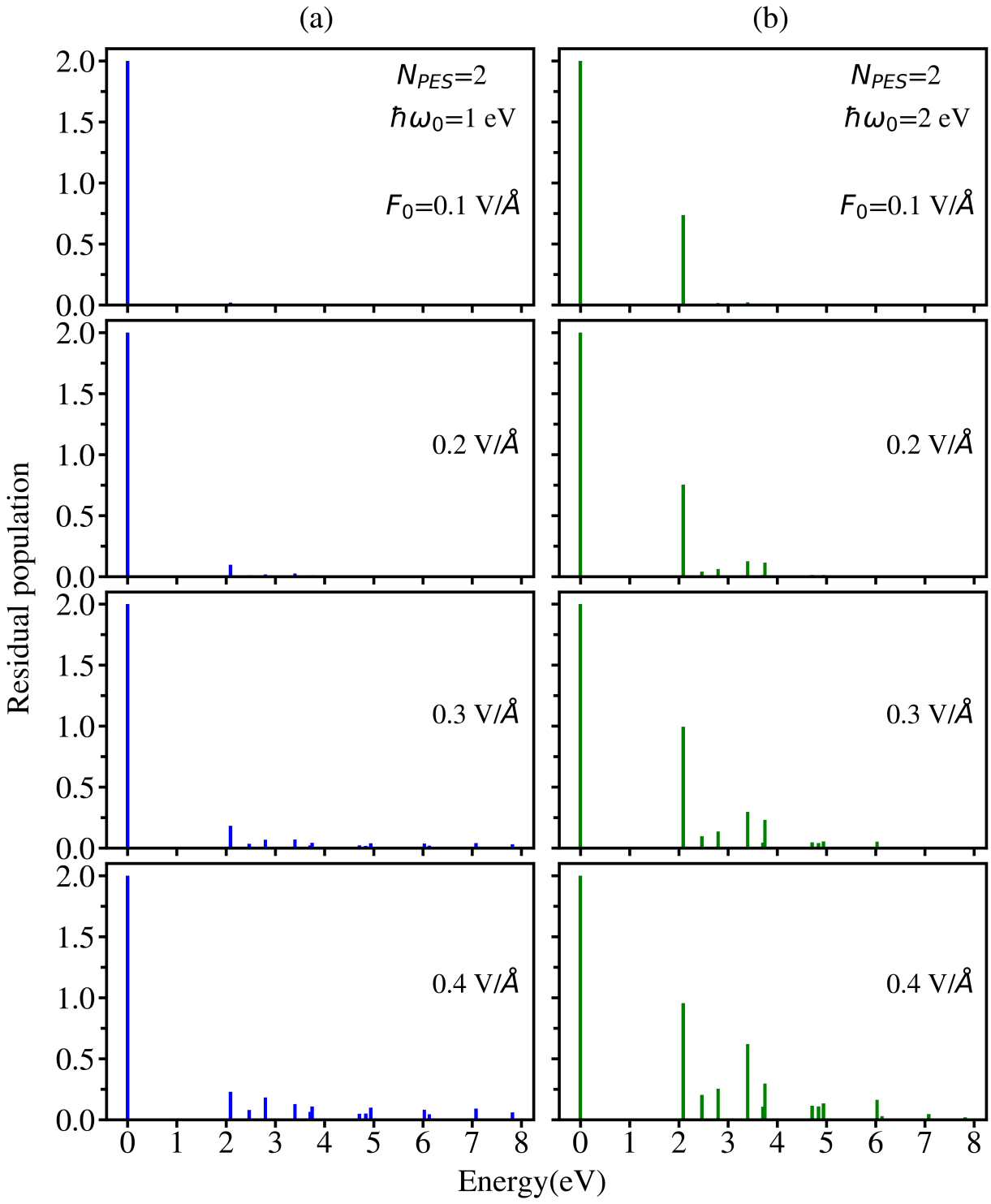


Figure 4.5 Residual population of conduction band states and two edge states. Two edge states are populated before the pulse. The number of atoms in TGQD is 46. The corresponding pulse amplitude is marked in each panel.The frequency of the pulse is $\hbar\omega_0 = 1$ eV (a) and $\hbar\omega_0 = 2$ eV (b).

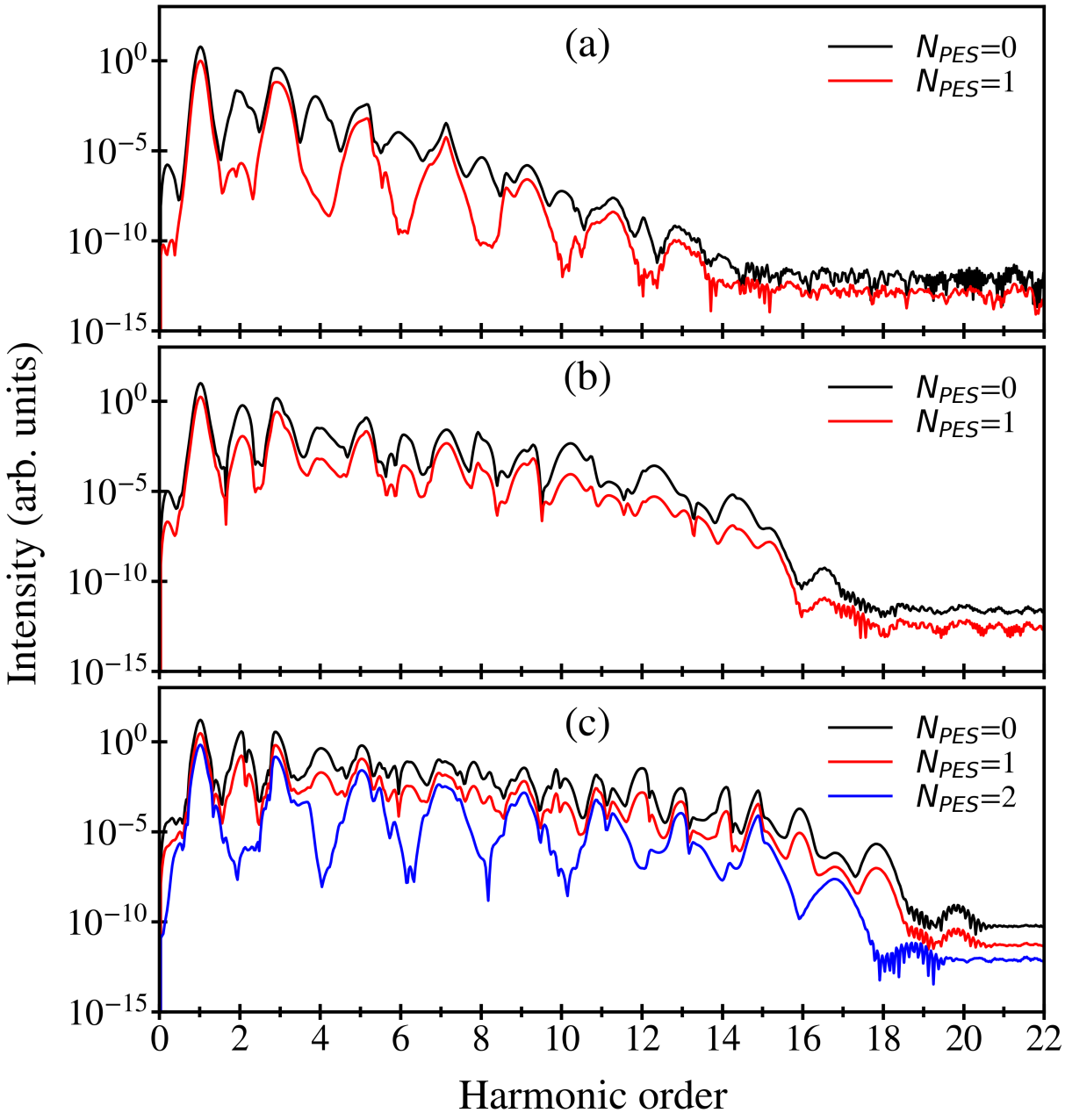


Figure 4.6 Emission spectra of TGQDs: The number of atoms in the dot is 22 (a), 33 (b), and 46(c). High harmonics with well-defined cutoffs are clearly visible in each spectrum. The number of populated edge states are marked for each graph. The frequency of the pulse is $\hbar\omega_0 = 1$ eV. The dephasing time is $\tau = 10$ fs. An offset was introduced to make the plotted data more readable.

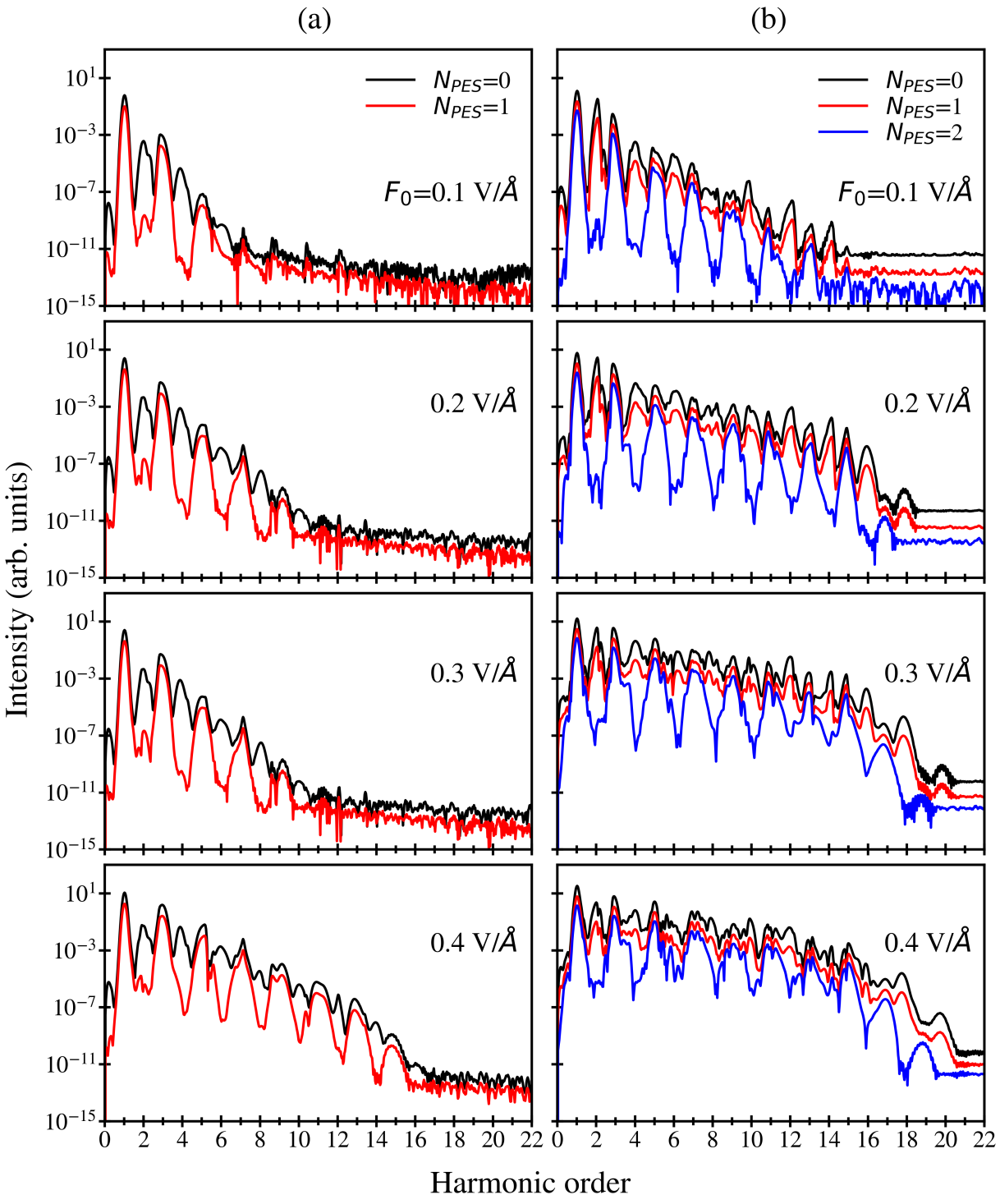


Figure 4.7 Emission spectra of TGQDs: The number of atoms is 22 (a) and 46 (b). High harmonics with well-defined cutoffs are clearly visible in the spectra. The corresponding populated edge states are marked for each graph. The frequency of the pulse is $\hbar\omega_0 = 1$ eV. With the increasing size of the TGQDs, the number of harmonics, as well as the cutoff frequency, increases. The dephasing time is $\tau = 10$ fs.An offset was introduced to make the plotted data more readable.

by the lower-energy conduction band states. Since the population of the conduction band states during the pulse is sensitive to the frequency of the pulse, i.e., at higher frequencies, which are closer to the band gap, more conduction band states are populated during the pulse, the suppression of high harmonics should be sensitive to the frequency of the incident pulse. In Fig. 4.8, the radiation spectra are shown for incident pulses with the frequencies that are comparable to the interlevel energy separation between the edge states and the conduction band states. In this case, the suppression of even harmonics at half-filling of the edge states is not that strong compared to the low-frequency pulses, and the peaks corresponding to even harmonics are clearly visible. For such frequencies of the pulse, there is a relatively strong population of high-energy conduction band levels during the pulse. Also, similarly to a low-frequency pulse, suppression of even harmonics becomes less pronounced for high field amplitude. Thus, the suppression of even harmonics, when half of the edge states are populated, is less pronounced when high-energy conduction band levels are excited during the pulse, which happens when the frequency of the pulse is close to the resonant condition or when the amplitude of the pulse is large.

The total radiation spectra produced by TGQDs have two contributions, which come from the $x$ and $y$ components of the dipole moment. Since for a TGQD only the $y$ axis is the axis of symmetry, the pulse polarized in the $x$ direction generates the dipole moment, which has both the $x$ and $y$ components. The corresponding contributions, $I_{x,x}$ and $I_{x,y}$, to the radiation spectra are shown in Fig. 4.9 for a 46-atom QD and different initial populations of the edge states. Here, $I_{x,x}$ is determined by the $x$ component of the dipole moment, while

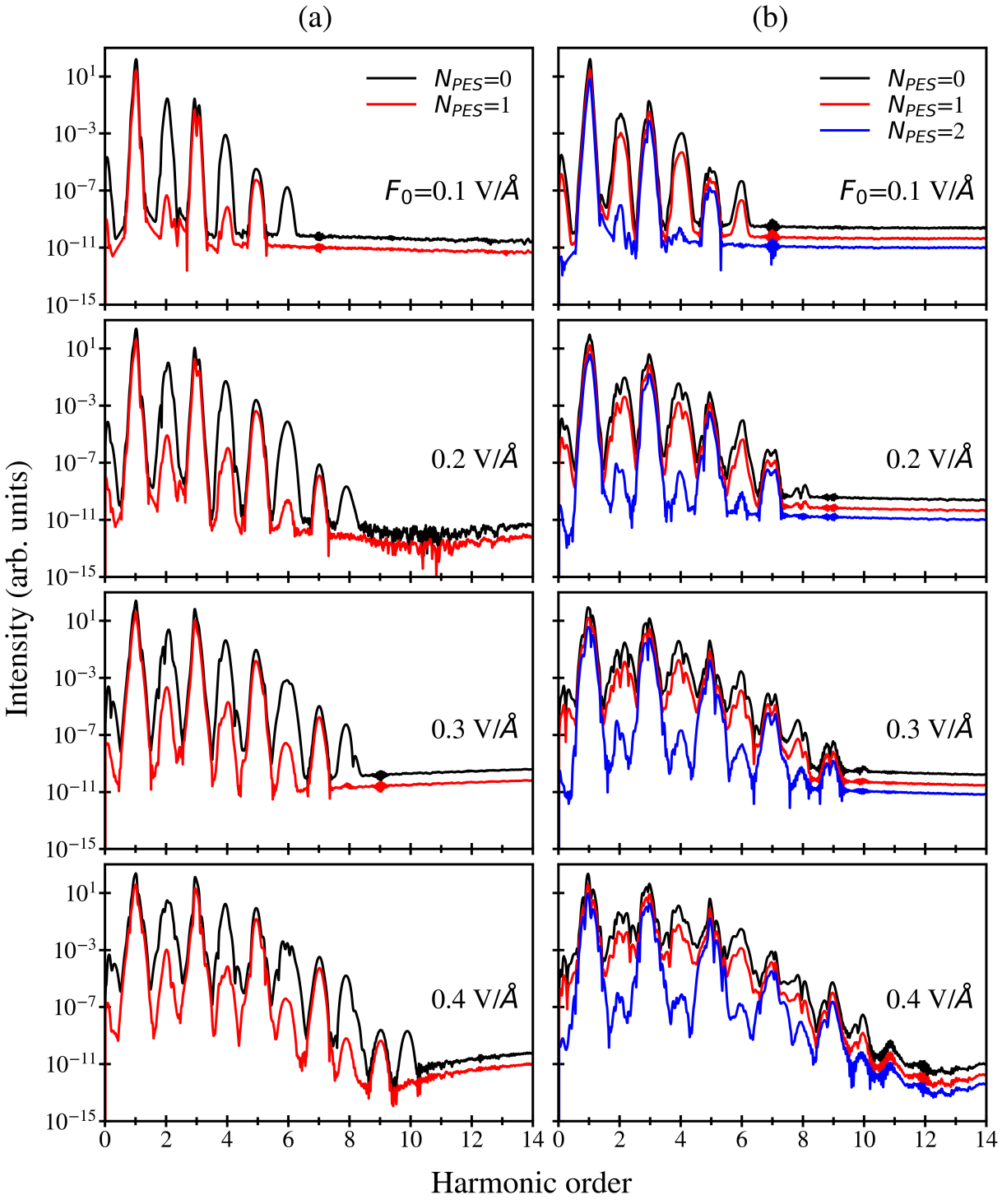


Figure 4.8 Emission spectra of TGQDs: Column (a) corresponds to 22-atom TGQD, while column (b) describes 46-atom TGQD.The number of populated edge states are marked for each graph. The amplitudes of the optical pulses are also shown in each panel. The frequency of the pulse is $\hbar\omega_0 = 2.3$ eV in column (a) and $\hbar\omega_0 = 2$ eV in column (b). With the increasing size of the TGQDs, the number of harmonics generated harmonics increases. The dephasing time is $\tau = 10$ fs.An offset was introduced to make the plotted data more readable.

$I_{x,y}$ is due to the $y$ component of the dipole moment. Since the y axis is the axis of symmetry of the system, then $I_{x,x}$ has only odd harmonics, see black lines in Fig. 4.9, and $I_{x,y}$ shows only even harmonics, see red lines in Fig. 4.9. In general, both contributions, $I_{x,x}$ and $I_{x,y}$, have comparable magnitudes, see Figs. 4.9(a) and 4.9(b) where $N_{PES} = 0$ and $N_{PES} = 1$, which results in comparable intensities of both even and odd harmonics in the total radiation spectra. When half of the edge states are populated, see Fig. 4.9(c), then $I_{x,y}$ becomes strongly suppressed, which results in suppression of the intensities of even harmonics in the total radiation spectrum.

All the above results correspond to optical pulses polarized along the $x$direction. For a pulse polarized along the $y$ direction, which is the axis of symmetry of the system, only the $y$ component of the dipole moment is generated during the pulse, while the $x$ component is zero. In general, for a pulse polarized in the $y$ direction, all high harmonic orders are generated. At the same time, similar to the case of a pulse polarized in the $x$ direction, when the edge states are half filled, the even harmonics are strongly suppressed. In Fig. 4.10, we present a comparison of the results for two polarizations of the incident pulse: $x$ and $y$. For all cases, for the low harmonics, the radiation spectra are very similar with comparable intensities. For high harmonics, the $x$-polarized pulse produces much more intense harmonics than the $y$-polarized pulse does. Also, the cutoff frequency is larger for the $x$-polarized pulse. Thus, the main difference between the $x$ and $y$polarized pulses is visible at harmonics with large frequencies, $> 10\omega_0$. The results in Fig. 4.10 are shown for the pulse frequency of $\hbar\omega_0 = 1$ eV when harmonics of up to 20th order can be generated. For larger frequency of the pulse,

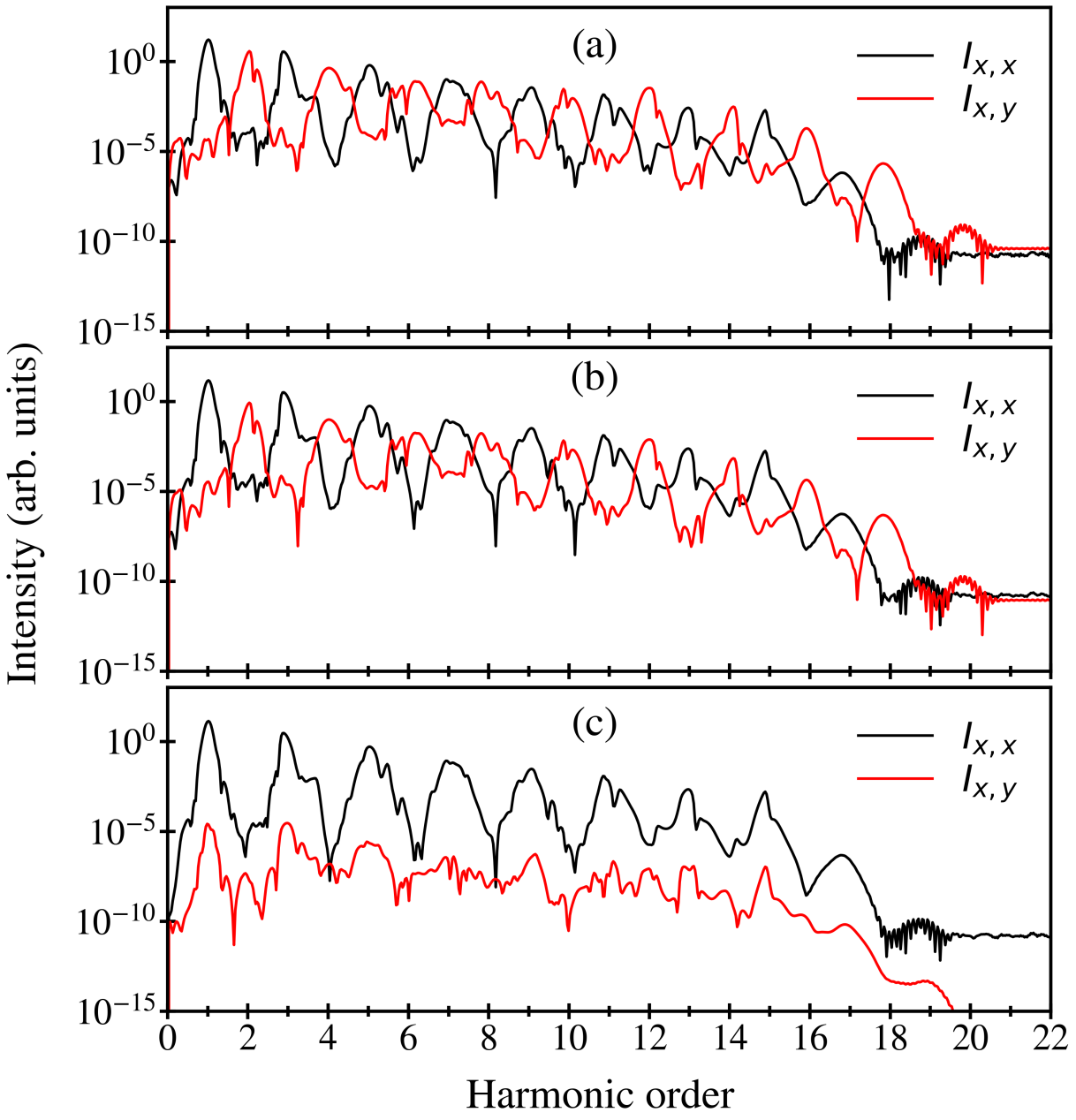


Figure 4.9 Radiation spectra due to $x$ and $y$ component of the dipole moment. The incident pulse is linearly polarized in the $x$ direction. The radiation spectra labeled by $I_{x,x}$ are determined by the $x$ component of the dipole moment, while the radiation spectra $I_{x,y}$ are due to the $y$ component of the dipole moment. The number of atoms in TGQD is 46. Panel (a): No edge states are populated; panel (b): one edge state is populated; and panel(c): two edge states are populated before the pulse.The radiation spectra $I_{x,x}$ have only odd components, while radiation spectra $I_{x,y}$ have only even components. The contribution to the radiation spectra associated with the $y$ component of the dipole moment is suppressed significantly when two edge states are initially populated. The dephasing time is $\tau = 10$ fs. The frequency of the pulse is $\hbar\omega_0 = 1$ eV, and pulse amplitude is $F_0 = 0.3$ V/Å.

e.g., $\hbar\omega_0 = 2$ eV, the condition is close to the resonant one and a low number of harmonics is generated. In this case, the radiation spectra are almost the same for both $x$ and $y$ polarized pulses.

Suppression of even-order harmonics reported above occurs when the edges states of graphene QDs are half filled. Such a system also has a particle-hole symmetry. The edge states, which belong to the $A_2^{''}$ representation of the $D_{3h}$ symmetry group, are strongly coupled by a linearly polarized optical pulse to the lowest CB and the highest VB states, which belong to the $A_1^{''}$ and $E^{''}$ representations. At the same time, the direct dipole coupling between the CB and VB states with the same symmetry is suppressed. In this case, in the field of the pulse, the electron transfer from the VB to the CB states occurs through the edge states. Because of the particle-hole symmetry of the system, the amount of the electron transfer from the VB states to the edge states is the same as the corresponding transfer from the edge states to the CB states. Thus, during the pulse, the edge states stay half filled and effectively electrons are transferred between the highest-energy VB states and the lowest-energy CB states with the same symmetry. As a result, the $y$ component of the dipole moment, which is responsible for the even-order harmonics, is suppressed. Such suppression becomes less pronounced for the pulses with high frequency, when the coupling between the CB and the VB states occurs not only through the edge states but also directly between the states of different symmetries, i.e., $A_1^{''}$ and $E^{''}$. One of the important characteristics of the HHG is the harmonic cutoff, which is the maximum harmonic order that can be generated.

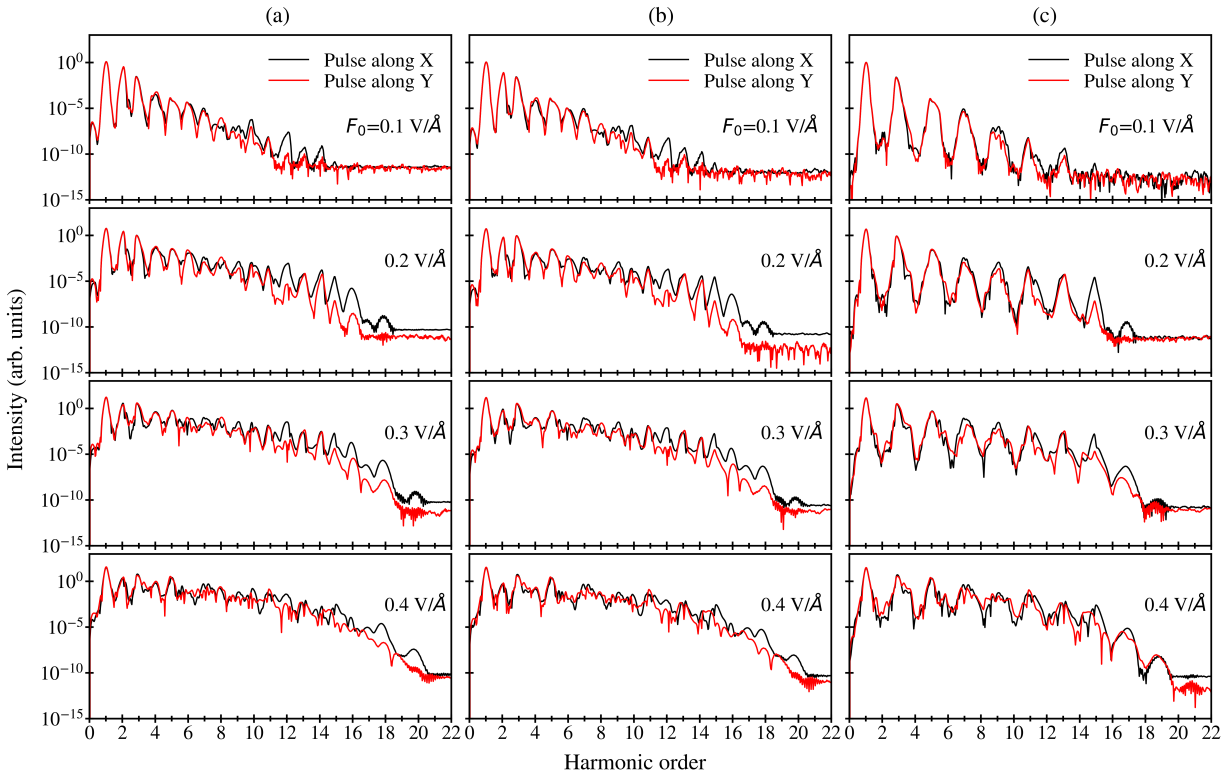


Figure 4.10 Radiation spectra of TGQD consisting of 46 atoms in the field of a linearly polarized pulse. The spectra corresponding to the pulses polarized along the $x$ and $y$ directions are shown by the red and black lines, respectively. The amplitudes of the corresponding optical pulses are shown in each panel. Different columns have different numbers of populated edge states before the pulse. Column: (a) No edge states are populated; column (b): one edge state is populated, and column(c): two edge states are populated. The frequency of the pulse is $\hbar\omega_0 = 1$ eV. The dephasing time is $= 10$ fs.

The cutoff frequency as a function of the field amplitude, $F_0$, is shown in Fig. 4.11 for different systems and different numbers of populated edge states. For almost all cases, the cutoff frequency has linear dependence on $F_0$. Such linear dependence is more clearly pronounced for high frequency of the incident pulse. Another property is that, generally, with increasing the initial population of the edge states the cutoff frequency decreases. This is due to decrease of the number of available states for electron excitations when the number of edge states increases. Also, with increasing size of the system, from 22 to 46, the cutoff

frequency monotonically increases, which is related to the corresponding increase in the number of electron states, both occupied and empty, in the QD system with increasing QD size.

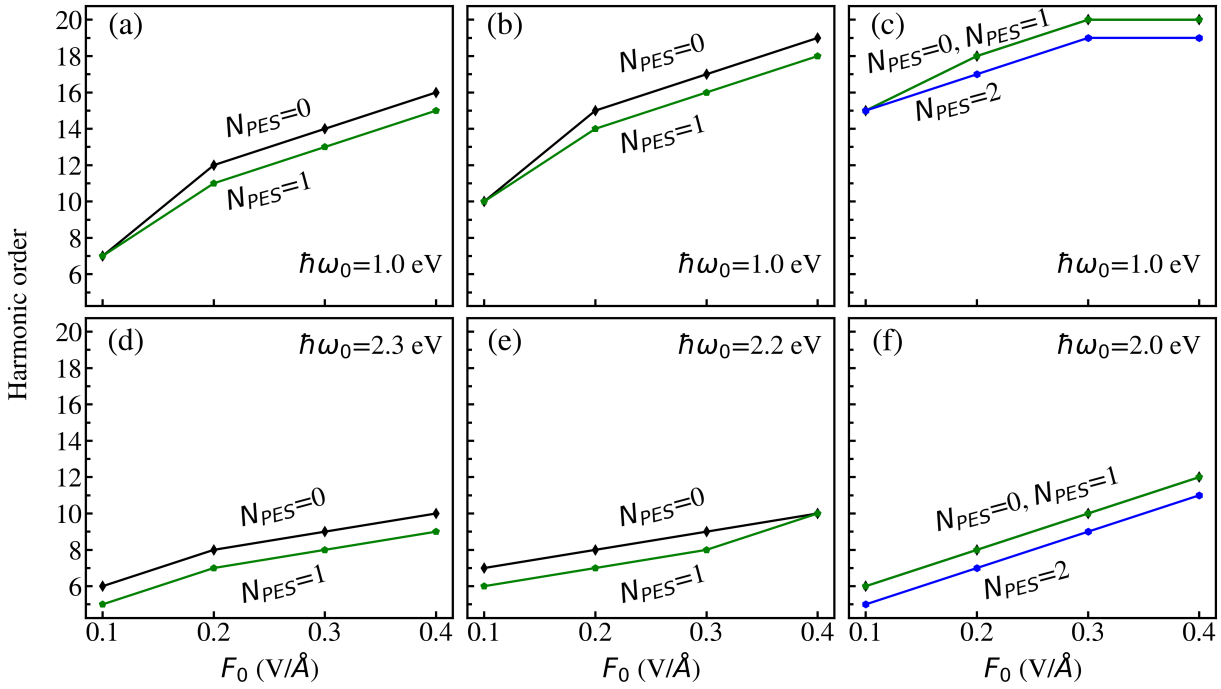


Figure 4.11 Harmonic cutoff versus the amplitude of the optical pulse. The frequency of the pulse is $\hbar\omega_0 = 1$ eV (a), (b) & (c) 2.3 eV (d) 2.2 eV (e) and 2 eV (f). The number of populated edge states is shown next to the corresponding line in each panel.

## 4.3 Conclusion

The radiation spectra of TGQDs placed in the field of an optical pulse depend on the size of the system and also on the parameters of the optical pulse, its amplitude, and frequency. Another characteristic of graphene QDs that can control the radiation spectrum and the corresponding generation of high harmonics is an initial electron population of QD edge states. Such edge states exist in graphene QDs with zigzag edges. Since the edge states in

such systems are in-gap states, they can strongly affect the generation of high harmonics. Namely, the generation of high harmonics depends on the number of initially occupied edge states. The strongest effect is observed for the systems, i.e., TGQDs with zigzag edges, which have an even number of edge states. In this case, if half of the edge states with the same spin component are initially populated then even high harmonics in the radiation spectra are suppressed. The level of suppression strongly depends on the frequency of the pulse. If the frequency of the pulse is close to the resonant condition, i.e., to the energy difference between the edge states and the conduction band states, then the even harmonics are weakly suppressed and the corresponding peaks in the emission spectra are clearly visible. But if the frequency of the pulse is small and far from the resonant condition, then suppression of even harmonics is strong with almost no peaks visible in radiation spectra at even frequencies.

The suppression of even harmonics at half-filled edge states is almost the same for different polarizations of the incident pulse, i.e., for $x$ and $y$ linearly polarized pulses.

Strong suppression of even harmonics in radiation spectra of TGQDs at a specific filling of TGQD edge states opens the possibility of control of the intensity of high harmonics by variation of gate voltage.

# CHAPTER 5

# CHAPTER 5 HIGH HARMONIC GENERATION IN GRAPHENE QUANTUM DOTS IN THE FIELD OF ELLIPTICALLY POLARIZED PULSE

This chapter aims to understand how the polarization of the incident optical field changes the electron dynamics, spectra of high-order harmonics, and high energy cutoff in GQDs having hexagonal and triangular geometry by varying the strength and ellipticity of the incident of the optical field. We observed the significant symmetry-related suppression of harmonics in hexagonal and triangular geometry when polarization approaches circular one while tuning the polarization of incident light from linear to circular. The findings presented in this chapter are published in a Physical Review B journal titled High-order harmonic generation in graphene quantum dots in the field of an elliptically polarized pulse [88].

## 5.1 Introduction

There has been growing interest in theoretical and experimental studies of optical nonlinearities of solids, including high harmonic generation (HHG), nonlinear absorption and scattering, and others[89; 90; 84; 91; 92; 93; 94; 95; 96; 97; 98; 45]. Recently, HHG in two-dimensional (2D) materials, including graphene[99; 100; 101; 102] and transition metal dichalcogenides[103], has drawn much attention due to their promising optical and electronic properties compared to three-dimensional solids. Several nanostructures, including graphene quantum dots (GQDs) [104] and graphene nanoribbons [105], were studied extensively to overcome the limitation due to lack of bandgap in semimetallic graphene. Bandgap tunability in GQDs can be achieved by varying lateral shape, size, and the type of the

edge, making GQDs more suitable for nonlinear optical systems[106]. The generation of high harmonics and its dependence on relaxation processes has been reported numerically in hexagonal GQDs with just 24 atoms [26]. Recent studies have also reported that HHG in GQDs with triangular[107; 85] and rectangular[108] geometries shows several exciting properties. Namely, in ref. [85], strong suppression of even-order harmonics has been reported in triangular GQDs, which have an even number of edge states. The suppression of even harmonics is realized when half of the edge states are initially, i.e., before the pulse, occupied.

While the HHG is mainly studied for linearly polarized optical pulses, general polarization of the incident optical pulse, e.g., elliptical polarization, provides unique opportunities to explore, investigate, and control strong light-matter interactions in solids and tune their nonlinear optical response. The polarization degree of freedom enables excellent insight into the study of the fundamental aspects of light-matter interaction and time-varying polarization states, which further opens the door to control attoscience coherent techniques, including spectroscopy, and would be a great candidate to control tabletop harmonic processes, including ultraviolet and X-ray spectral regions [109; 110; 111]. Recently, the dependence of HHG on the ellipticity of an incident pulse was used to probe the molecular chirality on a subfemtosecond timescale[112]. Furthermore, elliptical polarization enables the gating schemes, including polarization gating and double optical gating, to generate attosecond XUV pulses, which study the electron dynamics in atoms, molecules, and solids [113; 114; 115].

The elliptical polarization of the laser driver field has opened up several interesting physical phenomena in gases. In contrast, interactions of such pulses with nanosystems of solids

are largely unexplored, hindering the possibility of exploitation of experimental techniques to solid-state devices [111]. Therefore, studying the ellipticity dependence of light-matter interactions in 2D materials and their quantum dots would open new insight into the nonlinear optical properties of these systems.

In 2011, Ghimire et al. reported through an experimental study of bulk ZnO system that emitted high-order harmonics are less sensitive to ellipticity [18] of the optical pulse compared to the case of gases[116; 117]. However, under circular polarization of the incident pulse, the generation of high harmonics is strongly suppressed despite strong field ionization[18]. Later, Liu et al., under theoretical study of the same material, showed a monotonic decrease in harmonic yield with increasing ellipticity of the driving pulse[118].

On the contrary, experimental work on MgO system revealed a strong dependence of HHG yield on the ellipticity of the incident pulse, including a significant signal for a circular polarization[119]. The authors showed that the maximum harmonic yield, in some cases, can be reached not for a linear polarization but for a polarization with a finite value of the ellipticity. Later, an enhancement of HHG in graphene by elliptically polarized driving pulse was also reported [120; 121]. Furthermore, circularly polarized extreme ultraviolet HHG in graphene is reported using first-principles simulation within a time-dependent density functional theory[122]. These results revealed that circularly polarized driver pulses do not permanently prohibit harmonic generation from specific crystals and 2D materials. There are some proposals for solids to explain maximum harmonic yield at a finite ellipticity of the incident pulse in a semimetal regime of the crystal[123].

Quantum dots are systems that have properties of both solids and atoms, i.e., they have discrete energy spectra, which are determined by the symmetry of the dots, and also they have quasi-spatial periodicity of solids. Interaction of such quantum dots with an incident optical pulse should be sensitive to the polarization of the pulse, i.e., its ellipticity. Here we consider a special type of quantum dots: graphene quantum dots. Such quantum dots can have different symmetries, e.g., triangular GQDs have $D_{3h}$ symmetry while hexagonal GQDs have $D_{6h}$ symmetry. The symmetry of the GQD determines its nonlinear optical response, e.g., by suppressing the generation of some harmonics. Below we study theoretically the nonlinear ultrafast dynamics of GQDs within the density matrix approach, which allows us to include the relaxation processes within the GQDs phenomenologically.

The rest of the chapter is organized as follows: The results are discussed in Section III and summarized in the concluding Section IV.

## 5.2 Results and Discussion

Below, we study two types of GQDs, hexagonal and triangular, which have different point symmetries. The corresponding GQDs are shown in Fig. 5.1. The hexagonal QD consists of 54 carbon atoms and has $D_{6h}$ symmetry, while the triangular QD has 61 atoms, and the corresponding symmetry is $D_{3h}$. The triangular QD also has zigzag edges. We consider only two sizes of QDs to identify the symmetry-related effects in the nonlinear optical response of the systems.

The energy spectra of the triangular and hexagonal QDs are shown in Fig. 5.2. Due

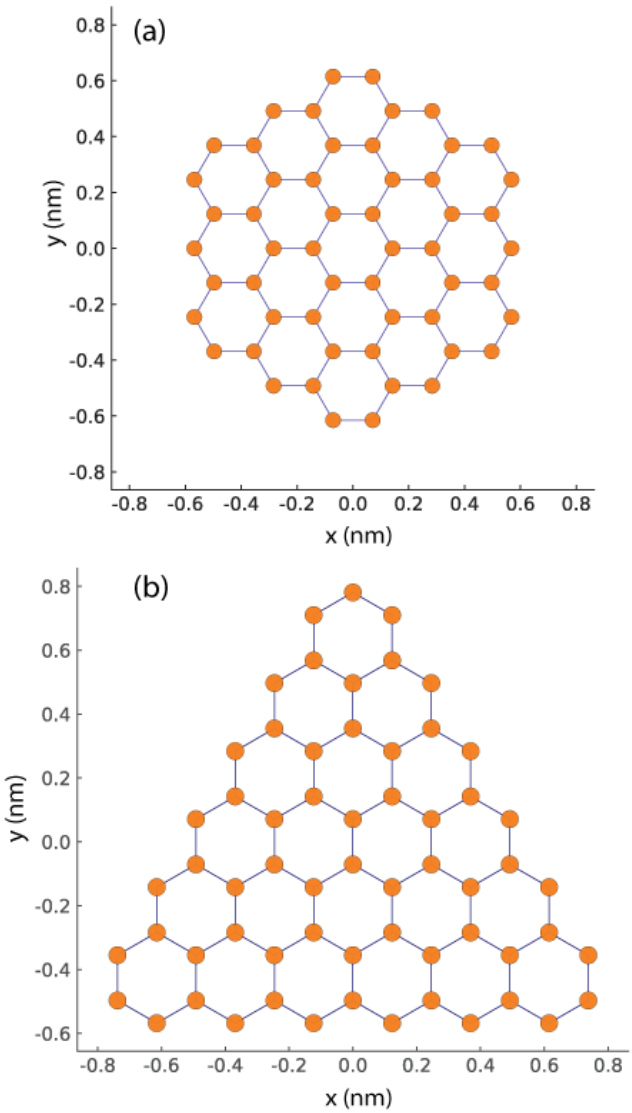


Figure 5.1 Hexagonal and triangular graphene quantum dots. The hexagonal dots consist of 54 atoms (a) and triangular dots possess 61 atoms (b). The distance between the nearest neighbor atoms is $a = 1.42$Å

to dimensional quantization, both systems have finite band gaps, which are 1.91 eV for the hexagonal QD and 1.87 eV for triangular QD. The triangular QD with zigzag edges also has degenerate in-gap edge states with zero energy,which are marked in Fig. 5.2. The bulk states of triangular and hexagonal GQDs belong to either one- or two-dimensional irreducible

representations of the corresponding symmetry groups, $D_{3h}$ and $D_{6h}$.

In all calculations below, we keep the same frequency of the pulse, 1 eV, which is less than the bandgap for both GQD systems. We change the amplitude $F_0$ of the pulse with the maximum amplitude up to 0.3 V/Å. The radiation spectra of triangular and hexagonal GQDs are shown in Fig. 5.3 for different ellipticity values of the incident pulse. The radiation spectra clearly follow the symmetries of the systems. No even-order harmonics are realized for the hexagonal QD, which has inversion symmetry, while for the triangular QD, both even-order and odd-order harmonics are clearly visible in the radiation spectrum. Another

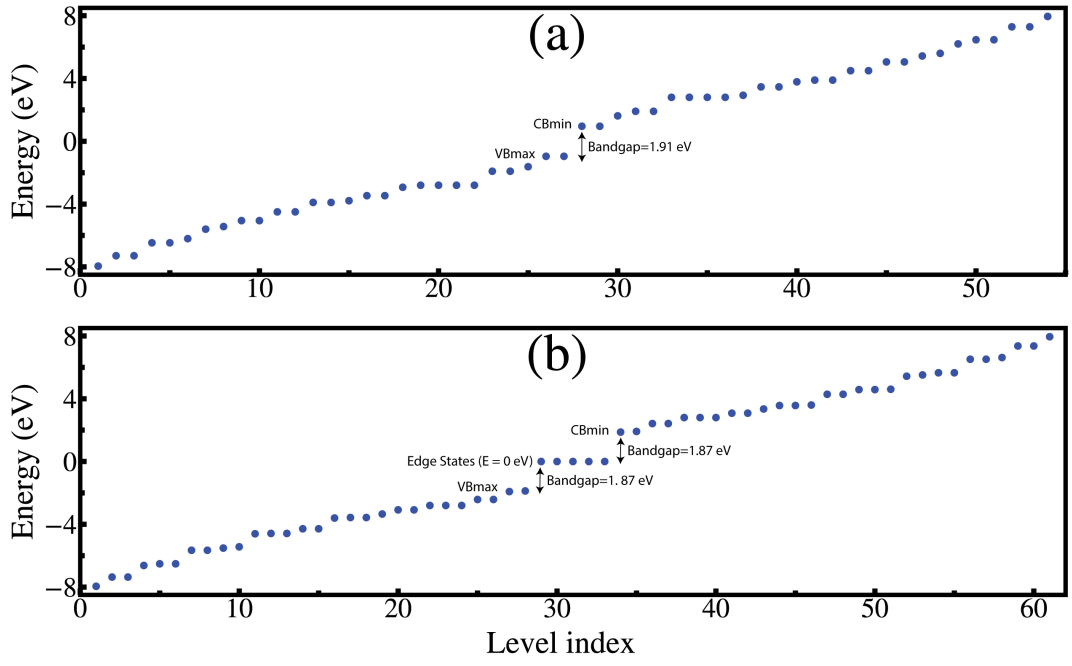


Figure 5.2 Energy spectra of hexagonal GQD (a), and triangular GQD (b). For the triangular QD, zero-energy states are edge states. The zero energy states near the Fermi energy surface correspond to edge states. Levels with negative and positive energies correspond to the valence band and conduction band states, respectively.

symmetry-related feature is a suppression of some high-order harmonics when the incident pulse becomes circularly polarized. Namely, the triangular GQD has $D_{3h}$ symmetry with the rotational element of $C_3$, and the orders of high harmonics that are suppressed are 3, 6, 9, ..., i.e., $3+3m$, where $m$ is an integer. The hexagonal GQD has $D_{6h}$ symmetry, which results in the suppression of high harmonics with orders 3, 9, 15, ..., i.e., $3+6m$, where $m$ is an integer. The suppression of the high-order harmonics is realized when the ellipticity becomes close to 1, which corresponds to a circularly polarized pulse. For all field amplitudes, the

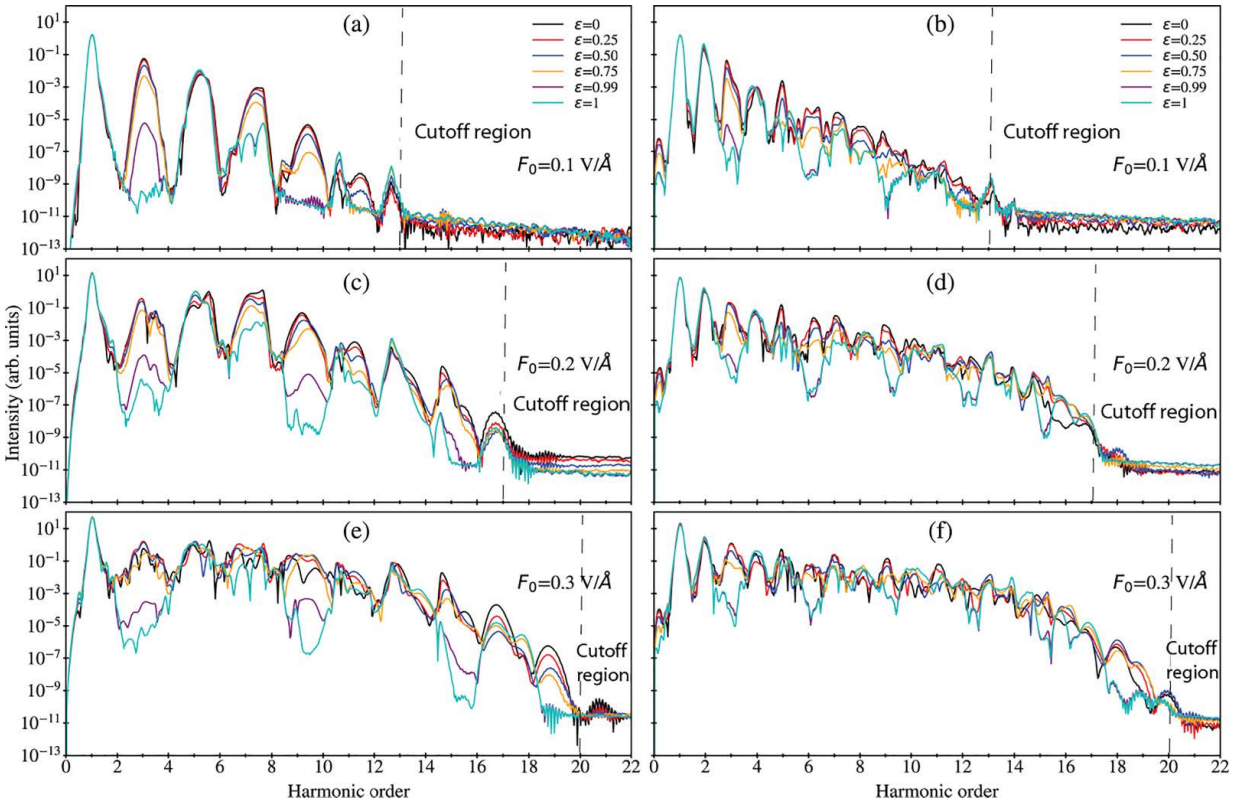


Figure 5.3 Emission spectra of graphene QDs: (a),(c), (e) hexagonal QD and (b),(d), (f) triangular QD. In each panel, different lines correspond to different ellipticities of the incident pulse. The pulse frequency is $\hbar\omega_0 = 1$ eV. The field amplitude of the incident pulse is $F_0 = 0.1$ V/Å(a), (b); 0.2 V/Å(c), (d); and 0.3 V/Å(e), (f). The dephasing time is $\tau = 10$ fs. The intensity is shown in the logarithmic scale.

suppression of the corresponding harmonics is clearly pronounced. Also, for the hexagonal QD, the harmonics orders of 6, 12, 18, and so on, i.e., even-order harmonics from the set of $3+3m$, are suppressed for all ellipticities due to the inversion symmetry of such a quantum dot. For high-order harmonics, which do not show suppression for a circularly polarized pulse, the dependence on the ellipticity of the incident pulse is weak. The cutoff frequency,

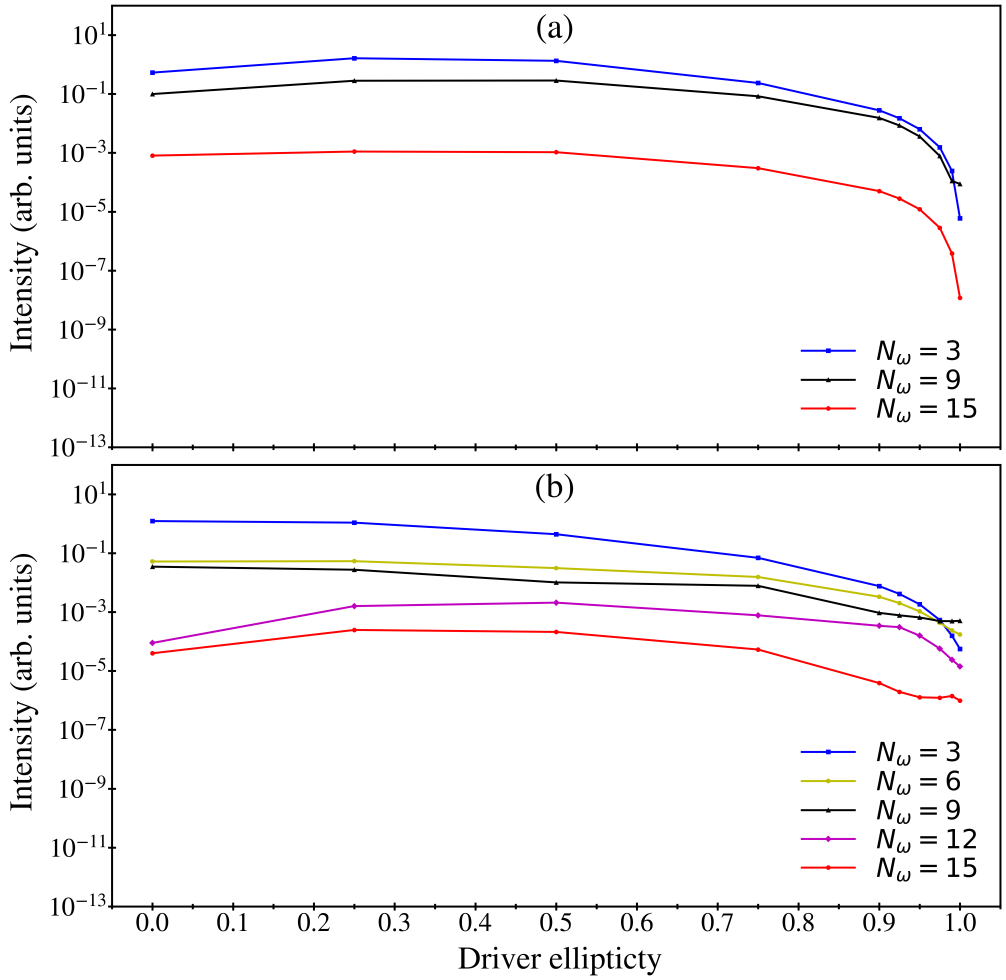


Figure 5.4 Intensities of high-order harmonics as a function of ellipticity of the incident pulse. The results are shown for (a) hexagonal QD and (b) triangular QD. The pulse frequency is $\hbar\omega_0 = 1$ eV, and its amplitude is 0.3 V/Å. The dephasing time is $\tau = 10$ fs. The results are shown for harmonics orders of 3, 9, and 15 in panel (a) and 3, 6, 9, 12, and 15 in panel (b) as marked. The intensity is shown on a logarithmic scale.

which is analyzed in detail below, also has a weak dependence on the ellipticity of the pulse. The emission spectra for different amplitudes of the optical pulse.

To illustrate the suppression of high-order harmonics for a circularly polarized pulse, we show in Fig. 5.4 the intensities of the first few high-order harmonics as functions of ellipticity

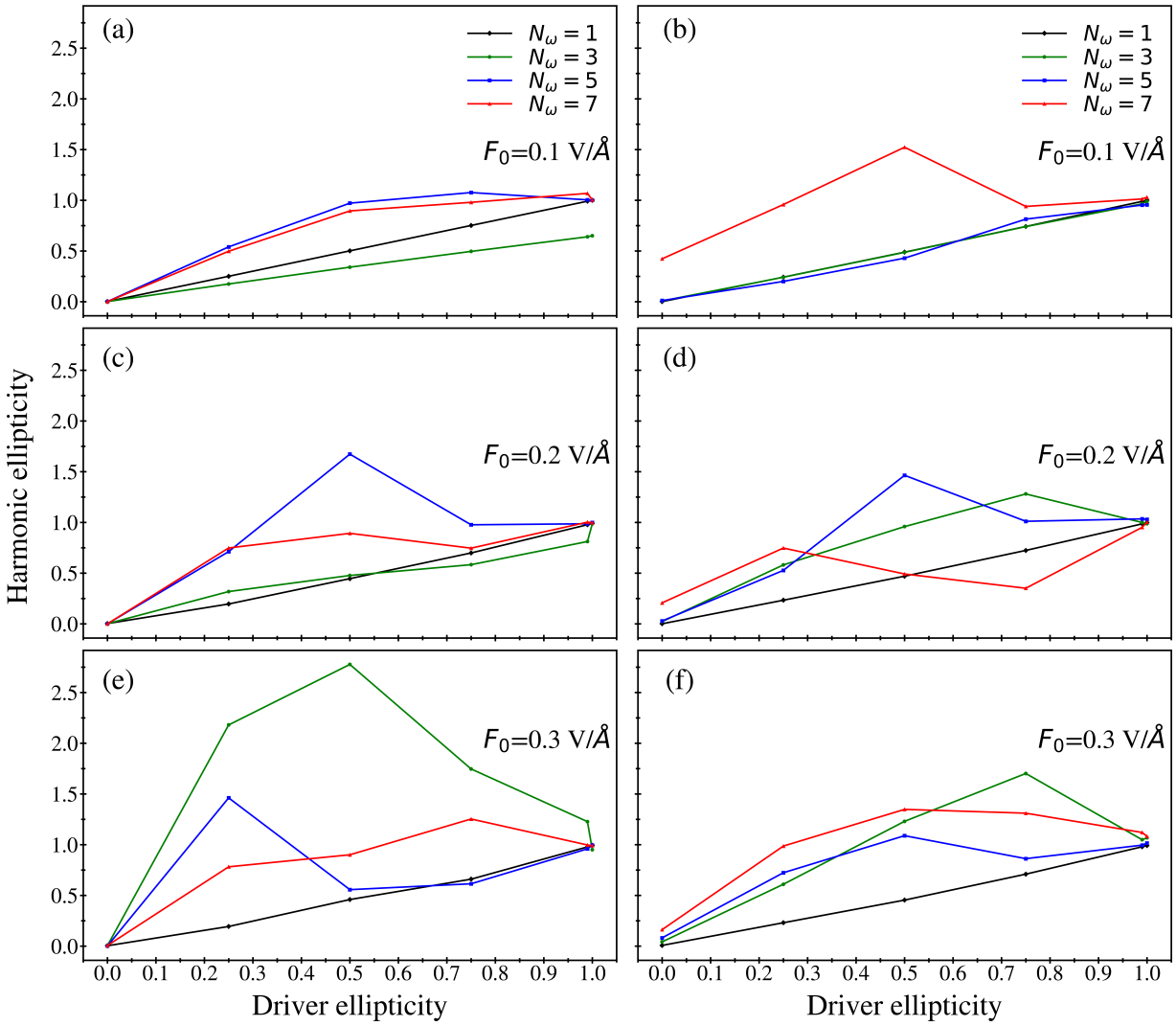


Figure 5.5 Ellipticities of the first four odd high order harmonics ($N_\omega$ =1, 3, 5, and 7) as a function of the ellipticity of the incident pulse. The results are shown for (a), (c), and (e) a hexagonal QD and (b), (d) and (f) triangular QD. The field amplitude is (a) and (b) 0.1 V/Å, (c) and (d) 0.2 V/Å, and (e) and (f) 0.3 V/Å. The pulse frequency is $\hbar\omega_0 = 1$ eV. The dephasing time is $\tau = 10$ fs.

of the incident pulse. The data show that the suppression of the corresponding harmonics occurs mainly in the range from $\epsilon > 0.9$. Suppression is less pronounced for the triangular QD, [see Fig. 5.4(b)], which has a larger number of atoms compared to the hexagonal QD. Namely, for the hexagonal QD, [see Fig. 5.4(a)], for all harmonics, the corresponding

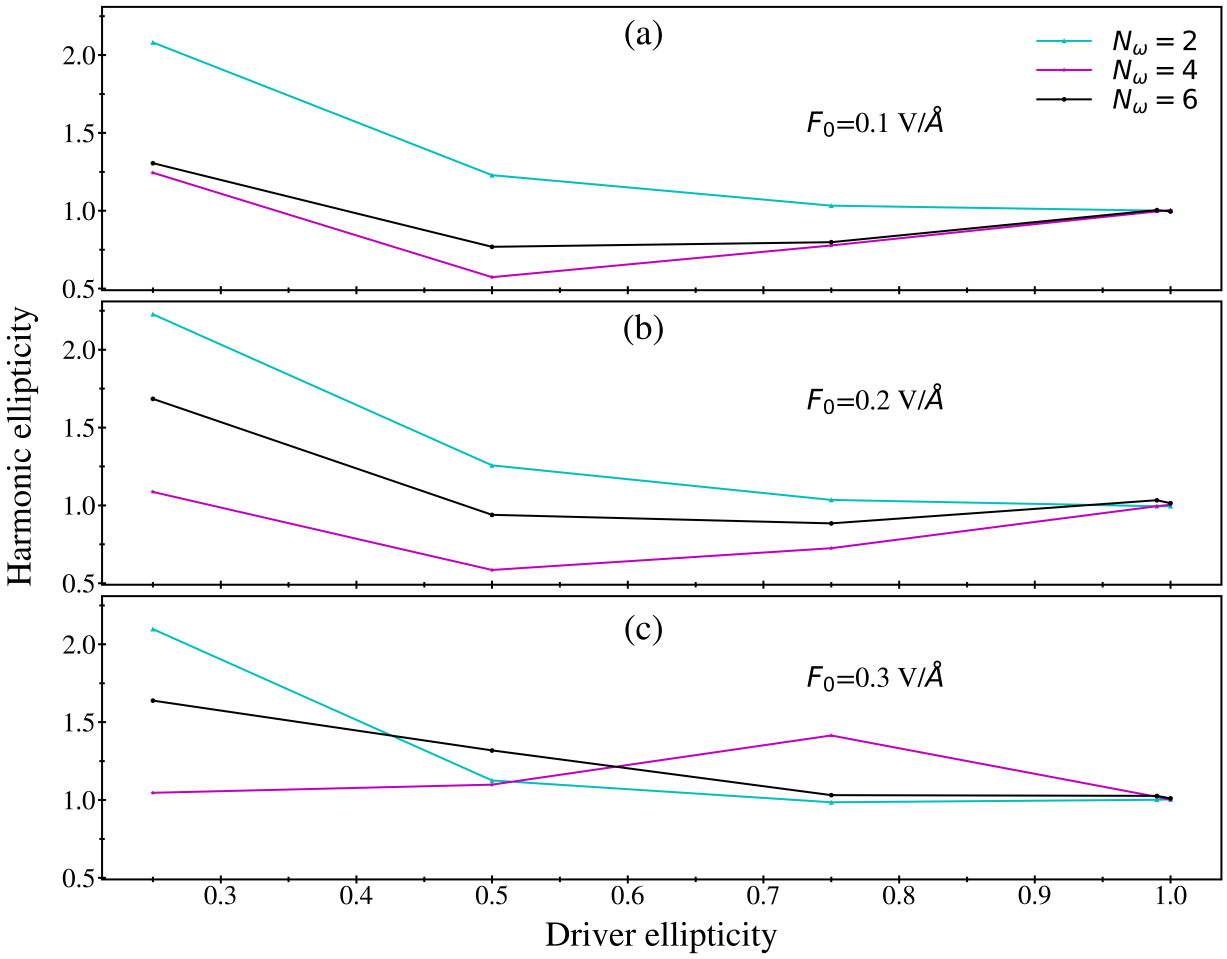


Figure 5.6 Ellipticities of the first three even order harmonics ($N_\omega$ =2, 4, and 6) as a function of the ellipticity of the incident pulse. The results are shown for triangular QD and the field amplitude of (a) 0.1 V/Å, (b) 0.2 V/Å, and (c) 0.3 V/Å. The data are shown only for the ellipticity, $\epsilon$, of the incident pulse greater than 0.2, while for small values of $\epsilon$, the ellipticities of the even harmonics are very large, illustrating the fact that for a linearly polarized pulse in the $x$ direction, the even harmonics are linearly polarized in the $y$ direction. The pulse frequency is $\hbar\omega_0 = 1$ eV. The dephasing time is $\tau = 10$ fs.

intensities are suppressed by 4-5 orders of magnitudes, while for the triangular QD, only the third-order harmonics is suppressed by 4 orders of magnitude and all other higher-order harmonics are suppressed by 2-3 orders of magnitude.

The emitted high harmonics are also elliptically polarized, and their polarization is characterized by the corresponding ellipticity. The dependence of the ellipticities of different high-order harmonics on the ellipticity of the incident pulse is shown in Fig. 5.5 for the first four odd harmonics ($N_\omega$=1, 3, 5, and 7). For a linearly polarized optical pulse, i.e., $\epsilon = 0$, the situation is different for the hexagonal and triangular QDs. For hexagonal QD [see Figs.

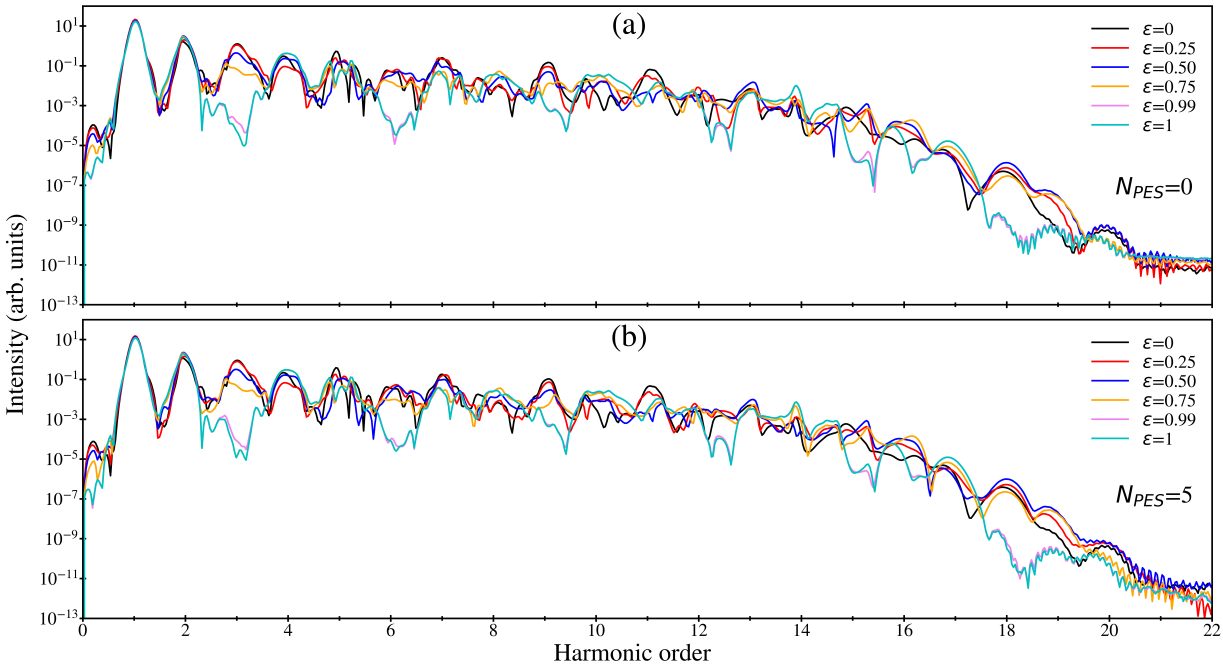


Figure 5.7 Emission spectra of a triangular graphene QD. In each panel, different lines correspond to different ellipticities of the incident pulse. In (a), only the valence band states with negative energies are occupied before the pulse, while in (b), both the valance band states and all edge states are initially populated. The parameter $N_{PES}$ shows the number of populated edge states. The pulse frequency is $\hbar\omega_0 = 1$ eV. The field amplitude of the incident pulse is $F_0 = 0.3$ V/Å. The dephasing time is $\tau = 10$ fs.The intensity is shown on a logarithmic scale.

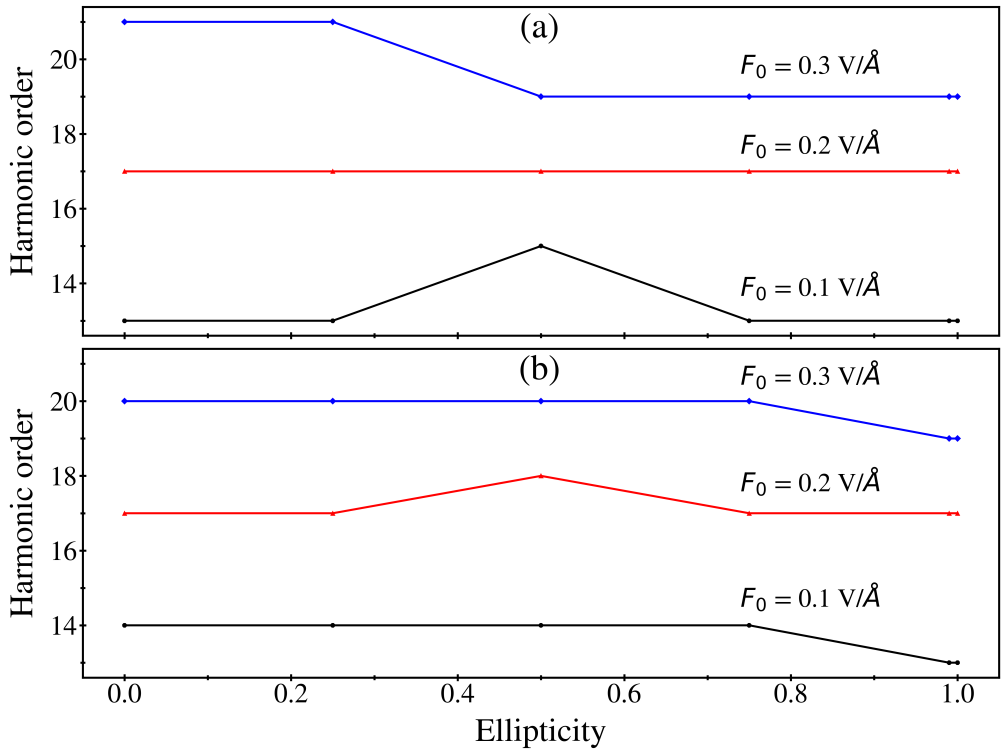


Figure 5.8 Cutoff frequency as a function of the ellipticity of the incident pulse. The results are shown for (a) hexagonal QD and (b) triangular QD. The frequency of the pulse is $\hbar\omega_0 = 1$ eV. The field amplitudes are shown next to the corresponding lines.

5.5(a), 5.5(c) and 5.5(e)], for which the $x$ axis is the axis of symmetry, the optical pulse that is linearly polarized along the $x$ direction generates only the $x$ component of the dipole moment, resulting in high-order harmonics which are linearly polarized with zero ellipticity. For the triangular QD, the $x$ axis is not the axis of symmetry. In this case, a linearly polarized pulse generates both the $x$ and $y$ components of the dipole moment, resulting in the emission of high-order harmonics which are elliptically polarized with small, but finite, ellipticity[see Figs. 5.5(b) , 5.5(d) and 5.5(f)].

Also, the ellipticity of the first-order harmonics, the frequency of which is the same as the frequency of the incident pulse is almost the same as the ellipticity of the incident pulse.

The difference between them is more pronounced for the high field amplitude of 0.3 V/Å[see Figs. 5.5(e) and 5.5(f)]; this difference is related to the nonlinear dynamics of the electron system in the field of the pulse, where the nonlinearity becomes more pronounced for higher field amplitudes.

For high-order harmonics, the unique property of their ellipticities is that they are larger than the ellipticity of the incident pulse. For some cases, the ellipticity of high-order harmonics becomes greater than 1, which means that, while for an incident pulse, the $x$ component of the optical field is greater than the $y$ component, for the high-order harmonics, the $x$ component of the generated field becomes less than the corresponding $y$ component.The enhancement of the ellipticity of high-order harmonics is not related to the system's symmetry, i.e., the behavior is similar for both hexagonal and triangular quantum dots. At the same time, for the hexagonal quantum dot, [see Figs. 5.5(a), (b), (c)], the enhancement of the ellipticity of high-order harmonics is more pronounced than for the triangular quantum dot. Also, the tendency with increasing the amplitude of the incident pulse is that the largest ellipticity is observed at smaller order harmonics when the amplitude of the pulse increases. For example, for the field amplitude of 0.1 V/Å, the maximum ellipticity is realized for the fifth and the seventh harmonics, while for the field amplitude of 0.3 V/Å, the maximum ellipticity is for the third harmonics.

While the hexagonal quantum dot has inversion symmetry, which results in the suppression of even-order harmonics, the triangular quantum dot does not have such symmetry, and odd-order harmonics are generated in the field of an elliptically polarized pulse. The ellip-

ticities of the corresponding harmonics are shown in Fig.5.6. For a linearly polarized pulse along the $x$ direction, i.e., for $\epsilon = 0$, the emitted even-order harmonics are linearly polarized along the $y$ axis, which follows from the reflection symmetry of the triangular quantum dot with respect to the $y$ axis. For our definition of the ellipticity, this polarization results in the infinite ellipticity of the even-order harmonics for $\epsilon = 0$. For the finite ellipticity of the incident pulse, $\epsilon > 0$, the ellipticities of the even-order harmonics are mainly greater than the ellipticity of the incident pulse. Also, for a circularly polarized incident pulse, $\epsilon = 1$, the emitted harmonics are circularly polarized.

For a triangular graphene QD with zigzag edges, there are degenerate edge states with zero energy. Above, we considered the situation in which only the valence band states are initially populated. For such a quantum dot, there is another possibility when both the valence and edge states are populated before the pulse. A comparison of the emission spectra for these two cases is presented in Fig.5.7. The results are identical, which is a manifestation of the particle-hole symmetry for these two systems. Namely, the situation in which only the valence band states are initially populated by electrons is identical to the situation in which only the conduction band states are initially populated by holes, i.e., the valence band and edge states are populated by electrons before the pulse. This symmetry is presented in the tight-binding model of graphene QDs considered above.

One of the important characteristics of the emission spectra is the cutoff frequency, i.e., the maximum frequency that can be generated by the system placed in the field of a pulse. The cutoff frequency as a function of the ellipticity $\epsilon$ of the incident pulse is shown in Fig.5.8.

The cutoff frequency has a weak dependence on $\epsilon$, with some large changes observable near $\epsilon \approx 0.5$. Namely, for the hexagonal QD and the large field amplitude, $F_0 = 0.3$ V/Å, the cutoff frequency decreases when the driver ellipticity increases from $\epsilon = 0.25$ to 0.5 and is constant at larger values of $\epsilon$, $\epsilon > 0.5$. At a smaller field amplitude, $F_0 = 0.1$ V/Å, the cutoff frequency shows nonmonotonic dependence within the interval of $0.25 < \epsilon < 0.75$, with the maximum at $\epsilon = 0.5$. For the triangular QD, the cutoff frequency decreases for $\epsilon > 0.75$, with the smallest value being realized for a driver ellipticity close to 1.

With increasing field amplitude, the cutoff frequency increases; i.e., more harmonics are generated, which is the expected behavior for systems interacting with an optical pulse. Also, for both types of QDs, triangular and hexagonal, the cutoff frequency is almost the same, which suggests that the cutoff frequency has real sensitivity to the geometry of QDs.

The generation of high-order harmonics is a manifestation of nonlinear electron dynamics in graphene QDs placed in the field of an optical pulse. Such electron dynamics can also be characterized by the population of excited QD states, i.e., conduction band and edge states, during the pulse and after the pulse. In Fig. 5.9, the total population of excited QD states is shown as a function of time. While it is an integral characteristic of the electron dynamics, the results are different for a linearly polarized incident pulse and a circularly polarized pulse. For a linearly polarized pulse, shown by blue lines in Fig.5.9, the population of the excited QD states shows an oscillatory behavior during the pulse, while such behavior is strongly suppressed for a circularly polarized pulse, which is illustrated by the red lines. This behavior is consistent with the suppression of the high-order harmonics

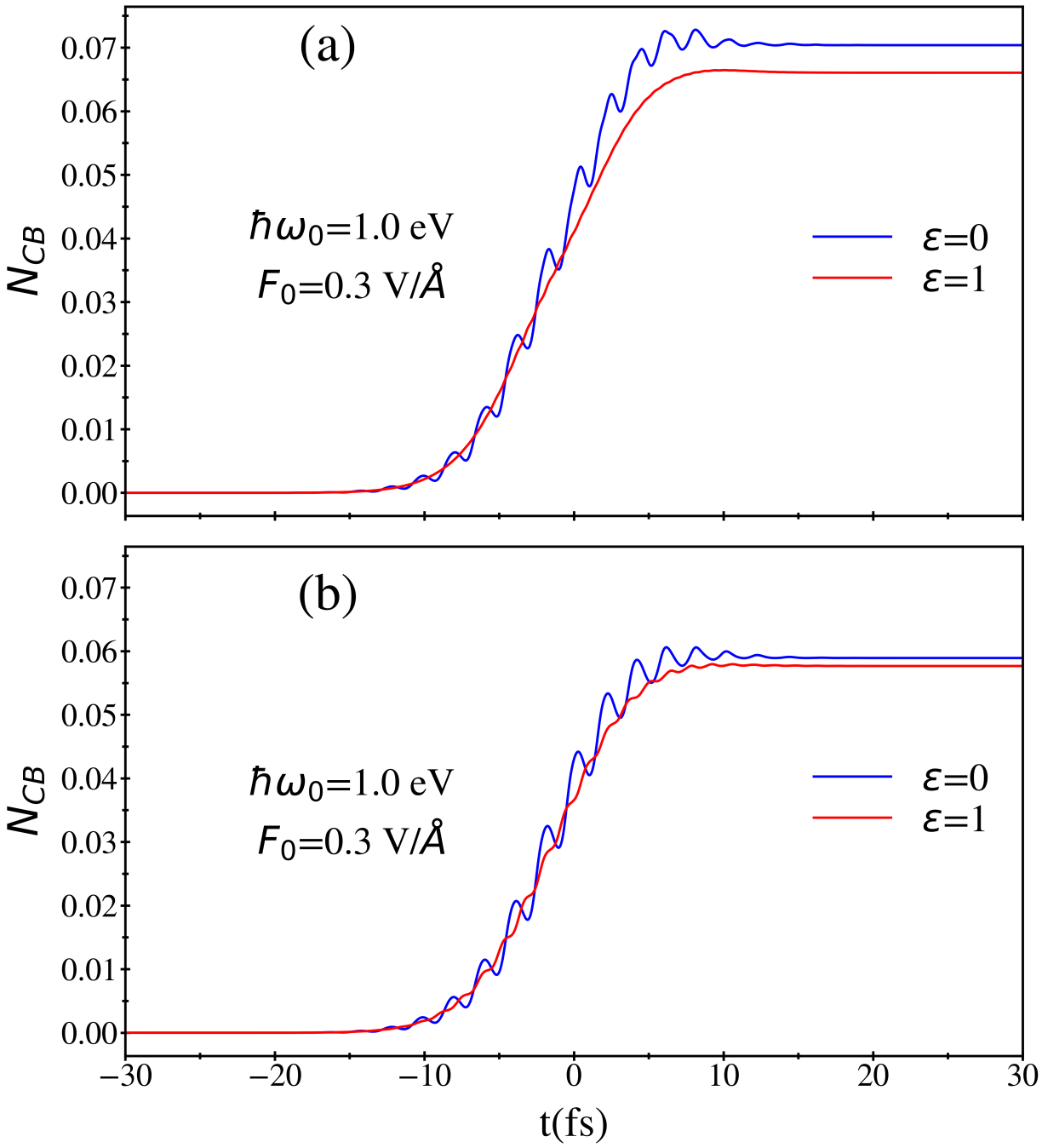


Figure 5.9 Conduction band populations of graphene QDs as a function of time. The results are shown for (a) the hexagonal QD and (b) triangular QD. In each panel, the results are shown for a linearly polarized pulse, $\epsilon = 0$, and a circularly polarized pulse, $\epsilon = 1$, by the blue and red lines, respectively. The frequency of the pulse is $\hbar\omega_0 = 1$ eV, and the field amplitude is 0.3 V/Å.

reported above for a circularly polarized incident pulse. For all cases, the electron dynamics is highly irreversible; i.e., the residual population of the excited states is comparable to the corresponding maximum population during the pulse. Also, in terms of the total population of the excited states, there is no fundamental difference between the triangular and hexagonal quantum dots. For both cases, the results show similar behavior because both systems have comparable band gaps around 1.9 eV.

Another characteristic of the electron dynamics is a residual population of the excited states of a QD after the pulse. Such a population is shown in Fig. 5.10 for both triangular and hexagonal QDs and for two polarizations of the incident pulse: linear and circular ones. While for the total population of the excited states shown in Fig.5.9, there is no difference between the two types of QDs; there is a fundamental difference between the populations of individual levels shown in Fig. 5.10. Namely, for the triangular QD [see Figs. 5.10(b) and 5.10(d)], there is a large population of edge states and a relatively small population of conduction band states, while for the hexagonal QD, the population of conduction band states is relatively large. This behavior is related to the different natures of the band gaps in these two QD systems. For the hexagonal QD, the band gap of 1.91 eV is between the valence band states and the conduction band states, while for the triangular QD, the band gap of 1.87 eV is between the valence band states and the edge states of the system. In terms of the dependence of an incident pulse on polarization, for both types of QDs, the lower energy excited states become more populated for a circularly polarized pulse. Namely, for the triangular QD, the edge states become more populated after a circularly polarized

pulse, while for the hexagonal QD, the excited states near the edge of the conduction band are more populated for a circularly polarized pulse compared to a linearly polarized pulse.

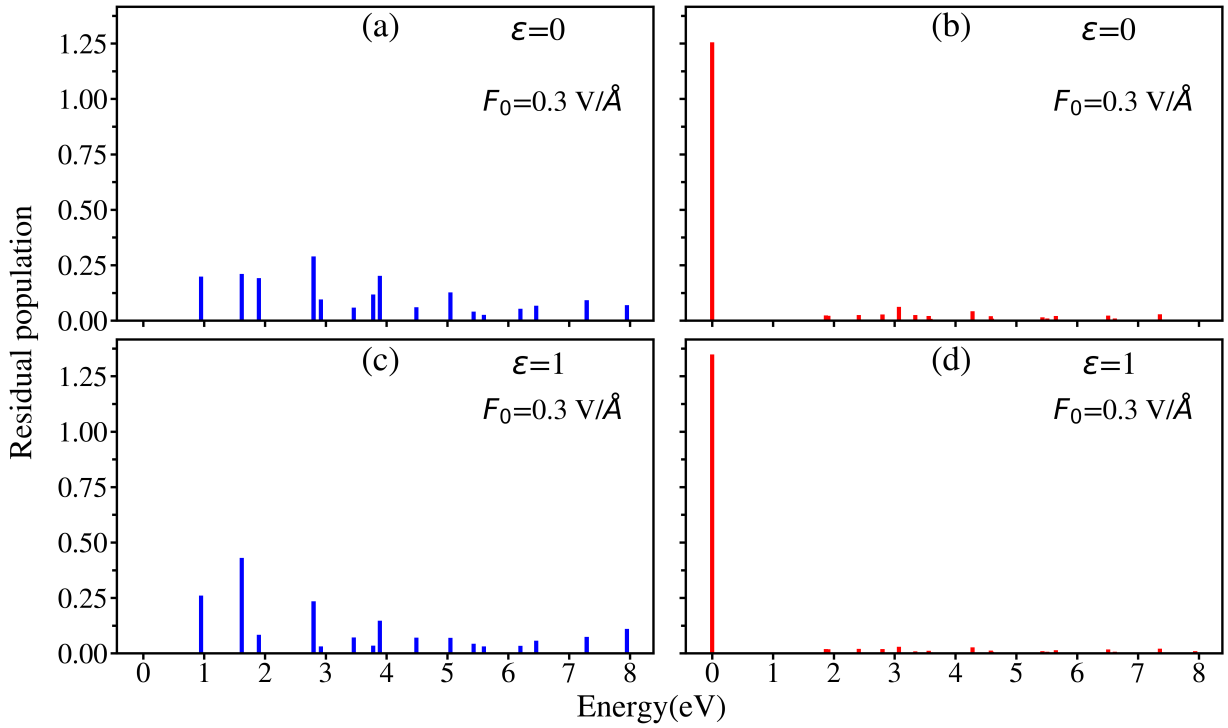


Figure 5.10 Residual populations of individual excited states of graphene QDs. The results are shown (a) and (c) for the hexagonal QD and (b) and (d) for the triangular QD. The polarization of an incident pulse is linear in (a) and (b) and circular in (c) and (d). For the triangular QD, the results at zero energy correspond to the populations of initially unoccupied edge states of the QD. The frequency of the pulse is $\hbar\omega_0 = 1$ eV and the field amplitude is 0.3 V/Å.

## 5.3 Conclusion

The emission spectra of graphene quantum dots in a field of an optical pulse depend not only on its intensity but also on its polarization. Namely, for an elliptically polarized pulse, the ellipticity of the pulse can be used as a tuning parameter to change the generation of high harmonics in QD systems. In the present chapter, we considered two types of

QDs: hexagonal and triangular QDs, which have $D_{6h}$ and $D_{3h}$ symmetries, respectively. The radiation spectra of such QDs show strong sensitivity to the ellipticity of an optical pulse when the optical pulse becomes close to a circularly polarized one. Such sensitivity is observed as a suppression of some high-order harmonics in the radiation spectra. The orders that are suppressed are determined by the symmetry of the QD; for a triangular QD, every third harmonic is suppressed, while for a hexagonal QD, every sixth harmonic is suppressed. While for small field amplitudes, the suppression of the corresponding harmonics is realized mainly for a circularly polarized pulse, for large field amplitude, the suppression occurs also for an elliptically polarized pulse with ellipticities that are in some range close to a circularly polarized pulse. Also, for a hexagonal QD, which has inversion symmetry, all even-order harmonics are suppressed for all ellipticities of the optical pulse, not only for a circularly polarized pulse.

Interaction of an elliptically polarized pulse with graphene QDs also generates elliptically polarized radiation. The ellipticities of the corresponding high-order harmonics depend on the parameters of the incident pulse, and in some cases, for large enough orders of harmonics or large intensity of the incident pulse, the corresponding polarization ellipse of high-order harmonics is effectively rotated by $90^0$ compared to the polarization ellipse of the incident pulse.

We studied the ultrafast electron dynamics of graphene QDs under an elliptically polarized pulse. The harmonic intensities depend on the amplitude of the optical pulse, its ellipticity, and the symmetry of the QD. The symmetry of the QD system plays a vital role

in the occurrence of even- or odd-order harmonics. Here, we observed only odd harmonics for the hexagonal dots, which possess $D_{6h}$ symmetry, while for triangular dots with $D_{3h}$ symmetry, both the even- and odd-order harmonics were observed. More importantly, the suppression of the harmonics was observed for both hexagonal and triangular dots. Such suppression of the high-order harmonics by varying the ellipticity of the incident pulse could provide an excellent way to control the HHG in graphene QDs and other 2D systems. The harmonic conversion efficiency for graphene QDs is of the order of $10^{14}$ per quantum dot. To enhance the conversion efficiency, an array of the corresponding quantum dots should be considered.

Thus, for graphene quantum dots interacting with an elliptically polarized optical pulse, both the intensity and the polarization of the generated high-order harmonics can be controlled by tuning the ellipticity of an incident pulse.

# CHAPTER 6

# CHAPTER 6 IMPACT OF MONOVACANCY OR DIVACANCY IN GENERATED HARMONICS IN GRAPHENE QUANTUM DOTS

## 6.1 Introduction

Exploring 2D materials, such as graphene, transition metal dichalcogenides, and their derivatives, has recently opened up a captivating and dynamic research frontier [1; 124; 125; 126; 127; 128; 129; 130; 131; 132; 133; 134]. This realm, encompassing monolayers, bilayers, nanostructures, and quantum dots (GQDs), presents a unique opportunity to transcend the limitations of graphene's zero band gap. [135; 136; 137; 138]. Investigating optoelectronic properties in finite structures like graphene quantum dots has sparked significant interest, particularly in the potential for bandgap tunability based on shape, size, geometry, and edge type [139; 140]. Currently, researchers are delving into the generation of high-order harmonics, a product of optical activity, to gain profound insights into the electron dynamics of nanostructured systems when interacting with ultrafast optical pulse fields [26; 141; 85; 88; 104].

High harmonic generation (HHG) is a highly nonlinear optical process that creates very short wavelengths- extreme ultraviolet (EUV)- through soft x-rays via ultrafast solid lasers [18; 84; 50; 27]. The HHG process is coherent and uses a very intense ultrafast laser pulse in gas and solids [142; 143]. In gas, such an energetic optical field overcomes the field that binds the electron to an atom, knocking electrons and accelerating them, and then returning, releasing all of the kinetic energy gained in photons [96]. This rapid electron acceleration on

attosecond timescales produces a coherent beam of radiation. In solids, the HHG process can typically be explained in three steps: tunnel ionization, where an electron tunnels through the potential barrier of an atom or molecule; acceleration, where the electric field of the laser accelerates the electron; and recombination, where the electron recombines with the parent atom, releasing energy in the form of a high-energy photon [16].

Due to the growth process, defects in natural solids are inevitable [144]. These defects can take any form, such as vacancies, impurities, dislocations, disorders, etc. [145; 146; 147; 148]. The engineering of a proper defect mechanism provides researchers with opportunities to impact electronic and optical properties, including electronics development with doping and creating a nitrogen-vacancy defect in diamonds or a single photon emitter in two-dimensional materials[149; 150; 151; 152]. Under light-matter interaction, imperfections such as vacancies or doping in nanostructures could significantly alter the high harmonic emission spectra, opening up a new avenue for research [153; 154; 97; 155]. In ref.[154], HHG in GQDs with disorder or vacancy is reported. Still, more study is needed to understand how these defects, or 'imperfections, 'can assist in the high harmonic generation process. Such studies could revolutionize our understanding of HHG and offer a fresh perspective on the optoelectronics of 2D materials, including quantum dots and nanostructures.

In the present work, we attempt to understand how the nonlinear effect, such as HHG, changes GQDs with imperfections, notably by introducing the absence of single or double atoms defined by monovacancy or divacancy. These vacancies, or 'holes' in the atomic structure, are significant as they can dramatically alter the electronic and optical properties of

the GQDs. We found that even monovacancy changes the spectrum remarkably enough to break the symmetry of the GQDs and modify the spectra significantly. This is a significant finding, as the symmetry of GQDs plays a crucial role in their optoelectronic properties. We also investigate how the intensity of HHG changes with varying sizes, shapes, geometry, and types of edges of GQDs, accounting for these vacancies. We observed that these vacancies are more sensitive to small-sized GQDs than bigger ones, where the effect is less pronounced as a more significant size. These vacancies are sensitive to the geometry of the dots; for example, the GQDs with hexagonal geometry having $D_{6h}$ geometry, a specific geometric configuration with six-fold rotational symmetry and a mirror plane, under these vacancies experience significant uplifting of energy levels, creating zero energy edge states with monovacancy responsible for the emergence of even order harmonics. Such uplift is also valid for divacancy, which changes the high harmonics spectrum, boosting harmonics in small-sized hexagonal dots. In zigzag-edged triangular dots with $D_{6h}$ geometry, monovacancy causes either a decrease in the number of zero energy edge states by significantly reducing the effective bandgap or an increase in the number of edge states, keeping the effective bandgap the same as in intrinsic GQD system but changing the high harmonics spectra. In armchair-edged triangular dots, monovacancy introduces zero energy edge states as in hexagonal dots and changes the emission spectra. However, even harmonics under vacancies get suppressed significantly with divacancy. These results are sensitive to the polarization of incident pulse, providing significant changes in spectra between linear and circularly polarised incident optical pulse. One of the most noticeable changes is monovacancy or divacancy, which disrupts

the symmetry-related suppression of harmonics observed in triangular and hexagonal GQDS.

The paper is structured as follows: Section II presents the model and main equations based on the density matrix approach, a mathematical tool widely used in quantum mechanics to describe a system's quantum state. The density matrix approach, a powerful method in quantum mechanics, allows for a more general description of a system's state, such as a GQD, than the wave function. It provides a more comprehensive description of the system's quantum state, including information about its coherence and mixed states. These equations describe the emitted radiation from GQD systems. Section III discusses the key findings, further summarized in the concluding Section IV.

### 6.2 Results and Discussion

The $N$ atoms intrinsic neutral graphene quantum dots (GQDs) system forms an $N$ by $N$ square matrix Hamiltonian that provides $N$ eigenvalues and $N$ times $N$ eigenvectors employing a tight-binding approach. If we introduce vacancies such as monovacancy, the number of atoms decreases by one and becomes $N-1$, providing $N-1$ eigenvalues on solving. In the case of divacancy, we obtain $N-2$ eigenvalues corresponding to $N-2$ neutral atoms. The zigzag-edged hexagonal GQDs (Fig. 6.1), zigzag-edged triangular GQDs (Fig. 6.2), and armchair-edged triangular GQDs (Fig. 6.3) represent the energy profiles for the corresponding neutral GQDs systems shown within inset in each panel. The number of atoms in the GQDs system and the number of vacancies introduced are also illustrated in the figures. In each case, monovacancy, or divacancy, lifts the energy levels compared to intrinsic

parent GQDs, providing additional channels to enhance the high harmonic emission spectra in most cases. These systems are further illustrated in Table 6.1, including bandgap, which is tunable in terms of shape, size, type of edge, and geometry in the case of the GQDs.

Table 6.1: Depiction of the number of dots, vacancies, bandgap, geometry, and edge type in GQD systems.

| Number of dots in GQD systems ($N$) | Number of Vacancies ($N_{vac}$) | Bandgap (eV) | GQD geometry | Edge type |
|---|---|---|---|---|
| 24 | 0 | 3.0 | Hexagonal | Zigzag |
| | 1 | 1.5 | | |
| | 2 | 1.3 | | |
| 54 | 0 | 1.9 | Hexagonal | Zigzag |
| | 1 | 0.95 | | |
| | 2 | 1.9 | | |
| 84 | 0 | 1.76 | Hexagonal | Zigzag |
| | 1 | 0.88 | | |
| | 2 | 0.9 | | |
| 22 | 0 | 2.41 | Triangular | Zigzag |
| | 1 | 0.88 | | |
| | 2 | 1.58 | | |
| 33 | 0 | 2.3 | Triangular | Zigzag |
| | 1 | 2.3 | | |
| | 2 | 1.65 | | |
| 61 | 0 | 1.87 | Triangular | Zigzag |
| | 1 | 1.37 | | |
| | 2 | 0.79 | | |
| 36 | 0 | 2.88 | Triangular | Armchair |
| | 1 | 1.44 | | |
| | 2 | 1.1 | | |
| 60 | 0 | 2.32 | Triangular | Armchair |
| | 1 | 1.16 | | |
| | 2 | 2.16 | | |

The intrinsic or perfect GQDs (without vacancies) exhibit harmonics respecting the system's symmetry. For example, hexagonal GQDs with $D_{6h}$ symmetry only produce odd

harmonics, while triangular GQDs have $D_{3h}$ symmetry that shows both even and odd harmonics. These results correspond well with the earlier findings in [26; 85]. We further analyze harmonics' polarization, setting the ellipticities between two extremes, linear pulse and circular pulse. With incident circularly polarized pulse, symmetry-related suppressions are well established for hexagonal GQDs, where suppression is observed for every sixth harmonic ( clear from Fig. 6.4). In contrast, every third harmonic in triangular GQDs ( refer Fig. 6.5) strongly suppresses in response to a circularly polarized pulse. These results correspond well to the recent finding [88].

We also investigate how the robustness of the even harmonics depends on the type of edges of the triangular GQDs. In intrinsic triangular GQDs of comparable sizes, zigzag edges show strong, even harmonics compared to armchair edges. In armchair edge GQDs, y-polarized intensity-intensity corresponding to the y component of dipole moment, which predominantly contributes to even harmonics, is weak compared to x-polarized, which predominately contributes to the odd harmonics. As a result, very weak, even harmonic peaks are emitted from armchair edges, as seen in Fig. 6.6. In zigzag edges even, order harmonic peaks are comparable to odd-order harmonics in the absence of vacancies.

The study aims to understand how high harmonic spectra change with vacancies. We consider the GQDs with monovacancy missing one atom and divacancy missing two atoms. Such vacancies in the natural crystal may result from experimentally preparing procedures, including crystal growth and fabrication, or from the crystal itself innate, whose optical properties are worthy of exploration. The linearly polarized incident pulse incident on GQDs with

monovacancy enhances the harmonic spectra significantly for small GQDs. The degree of enhancement gradually becomes weaker for intermediate-sized GQDs and sets the lowest degree of enhancement for larger GQDs. In all cases, just missing a single atom symmetry-related harmonics are mostly affected. In HGQDs, monovacancy lifts the energy levels, causing the rise of zero energy edge states and giving birth to the even-order harmonic induced by the inversion symmetry breaking. These even harmonics arising from the symmetry breaking are significantly higher than the odd-order harmonics, specifically in small GQDs. However, the even harmonics are not comparable to odd harmonics when the dots become larger. Nevertheless, even harmonics are significant and noticeable in GQDs resulting from symmetry breaking due to monovacancy. Similar results are noted for zigzag-edged triangular GQDs where monovacancy either reduces or decreases the number of zero energy edge states, lifting the energy levels significantly. Except for 33-atom zigzag-edged TGQDs, in all cases, the number of zero energy edge states is decreased by 1, resulting in monovacancy. In the case of 33-atom TGQDs, monovacancy adds zero energy edge states, making four from three edge states initially present. In this specific case, no bandgap is changed. In armchair-edged triangular GQDs, monovacancy results in the rise of zero energy, causing a significant boost of even harmonics, as observed in zigzag-edged hexagonal GQDs. In all cases of monovacancy, the bandgap is significantly reduced. Such bandgap change resulting from vacancies is presented in Table. 6.1.

For circularly polarized pulses, monovacancy disrupts all the symmetry-related suppression observed for intrinsic GQDs. Monovacancy boosts the suppressed harmonic spectra in

every third of the high harmonic spectrum in triangular GQDs. This result is applicable for both types of edges, zigzag or armchairs, in triangular GQDs. Such a boost-up of the harmonics in hexagonal GQDs is observed for every sixth harmonic instead of the suppression that is achieved for intrinsic GQDs.

Divacancy significantly enhances the high harmonic spectra as compared to intrinsic GQDs. Nonetheless, the degree of enhancement is lower than that of monovacancy, specifically in small zigzag-edged hexagonal GQDs. The 54- and 84-atom GQD systems with intermediate to big sizes exhibit significant enhancement for eight harmonics. The most substantial intensity peak enhancement in small triangular GQDs is observable. However, it gradually weakens as the system grows, increasing the number of dots in both zigzag and armchair edges. In response to polarization, divacancy undergoes significant changes. The disruption of symmetry-related harmonics results in the suppression of both hexagonal and triangular geometry GQDs systems. The observed boost of these harmonics is depicted in Fig. 6.4 - Fig. 6.6.

We further investigate how increasing the field strength of the optical pulse changes the high harmonics in hexagonal and triangular GQDs. We further investigate the effect of monovacancy or divacancy in triangular and hexagonal GQD systems under linearly and circularly polarized incident optical fields. The system responds uniquely to monovacancy or divacancy and linear and circular polarization of the incident optical pulse. Such variations can easily be understood from Fig. 6.7 and Fig. 6.8.

Under linear polarization, specifically for small GQDs, the effect of monovacancy or di-

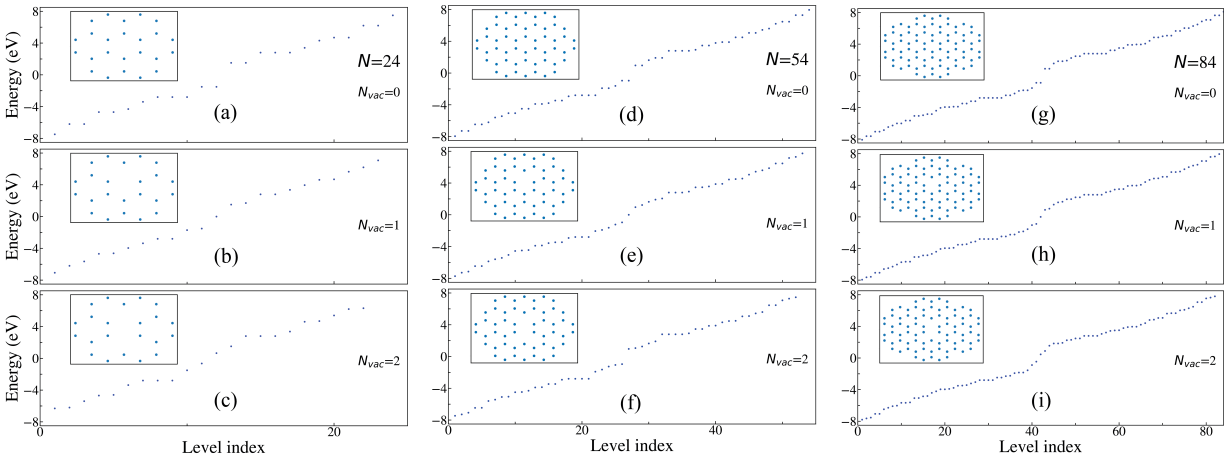


Figure 6.1 Energy profile for hexagonal GQDs system having the zigzag edge. Perfect GQDs (no vacancies) (a), (d), and (g); monovacancy (b), (e), and (h); divacancy (c), (f), and (i). The number of atoms in each GQD system is displayed in left (24), center (54), and right (84) panels. The inset in each panel represents the GQDs system.

vacancy becomes stronger depending upon the system and geometry. For triangular GQD of 22 atoms, divacancy becomes strongest except in second harmonics, in which monovacancy is exceptionally strong at a small field strength of $F_0$= 0.1 V/Åand though dominant but relatively weaker at higher amplitudes 0.3 and 0.5 V/Å. In this system, harmonics with monovacancy are between harmonics with divacancy and harmonics without vacancy regarding the height of the harmonic peaks. On the other hand, in small hexagonal GQDs of 24 atoms, the harmonic peaks of monovacancy dominate all the time. However, the number of harmonic orders increases with pulse amplitude. In this case, the effect divacancy is intermediate, setting shorter harmonic peaks for intrinsic GQD and longer for monovacancy, as stated earlier. Such unique differences in hexagonal and triangular GQDs in response to monovacancy or divacancy are expected due to the difference in symmetry of the system,

location of vacancy, number of vacancies, nontrivial nature of the vacancies and presence or absence of zero energy edge states.

Fig. 6.8 represents the emission spectrum of the triangular and hexagonal systems under circularly polarized ultrafast pulse. In all cases, the effect of monovacancy dominates with few exceptions at the low pulse amplitude. The unusual behavior is that the divacancy slightly boosts the first harmonics compared to monovacancy in both GQDs. However, the peaks of first harmonics corresponding to divacancy and monocracy are comparable at larger field amplitudes at hexagonal GQDs. In contrast, for triangular GQDs, the first peak corresponding still dominates, but the effect is weaker than a small field. In all cases, another notable change is the symmetry-related suppression of harmonic peaks shown by black curves, which are disrupted by either monovacancy or divacancy in both GQDs shown

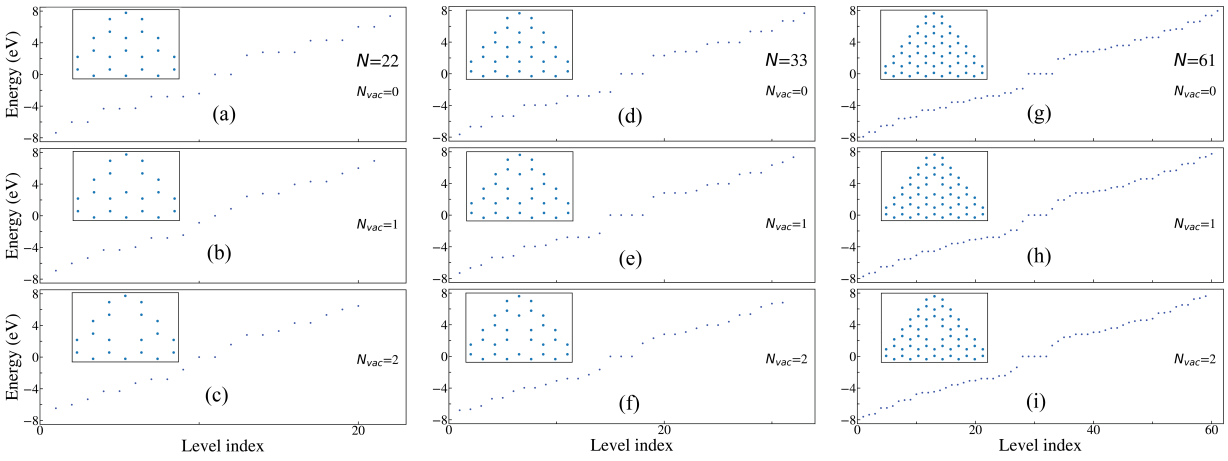


Figure 6.2 Energy profile for triangular GQDs system having the zigzag edge.Perfect GQDs (no vacancies) (a), (d), and (g); monovacancy (b), (e), and (h); divacancy (c), (f), and (i). The number of atoms in each GQD system is displayed in left (22), center (33), and right (61) panels. The inset in each panel represents the GQDs system.

by blue and red curves. We also observed a gradual increase of intensity in both types of GQD with an increase in field amplitude, as expected.

We further investigate the emission spectra of the triangular GQDs with the types of edge. In the intrinsic dots with triangular geometry, the zigzag-edged GQDs show well-defined even harmonic peaks comparable to odd harmonics. In the armchair type, the contribution of even harmonics is weaker, and they are low in amplitude compared to odd ones. These variations are clearly illustrated in Fig. 6.9 for 33- and 36-atom GQDs. The left and right panels are designated for corresponding intensity for linear and circular polarization of the light

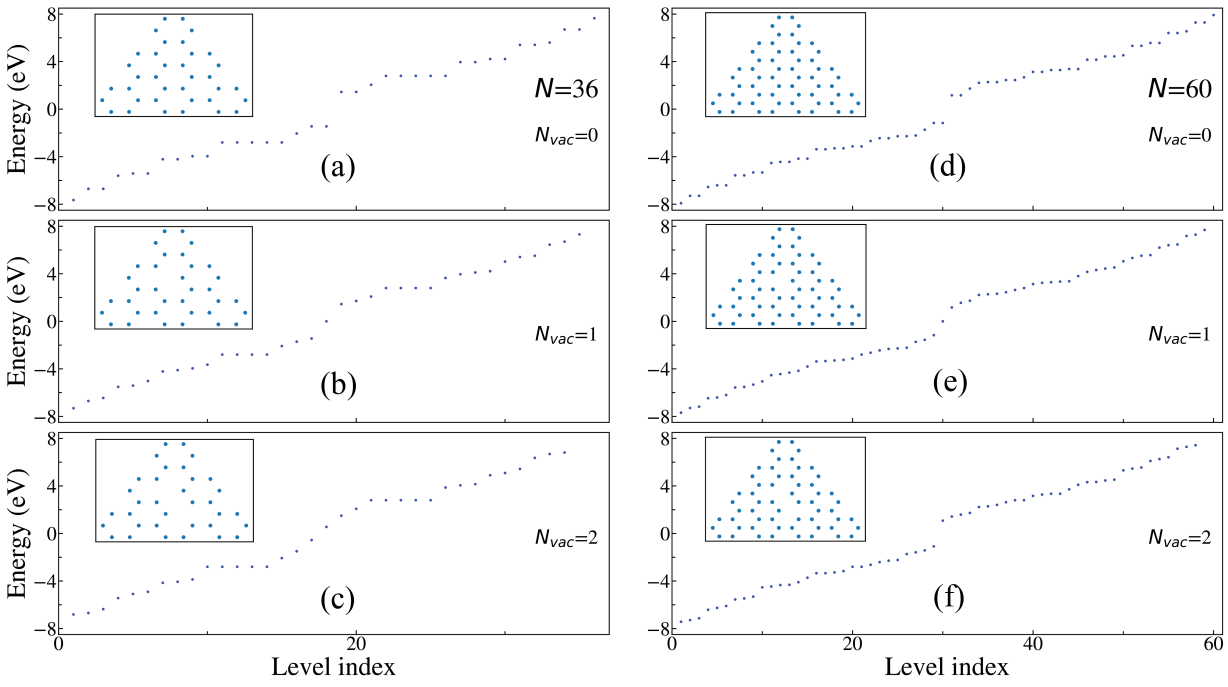


Figure 6.3 Energy profile for triangular GQDs system having the armchair edge. Perfect GQDs (no vacancies) (a), and (d); monovacancy (b), and (e); divacancy (c), and (f). The number of atoms in each GQD system is displayed in panels on the left (36) and right (60). The inset in each panel represents the GQDs system.

panel, illustrating how the emission spectra vary with monovacancy and divacancy compared to intrinsic ones. We observed that monovacancy or vacancy significantly boosts the even harmonics under linear polarization in armchair edge, setting the highest peaks for ever-order harmonics under monovacancy and odd-order harmonics order under 13 with divacancy. A zigzag edge having 33- atoms has more dominance of divacancy for odd order harmonics until 12 and even order dominance until eight order harmonics; then monovacancy boosts up for the remaining spectrum. Under circular polarization, intrinsic GQDs establish the disruption of symmetry-related harmonics in both edge types. However, divacancy dominates

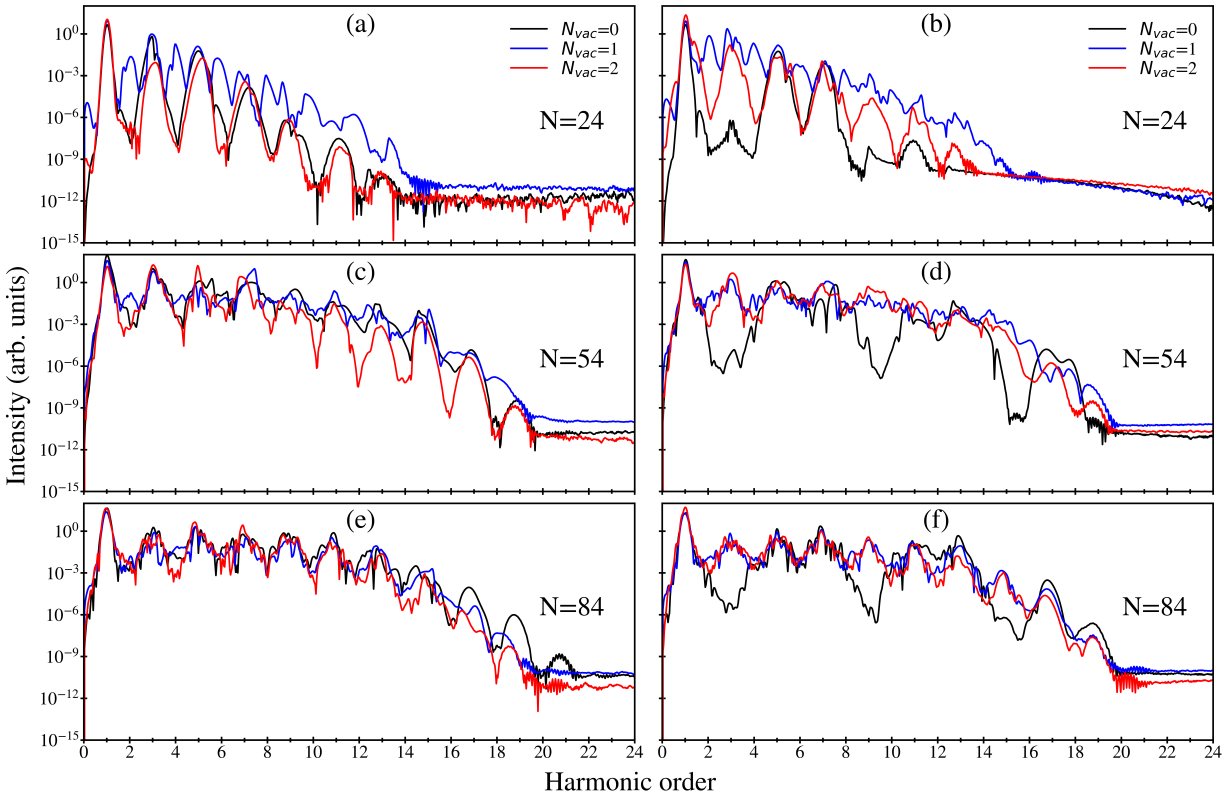


Figure 6.4 HHG spectra for zigzag- edged hexagonal GQDs system: (a), and (b) 24-atom; (c) and (d) 54-atom; and (e) and (f) 84-atom. The number of atoms in each GQD system is also displayed in each panel. The amplitude of the incident pulse is 0.3 V/Å.

for almost the entire spectrum under vacancies in 33-atom GQDs, while odd-order harmonics with divacancy and even-order harmonics with monovacancy dominate in 36-atom TGQD under circular polarization. In triangular geometry, monovacancy or divacancy significantly boosts the harmonic peaks.

When the system grows in size, the effect of monovacancy gradually weakens, as removing a single vacancy does not affect the system as much. However, the disruption of symmetry-related suppression is notable in the case of circularly polarized light, which is demonstrated in Fig. 6.10. In triangular geometry in either edge type, either monovacancy or vacancy

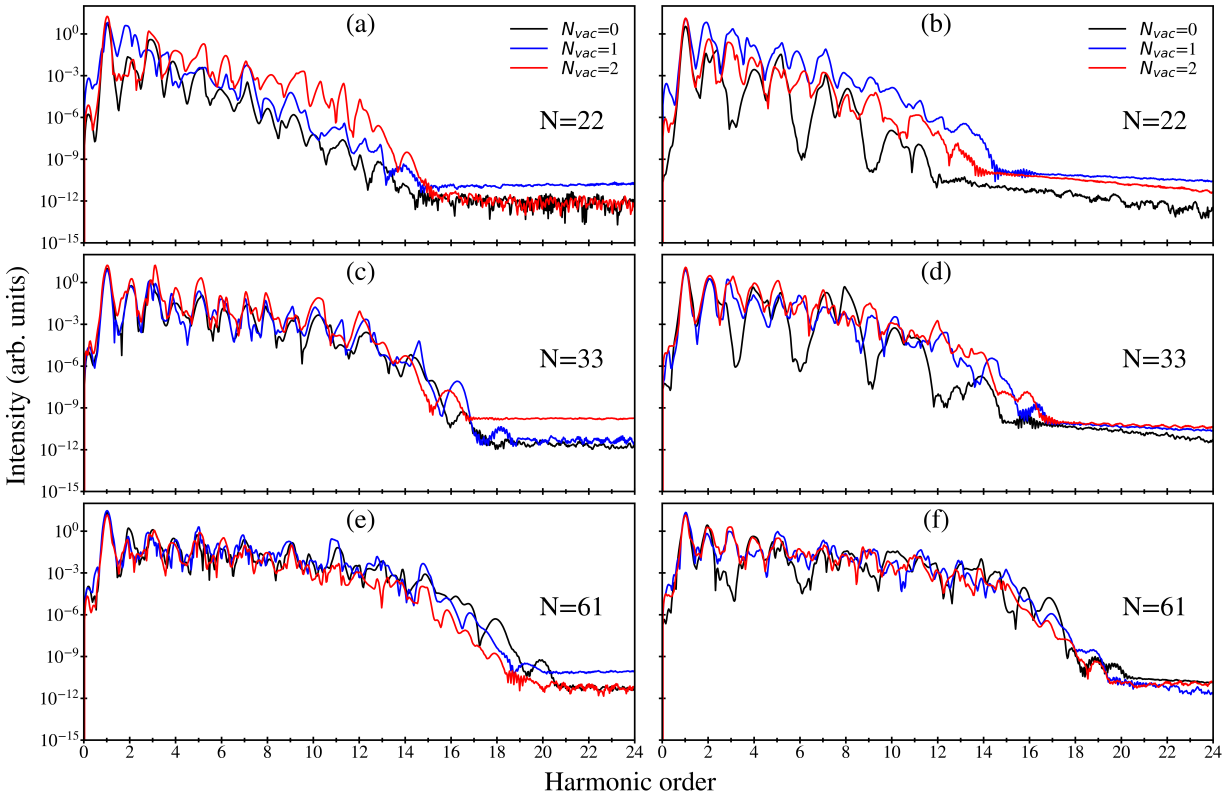


Figure 6.5 HHG spectra for zigzag-edged hexagonal GQDs system: (a), and (b) 22-atom; (c) and (d) 33-atom; and (e) and (f) 61-atom. The number of atoms in each GQD system is also displayed in each panel. The amplitude of the incident pulse is 0.3 V/Å.

significantly boosts the even-order harmonics. In the 61-atom zigzag GQDs, intensity corresponding to divacancy is more vital for low order harmonics until 5, then corresponding peaks with monovacancy are more substantial until 15. Then, around the end of the spectrum, the effect of either monovacancy or divacancy becomes weaker; instead, the intrinsic GQD is more robust in this range. While in an armchair edge-type, all even harmonics with vacancy are boosted, setting the highest values for the monovacancies even with the uniform pattern around the end of the spectrum in a linearly polarized pulse. However, there is no smooth variation; instead,. There is fluctuation due to nonmonotonic bootup observed for linear or circularly polarized light.

We further investigate the intensity corresponding to the $x$ and $y$ components to dipole moment for the GQDs with triangular geometry, including the cases for linear and circular

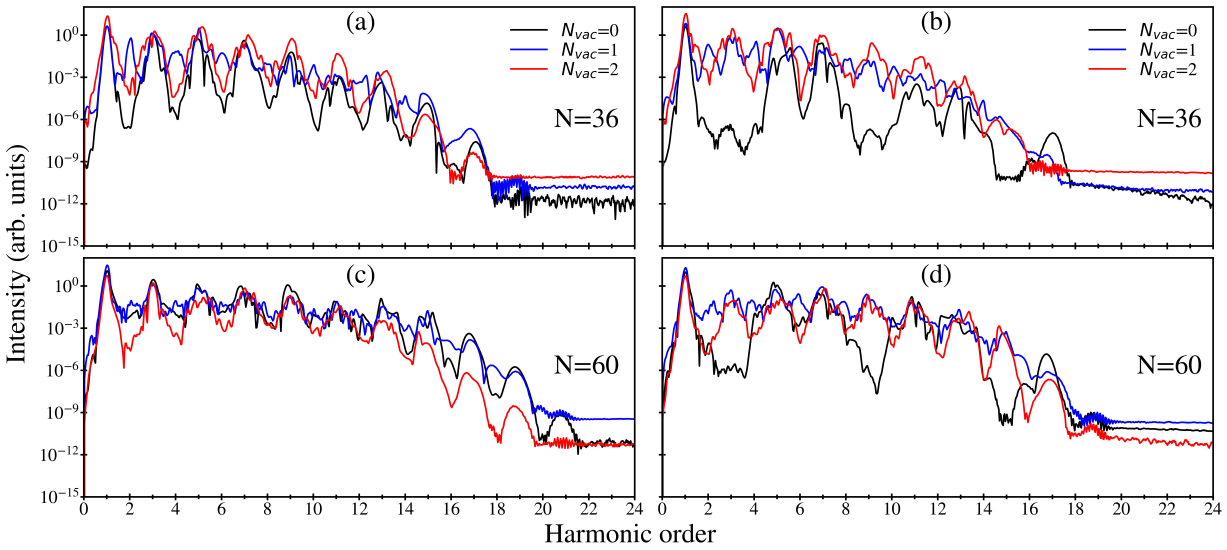


Figure 6.6 HHG spectra for armchair-edged hexagonal GQDs system: (a) and (b) 36-atom; and (c) and (d) 60-atom.The incident optical pulse is linearly polarized (left panel) and circularly polarized (right panel). The number of atoms in each GQD system is also displayed in each panel. The amplitude of the incident pulse is 0.3 V/Å.

polarization of light. For the linear polarization, the changes are more prominent and change slightly with the increase in size. The findings for linear polarization are presented in Fig. 6.11 - Fig. 6.12. For circular polarization, we designate the appendix section presenting them in Fig. 6.13 - Fig. 6.14.

We present the comparative analysis of harmonic spectra under incident linear polarization, analyzing the intensity contribution corresponding to rectangular components of dipole moments $x$ corresponding to 33-atom zigzag and 36-atom armchair-edged triangular

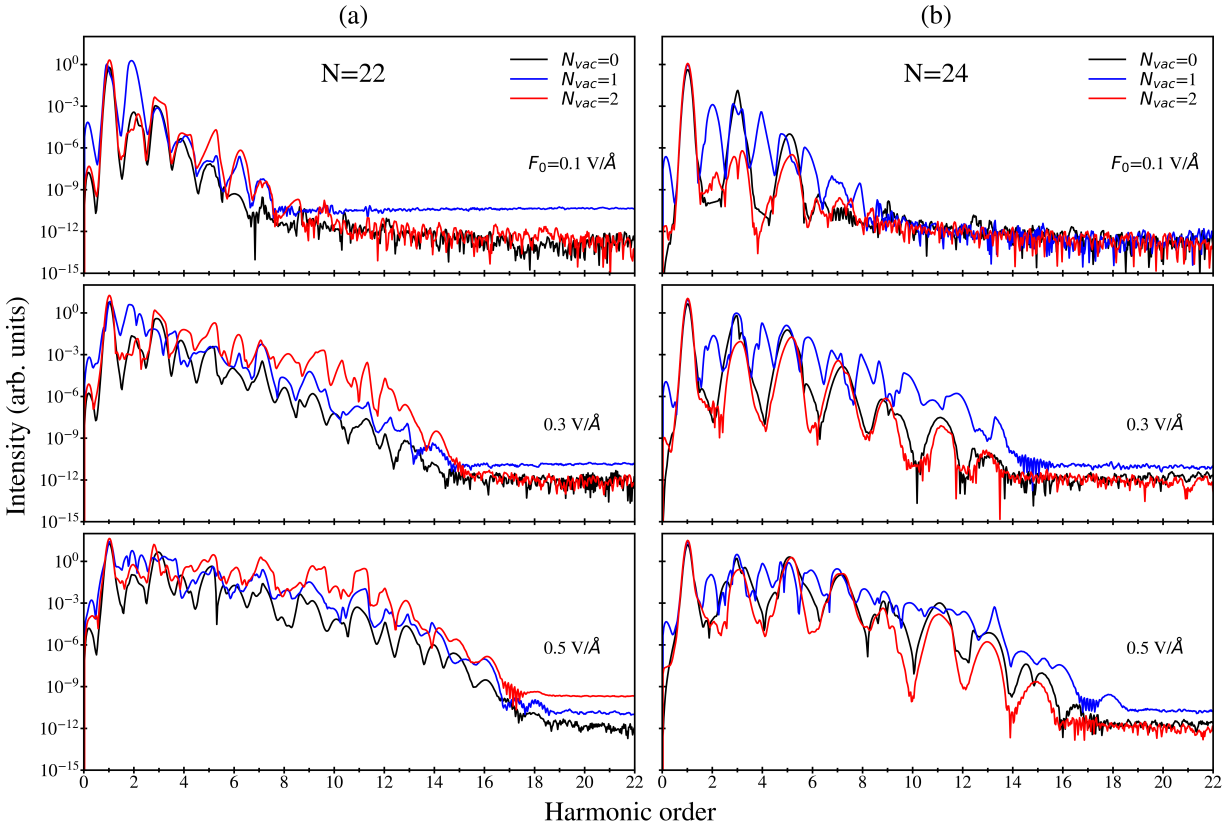


Figure 6.7 Emission spectra comparison: (a) zigzag-edged 22-atom triangular GQDs; and (b) zigzag-edged 24-atom GQDs. The pulse magnitude of an incident optical pulse and the number of vacancies in the GQDs system are also depicted. The incident optical pulse is linearly polarized.

GQDs in Fig. 6.11. Intrinsic GQDs of zigzag edge show a rich spectrum of well-defined high harmonics, including odd and even harmonics of comparable magnitude, primarily odd harmonics contributed by the $x$ component and even harmonics by the $y$ component shown in the top-left panel. The armchair edge shows well-defined odd harmonics mainly contributed by the $x$ component, and tiny even harmonics are contributed majorly by the $y$ component. as displayed in the top-right panel. In this case, weaker harmonics may even result from the absence of in-gap edge states in the armchair edge despite the triangular geometry of

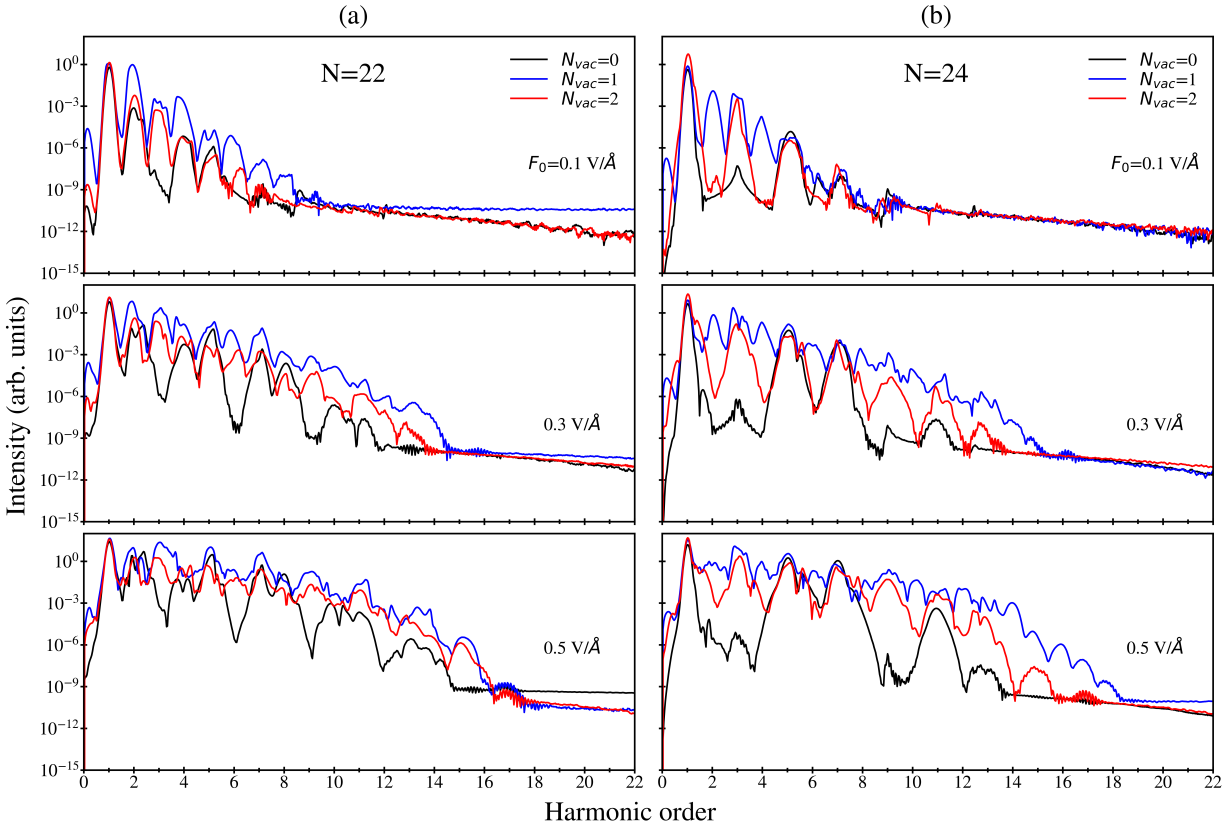


Figure 6.8 Emission spectra comparison: (a) zigzag-edged 22-atom triangular GQDs; and (b) zigzag-edged 24-atom hexagonal GQDs. The pulse magnitude of an incident optical pulse and the number of vacancies in the GQDs system are also depicted. The incident optical pulse is circularly polarized.

the GQDs. Under monovacancy or divacancy, the zigzag-edged GQDs significantly boost the even harmonics near the cutoff region. In contrast, a few lower order even harmonics peaks are slightly decreased with increasing vacancy (clear from left panel central and bottom panel). In this case, monovacancy increases a high harmonic cutoff order from 16 to 18. The armchair edge under vacancy does not show any boost up for even harmonics, almost vanishing even harmonics for divacancy. In these cases, the strength of odd-order harmonics closer to the cutoff decreases significantly with monovacancy and is of comparable intensity with divacancy. This variation among zigzag and armchair edges in triangular edges may result from the presence or absence of edge states, location of monovacancy or divacancy, and extra oblique symmetry in the armchair-edged triangular GQD.

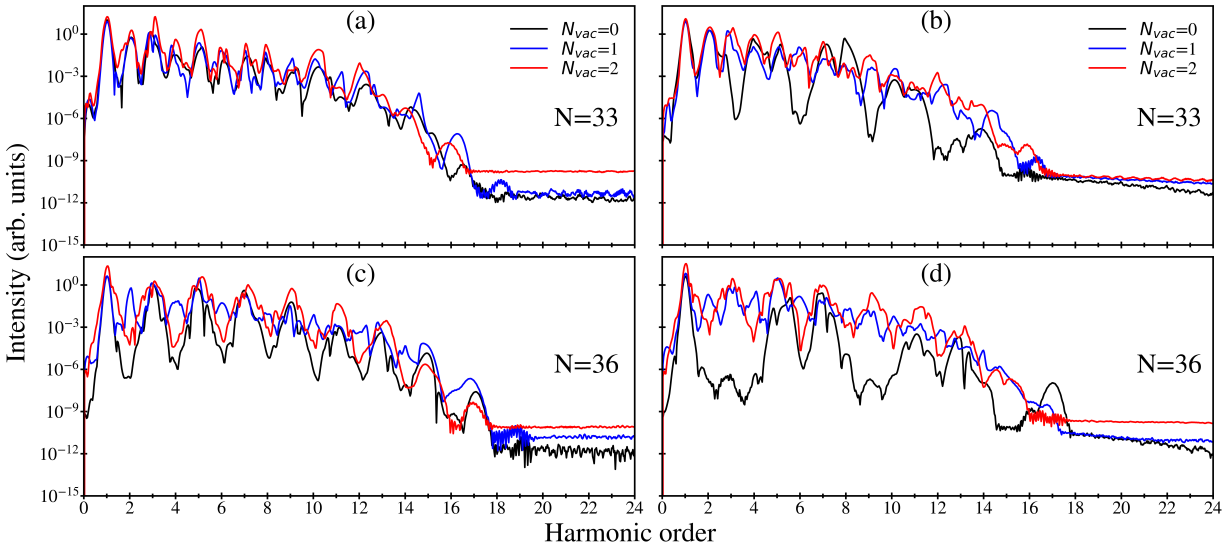


Figure 6.9 Emission spectra comparison for triangular GQDs system: (a), and (b) zigzag-edged 33-atom, and (c) and (d) armchair-edged 36-atom. The left panel is linearly polarized incident optical pulse(a) and (c), and the Right panel is circularly polarized incident optical pulse (b) and (d). The number of atoms in each GQD system is also displayed in each panel. The amplitude of the incident pulse is 0.3 V/Å.

We also analyzed the intensity distribution corresponding to the $x$ and $y$ components of the dipole moment in bigger triangular dots: 61-atom zigzag-edged and 60-atom armchair-edged GQD. In this case, zigzag-edged intrinsic triangular GQD shows a significant signal with comparable odd and even harmonics resulting from $x$ and $y$ components as observed in small-sized zigzagged edges. The intrinsic armchair edge GQD contributes dominant odd harmonics corresponding to the $x$ component. In contrast, the $y$ component provides almost diminished harmonics, even weaker than the small-sized armchair edge discussed before. Regarding monovacancy or divacancy, even harmonic peaks get smaller than odd harmonics. This variation is slightly different than the small zigzag-edged triangular GQDs addressed earlier. The armchair-edged GQD, on the other hand, shows a weaker even harmonic signal

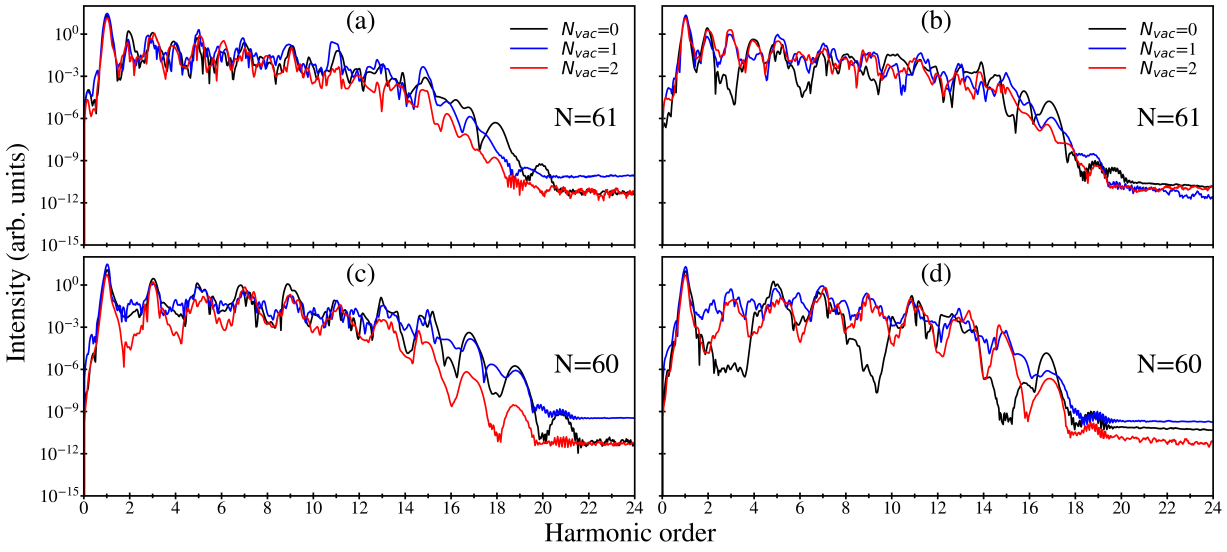


Figure 6.10 Emission spectra comparison for triangular GQDs system: (a), and (b) zigzag-edged 61-atom, and (c) and (d) armchair-edged 60-atom. The left panel is linearly polarized incident optical pulse(a) and (c), and the Right panel is circularly polarized incident optical pulse (b) and (d). The number of atoms in each GQD system is also displayed in each panel. The amplitude of the incident is 0.3 V/Å.

for monovacancy and almost vanishing even harmonics for divacancy as observed in small-sized armchair edged discussed earlier. The odd harmonic signal is dominant in this case, as agreed earlier. This variation may be due to the negligible effect of vacancies in a bigger size, type of edge, and location of the particular vacancy.

This section explores how the intensity corresponding to the dipole moment component in zigzag and armchair edges triangular GQDs changes with a circularly polarized incident pulse. We present the finding for small-sized dots in Fig. 6.13 and relatively bigger-sized

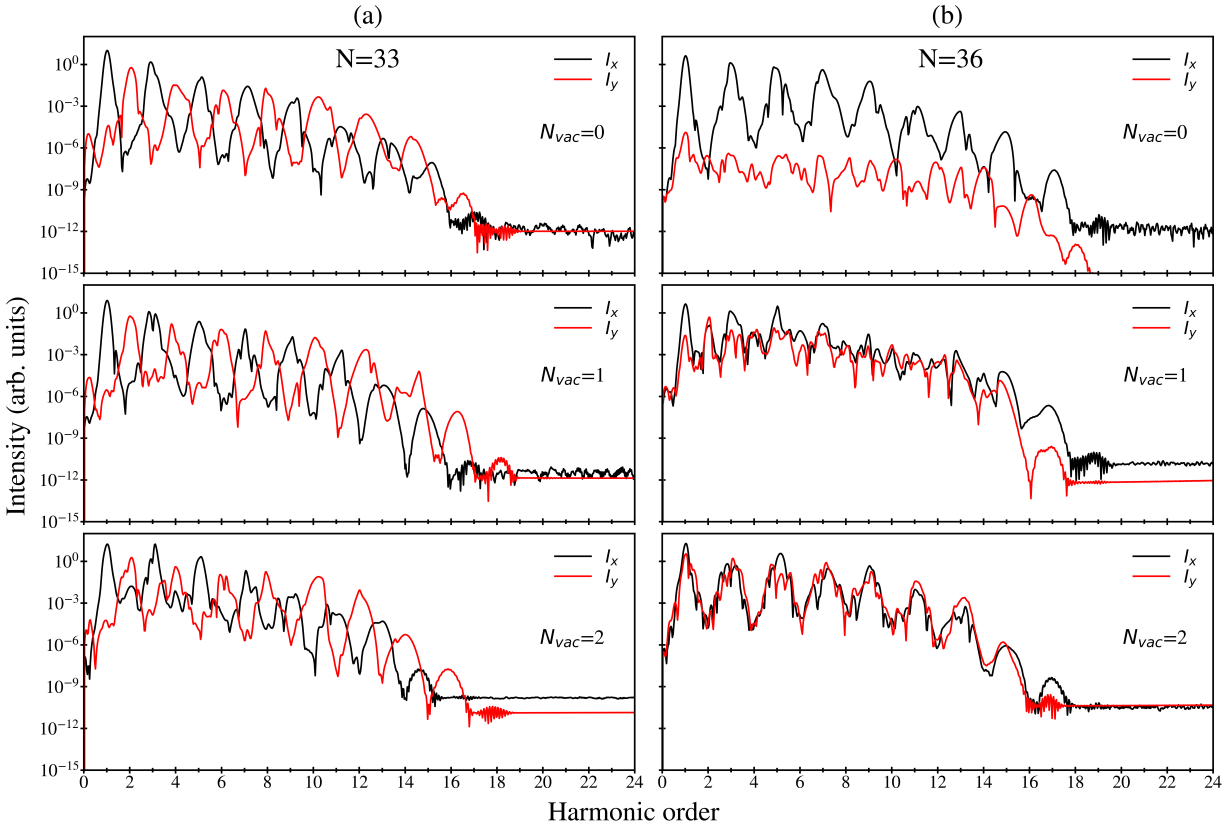


Figure 6.11 Emission spectra comparison : zigzag edged 33-atom (a); and armchair edged 36-atom triangular GQDs (b). The incident optical pulse is linearly polarized. The number of vacancies in the GQDs system is marked on each panel. The amplitude of the incident pulse is 0.3 V/Å.

dots in Fig. 6.14, accounting for intrinsic GQD, monovacancy, and divacancy in each panel comparatively. Fig. 6.13 clearly shows intensity corresponding to $x$ and $y$ components of dipole moments are almost identical for intrinsic zigzag edged GQDs ( top left panel), ensuring suppression of symmetry-related harmonics corresponding to $D_{3h}$ group. Similar results are observed for armchair-edged triangular GQDs, as shown in the top right panel of the exact figure. Regarding monovacancy and divacancy, there is a dominant $y$ component for the zigzag-edged dot shown in the mid and bottom left panels. Similar findings with boosted

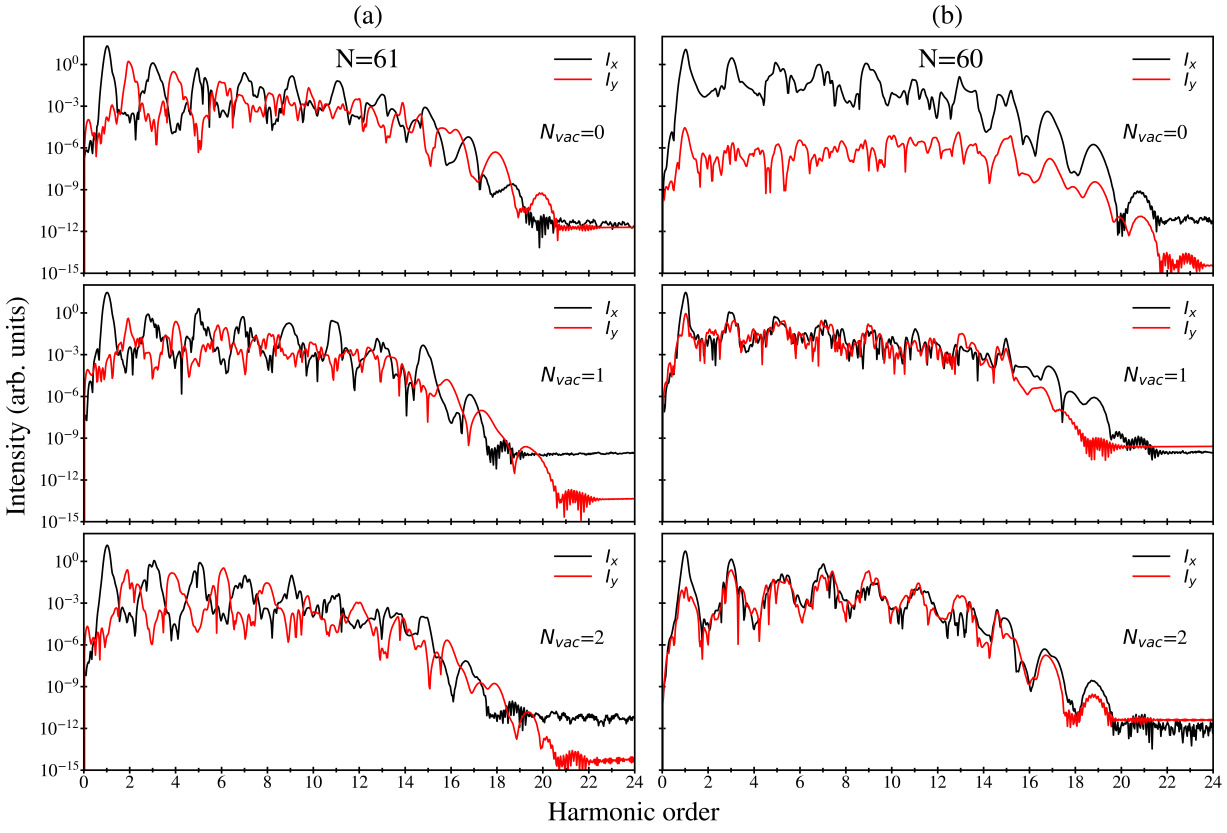


Figure 6.12 Emission spectra comparison : zigzag edged 61-atom (a); and armchair edged 60-atom triangular GQDs (b). The incident optical pulse is linearly polarized. The number of vacancies in the GQDs system is marked on each panel. The amplitude of the incident pulse is 0.3 V/Å.

$y$ components are observed for armchair edge GQDs in the central and bottom right panels.

Fig. 6.14 shows the variation in larger-sized dots, including zigzag and armchair edges in triangular GQDs. For the intrinsic case, in 61 atoms of zigzag-edged GQD, both $x$ and $y$ components contribute identical 'yields,' which in this context refers to the intensity of the dipole moment component. This behavior is shown in the top left panel panels results inconsistent with the zigzag edge small dots in small Fig. 6.13. Similar patterns are observed for the armchair-edged bigger dots in the top right panel. Regarding monovacancy

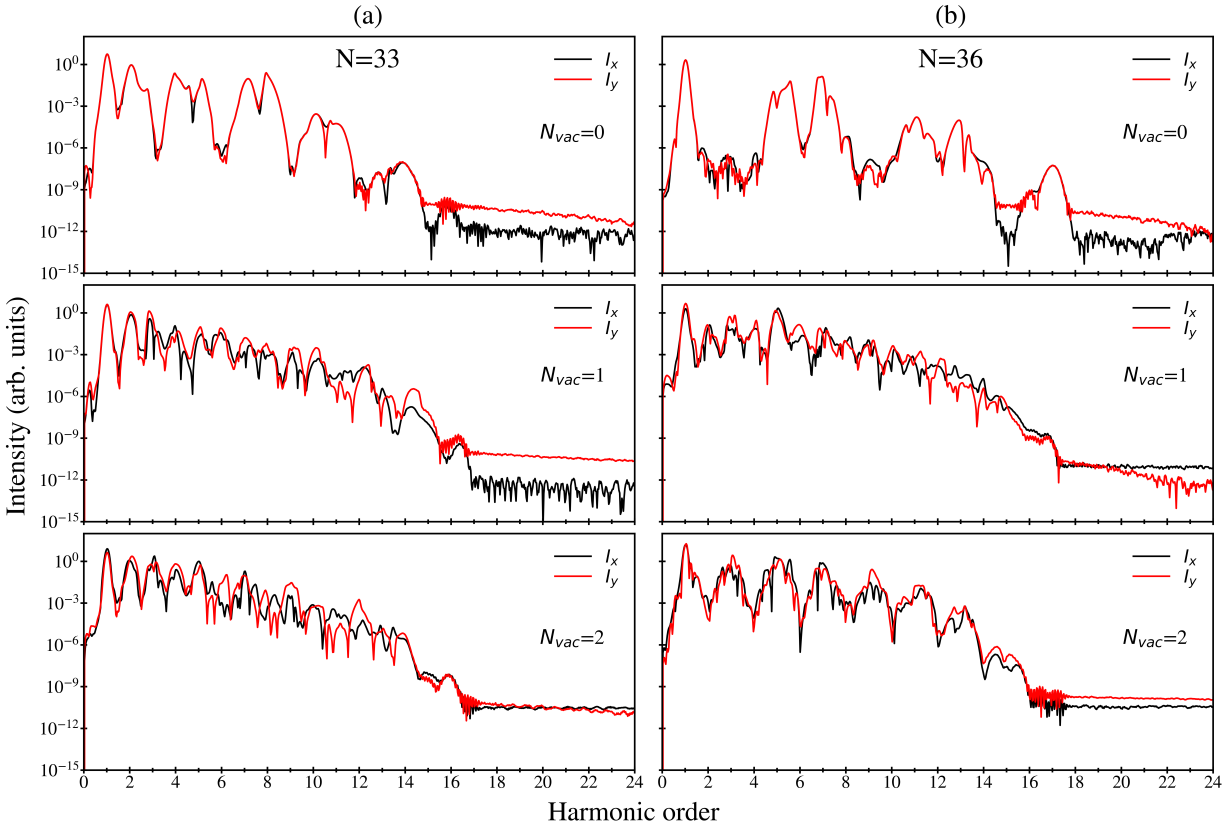


Figure 6.13 Emission spectra of triangular GQDs: zigzag edged 33-atom (a); and armchair edged 36-atom system (b). The incident optical pulse is circularly polarized. The number of vacancies in the GQDs system is marked on each panel. The amplitude of the incident pulse is 0.3 V/Å.

and divacancy, we see a significant contribution of the $y$ component as observed in small-sized dots, except for minor exceptions where intrinsic GQDs do for these cases. Similar results are shown for bigger armchair-edged GQDs in central and bottom right panels. As in small-sized triangular dots, all instances of big-sized dots respect the suppression of symmetry-related harmonics corresponding to $D_{3h}$ symmetry group in big-sized dots.

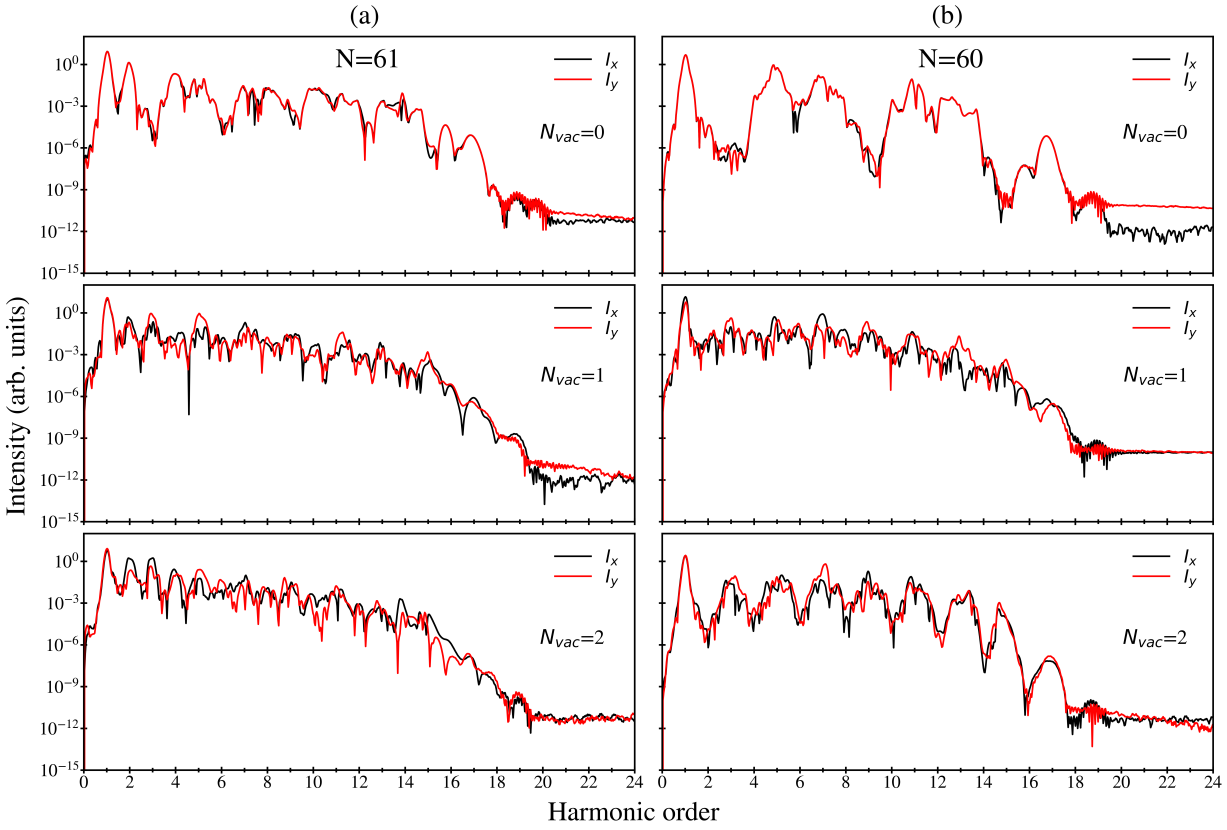


Figure 6.14 Emission spectra of triangular GQDs: zigzag edged 61-atom (a); and armchair edged 60-atom system (b). The incident optical pulse is circularly polarized. The number of vacancies in the GQDs system is marked on each panel. The amplitude of the incident pulse is 0.3 V/Å.

## 6.3 Conclusion

In this multisystem GQDs research, we conducted a comprehensive study on generating high-order harmonics in graphene quantum dots (GQDs) systems. Our theoretical exploration involved exciting GQDs with monovacancy and divacancy using a few femtosecond ultrafast optical pulses, which are concise bursts of light on the order of a few femtoseconds ($10^{-15}$ seconds). We meticulously varied the shape, size geometry, type of edge, and incident optical pulse magnitude and polarization to observe their intriguing effects on the high-order harmonics spectra. Our investigation into the role of the presence of vacancy in the GQDs has unveiled significant modifications in the high harmonics spectra. The presence of vacancy, even the monovacancy, profoundly impacts the symmetry-related harmonic peaks. In small-sized GQDs, both triangular and hexagonal, the vacancy enhances the emission spectra firmly under a linearly polarized pulse compared to large-sized ones, where the effect is less pronounced. Under circular polarization, all symmetry-related suppression observed for triangular and hexagonal dots are disrupted even with monovacancy, the absence of one atom in the GQDs. In zigzag-edged hexagonal and armchair-edged triangular GQDs, the monovacancy caused a zero energy edge state, a unique electronic state with no energy cost, in the energy profile. This state decreases the GQDs bandgap and enhances the high harmonics, providing additional channels for multiphoton excitation. In these systems, divacancy removes the zero energy edge state, which resembles the intrinsic GQD without vacancy but with enhanced emission spectra compared to the parent GQD (without vacancy). These results provide further insight into investigating the other 2D systems, including quantum

dots, and open up new avenues for enhancing the harmonics in the entire spectral region.

# CHAPTER 7
# CHAPTER 7 SUMMARY

In this dissertation, we conducted a theoretical investigation into the ultrafast nonlinear optical properties of graphene quantum dots (GQDs) systems, focusing on four specific areas of research: (i) generation of harmonics and its impact on relaxation, (ii) HHG governed by edge states in triangular GQDs, (iii) ellipticity dependence of HHG in GQDs, and (iv) HHG in GQDs with monovacancy or divacancy. We solved the neutral Hamiltonian of the system using the tight-binding model and established the basis sets for the density matrix operator. This operator is then used to reveal the optical nonlinearities, including nonzero conduction band population, dipole moment, and HHG, using theoretical formulations employing the time-dependent Schrödinger equation, quantum master equation, and density matrix described in the first two chapters of the dissertation. We introduced a finite relaxation time to study the dephasing mechanisms, which represent the loss of quantum information with time and help to correlate the findings with experimental results.

In Chapter 3, we studied the ultrafast electron dynamics of graphene quantum dots, focusing on generating high-order harmonics and how these harmonics change with finite relaxation time. Under the optical field produced by a few-femtosecond linear optical pulse, we studied the variation of nonlinear optical properties of the quantum dots. To achieve this goal, we vary the pulse amplitude and frequency of the incident optical pulse and dephasing times corresponding to nondiagonal elements. Under the finite relaxation time, nonlinearities, including residual conduction band population and HHG, are addressed in

GQDs placed in a short, robust, linearly polarized optical pulse. At short finite dephasing times, the ultrafast electron dynamics show significant irreversibility with a sizeable residual population of the excited quantum dot levels. When dephasing time increases, intensities correspond to a low-frequency boost, while the cut-off energy decreases regarding the HHG spectrum. The cut-off energy's dependence on the optical pulse's amplitude is also sensitive to the frequency of the pulse. This dependence for hexagonal GQDs is almost linear when the optical pulse frequency is much less than the quantum dot band gap. However, when the pulse frequency is comparable to the band gap, the cut-off energy shows saturation behavior at a large field amplitude, $> 0.4$ V/Å. This result motivates researchers to study other quantum dots and 2D materials theoretically and experimentally.

In Chapter 4, we focused on the research project, HHG governed by edge states in triangular graphene quantum dots. We studied the system of the different dots with zigzag edges, comparing the harmonic yield for partially populated edges. In the zigzag-edged triangular quantum dots, edge states - the zero energy states between the conduction band and valance band, arise near the fermi energy levels. These edge states modify the HHG spectra significantly in the dots, which is different from bulk states. When half the total number of edge states in the system are populated, even harmonics are suppressed significantly by optical pulse frequency below the band gap. When optical frequency approximates the bandgap (resonant case), the degree of suppression becomes relatively weak. Otherwise, all harmonics are of comparable intensities when no edge states are populated or edge states are partially populated. Such harmonics obtained in shorter wavelength regions with the input

of an ultrafast optical pulse of longer wavelengths have potential implications for controlling the HHG in the system of Quantum dots and other 2D materials, thus paving the way for practical applications in the field of quantum physics and material science.

Chapter 5 focuses on the theoretical study of HHG in graphene quantum dots in the elliptically polarized laser pulse. The elliptically polarized ultrashort pulse interacts with the system of quantum dots to reveal unique nonlinear behavior different from the linearized polarized optical field. The generated high harmonics are sensitive to pulse ellipticity, frequency, and amplitude. The high-order harmonics are more sensitive to pulse ellipticity than the lower-order harmonics. Some harmonics are strongly suppressed in the case of a circularly polarized pulse. The suppressed harmonic orders depend on the symmetry of the QD systems. For triangular dots, which have $D_{3h}$ symmetry, every third harmonic is suppressed, while for hexagonal dots with $D_{6h}$ symmetry, such suppression is observed for every sixth harmonic. In both cases, suppression is well pronounced beyond the third harmonics. These results indicate that the ellipticity of the incident optical pulse could be used to control and optimize HHG in graphene quantum dots and other 2D materials.

The project titled HHG in GQDs with monovacancy or divacancy delves into the intricate influence of defects in high harmonic generation in graphene quantum dots, detailed in Chapter 6. We are deeply interested in how the generated harmonics change in the imperfect crystal with monovacancy or divacancy in the GQDs. These defects are altering the HHg spectrum significantly; for example, in hexagonal GQD with zigzag edges, even order harmonics arise with monovacancy, while with divacancy, even harmonic disappears and

only odd harmonics occurred, preserving the symmetry of the system as in GQD, without vacancy. In triangular GQDs with zigzag edges, nonmonotonic boost-up of harmonics with monovacancy and divacancy was observed. The monovacancy strongly changes the HHG spectrum in all cases, showcasing our research's intricate and complex nature. These findings broaden the current understanding of GQDs and provide new insights into their optical properties, which can be crucial for developing novel quantum devices and materials.

This dissertation further provides future directions for researchers investigating ultrafast electron dynamics of 2D materials, including nanostructures and quantum dots. The projects mentioned in the current thesis can be extended to other 2D materials, such as transition metal dichalcogenides, to compare and analyze nonlinear optical properties such as HHG. We can explore such nonlinearities as varying polarization, pulse magnitude of the incident optical pulse, and varying shape, size, geometry, and type of edge of the nonlinear material. To advance the area, I have primarily five future research projects in my mind: (i) Ultrafast electron dynamics of graphene quantum dots with impurities or doping, (ii) High Harmonic generation in transition metal dichalcogenides using extended Hubbard Hamiltonian (iii) Comparative study of harmonic efficiency between monolayers and heterostructures of 2D material (iv) Anomalous Hall effect and Faraday number variation between sharp-edged nanostructures and (v) Role of Berry curvatures for understanding interband and intraband harmonics in low-dimensional materials.

Motivated by the significant enhancement of high-order harmonics with vacancies in GQD with vacancies, I plan to study the mechanism of electron dynamics and observe the

emission spectra and their variation compared to intrinsic GQD. There is an expectation of some degree of enhancement with impurities or doping. Introducing vacancies or adding a few atoms as impurities could significantly enhance the radiation intensity. Such extrinsic GQDs would be a great candidate for investigating optoelectronics properties for future devices. The second future project extends the current study in transition metal dichalcogenides, other promising candidates for studying optical nonlinearities in 2D materials. To achieve this goal, I plan to employ extended Hubbard Hamiltonian, which includes interaction terms such as coulomb attraction and repulsion. This study could provide more inclusive results than the tight-biding Hamiltonian, where only hoping between the nearest neighbors is considered. The third future research study compares the harmonic efficiency between 2D materials to determine the optimal material for maximizing efficiency. This research can further be extended to other 2D heterostructures to compare the efficiencies between monolayer and heterostructure. Such a study could provide further insight into the search for the best material to enhance harmonic efficiency. The fourth future research project aims to study the fundamental aspect of the Faraday number and anomalous quantum Hall effect in sharp-edged nanostructures. The sharp-edged nanostructures are unique because they can exhibit anomalous quantum Hall without a magnetic field, and a study of Faraday's numbers can be included. The finding could lead to a new perspective to compare the quantum Hall effect without a magnetic field produced so that it could be different from the quantum Hall with a magnetic field. The final future research project attempts to investigate the role of Berry curvature in investigating interband and intraband harmonics in low-dimensional

materials. This study helps to understand the topology, symmetry, and relation between inter and intraband dynamics and corresponding optical nonlinearity in 2D materials and heterostructures, including layered structures and quantum dots. Overall, the future directions indicated in this dissertation could provide additional insight into investigating and understanding symmetry and topology-related linear and nonlinear effects, enhancing the harmonic efficiency, and selecting optimal material for harmonic yield employing advances and extended theoretical models, including extended Hubbard Hamiltonian.

# APPENDICES

# TABLE OF CONTENTS IN APPENDICES

# LIST OF OF TABLES IN APPENDICES

# LIST OF OF FIGURES IN APPENDICES

## A Symmetry Groups

This section presents tabular representation for $D_{3h}$ and $D_{6h}$ symmetry groups. Table 1 represents the $D_{3h}$ symmetry groups and table 2 represents the $D_{6h}$ symmetry groups. This information in the symmetry character table is adapted from ref.[156].

Table 1: Character table for the $D_{3h}$ point group

| $D_{3h}$ | $E$ | $2C_3$ | $3C_2$ | $\sigma_h$ | $2S_3$ | $3\sigma_v$ | Basis |
|---|---|---|---|---|---|---|---|
| $A_1'$ | 1 | 1 | 1 | 1 | 1 | 1 | $a_{xx}+a_{yy}, a_{zz}$ |
| $A_1''$ | 1 | 1 | 1 | -1 | -1 | -1 | |
| $A_2'$ | 1 | 1 | -1 | 1 | 1 | -1 | $R_z$ |
| $A_2''$ | 1 | 1 | -1 | -1 | -1 | 1 | $z$ |
| $E'$ | 2 | -1 | 0 | 2 | -1 | 0 | $(x,y),(a_{xx}-a_{yy}, a_{xy})$ |
| $E''$ | 2 | -1 | 0 | -2 | 1 | 0 | $(R_x,R_y),(a_{xz}, a_{yz})$ |

Table 2: Character table for the $D_{6h}$ point group

| $D_{6h}$ | $E$ | $2C_6$ | $2C_3$ | $C_2$ | $3C_2'$ | $3C_2''$ | $I$ | $2S_3$ | $2S_6$ | $\sigma_h$ | $3\sigma_d$ | $3\sigma_v$ | Basis |
|---|---|---|---|---|---|---|---|---|---|---|---|---|---|
| $A_{1g}$ | 1 | 1 | 1 | 1 | 1 | 1 | 1 | 1 | 1 | 1 | 1 | 1 | $a_{xx}+a_{yy}, a_{zz}$ |
| $A_{1u}$ | 1 | 1 | 1 | 1 | 1 | 1 | -1 | -1 | -1 | -1 | -1 | -1 | |
| $A_{2g}$ | 1 | 1 | 1 | 1 | -1 | -1 | 1 | 1 | 1 | 1 | -1 | -1 | $R_z$ |
| $A_{2u}$ | 1 | 1 | 1 | 1 | -1 | -1 | -1 | -1 | -1 | -1 | 1 | 1 | $z$ |
| $B_{1g}$ | 1 | -1 | 1 | -1 | 1 | -1 | 1 | -1 | 1 | -1 | 1 | -1 | |
| $B_{1u}$ | 1 | -1 | 1 | -1 | 1 | -1 | -1 | 1 | -1 | 1 | -1 | 1 | |
| $B_{2g}$ | 1 | -1 | 1 | -1 | -1 | 1 | 1 | -1 | 1 | -1 | -1 | 1 | $R_z$ |
| $B_{2u}$ | 1 | -1 | 1 | -1 | -1 | 1 | -1 | 1 | -1 | 1 | 1 | -1 | |
| $E_{1g}$ | 2 | 1 | -1 | -2 | 0 | 0 | 2 | 1 | -1 | -2 | 0 | 0 | $(R_x,R_y),(a_{xz}, a_{yz})$ |
| $E_{1u}$ | 2 | 1 | -1 | -2 | 0 | 0 | -2 | -1 | 1 | 2 | 0 | 0 | $(x,y)$ |
| $E_{2g}$ | 2 | -1 | -1 | 2 | 0 | 0 | 2 | -1 | -1 | 2 | 0 | 0 | $(a_{xx}-a_{yy}, a_{xy})$ |
| $E_{2u}$ | 2 | -1 | -1 | 2 | 0 | 0 | -2 | 1 | 1 | -2 | 0 | 0 | |

## B Python codes for Pulse profiles

This section presents the Python codes to represent the incident optical pulse used to complete the research projects in this dissertation. We studied the system for linear, circular, and elliptical polarization of the incident optical pulse described by the Python code below.

```
# #%%%% (1) Linear Pulse
import numpy as np
import matplotlib.pyplot as plt

#%%% Assign the values
hbar=0.6582119569 # [ eV fs] reduced Planck constant
step=13/300
tau_0=10     # [fs] duration of pulse

#%%%%% (i)  x-component

def Fx(t):
    eps = 0  # Linear polarization
    F_0 = 0.3  # Pulse amplitude
    F_0x = F_0/(np.sqrt(1+eps**2))
    T = 2*np.pi*hbar  # [fs] corresponds to pulse frequency 1 eV
    return F_0x*(np.exp(-(t/tau_0)**2)*np.cos(((2*np.pi)/T)*t))

pvalsx = np.array([Fx(i)
                   for i in np.arange(-3*tau_0, 10*tau_0, step)])
Nx = len(pvalsx)

#%%%  (ii) y-component

def Fy(t):
    eps = 0   # Linear polarization
    F_0 = 0.3  # Pulse amplitude
    F_0y = eps*(F_0/(np.sqrt(1+eps**2)))
    T = 2*np.pi*hbar  #   [fs] corresponds to pulse frequency 1 eV
    return F_0y*(np.exp(-(t/tau_0)**2)*np.sin(((2*np.pi)/T)*t))

pvalsy = np.array([Fy(i)
                   for i in np.arange(-3*tau_0, 10*tau_0, step)])
Ny = len(pvalsy)
N = Nx

#%% Plot
plt.plot(np.arange(-3*tau_0, 10*tau_0, step), pvalsx, 'b')
plt.plot(np.arange(-3*tau_0, 10*tau_0, step), pvalsy, 'r')
plt.ylabel('Field amplitude')
plt.xlabel('t (fs)')
plt.title('Pulse profile')
plt.show()
```

Figure 1  Linear pulse code

```
#%%%% (2) Circular Pulse
import numpy as np
import matplotlib.pyplot as plt

#%%% Assign the values
hbar=0.6582119569 # [ eV fs] reduced Planck constant
step=13/300
tau_0=10     # [fs] duration of pulse

#%%%%% (i)  x-component

def Fx(t):
    eps = 1  # Circular polarization
    F_0 = 0.3  # Pulse amplitude
    F_0x = F_0/(np.sqrt(1+eps**2))
    T = 2*np.pi*hbar  # [fs] corresponds to pulse frequency 1 eV
    return F_0x*(np.exp(-(t/tau_0)**2)*np.cos(((2*np.pi)/T)*t))

pvalsx = np.array([Fx(i)
                   for i in np.arange(-3*tau_0, 10*tau_0, step)])
Nx = len(pvalsx)

#%%%  (ii) y-component

def Fy(t):
    eps = 1   # Circular polarization
    F_0 = 0.3  # Pulse amplitude
    F_0y = eps*(F_0/(np.sqrt(1+eps**2)))
    T = 2*np.pi*hbar  #   [fs] corresponds to pulse frequency 1 eV
    return F_0y*(np.exp(-(t/tau_0)**2)*np.sin(((2*np.pi)/T)*t))

pvalsy = np.array([Fy(i)
                   for i in np.arange(-3*tau_0, 10*tau_0, step)])
Ny = len(pvalsy)
N = Nx

#%% Plot
plt.plot(np.arange(-3*tau_0, 10*tau_0, step), pvalsx, 'b')
plt.plot(np.arange(-3*tau_0, 10*tau_0, step), pvalsy, 'r')
plt.ylabel('Field amplitude')
plt.xlabel('t (fs)')
plt.title('Pulse profile')
plt.show()
```

Figure 2  Circular pulse code

```
#%%%% (3) Elliptical Pulse
import numpy as np
import matplotlib.pyplot as plt

#%%% Assign the values
hbar=0.6582119569 # [ eV fs] reduced Planck constant
step=13/300
tau_0=10     # [fs] duration of pulse

#%%%%% (i)  x-component

def Fx(t):
    eps = 0.25  # elliptical polarization with finite ellipticiy
    F_0 = 0.3  # Pulse amplitude
    F_0x = F_0/(np.sqrt(1+eps**2))
    T = 2*np.pi*hbar  # [fs] corresponds to pulse frequency 1 eV
    return F_0x*(np.exp(-(t/tau_0)**2)*np.cos(((2*np.pi)/T)*t))

pvalsx = np.array([Fx(i)
                   for i in np.arange(-3*tau_0, 10*tau_0, step)])
Nx = len(pvalsx)

#%%%  (ii) y-component

def Fy(t):
    eps = 0.25   # elliptical polarization with finite ellipticiy
    F_0 = 0.3  # Pulse amplitude
    F_0y = eps*(F_0/(np.sqrt(1+eps**2)))
    T = 2*np.pi*hbar  #   [fs] corresponds to pulse frequency 1 eV
    return F_0y*(np.exp(-(t/tau_0)**2)*np.sin(((2*np.pi)/T)*t))

pvalsy = np.array([Fy(i)
                   for i in np.arange(-3*tau_0, 10*tau_0, step)])
Ny = len(pvalsy)
N = Nx

#%% Plot
plt.plot(np.arange(-3*tau_0, 10*tau_0, step), pvalsx, 'b')
plt.plot(np.arange(-3*tau_0, 10*tau_0, step), pvalsy, 'r')
plt.ylabel('Field amplitude')
plt.xlabel('t (fs)')
plt.title('Pulse profile')
plt.show()
```

Figure 3  Elliptical pulse code

# REFERENCES

[1] A. K. Geim, Graphene: status and prospects, science 324 (5934) (2009) 1530–1534.

[2] N. Peres, Graphene, new physics in two dimensions, Europhysics News 40 (3) (2009) 17–20.

[3] A. Rozhkov, G. Giavaras, Y. P. Bliokh, V. Freilikher, F. Nori, Electronic properties of mesoscopic graphene structures: Charge confinement and control of spin and charge transport, Physics Reports 503 (2-3) (2011) 77–114.

[4] S. A. O. Motlagh, V. Apalkov, Absorption properties of graphene quantum dots under ultrashort optical pulses, Physical Review B 104 (4) (2021) 045421.

[5] A. H. Zewail, Femtochemistry: Atomic-scale dynamics of the chemical bond, The Journal of Physical Chemistry A 104 (24) (2000) 5660–5694.

[6] M. Khokhlova, E. Pisanty, A. Zaïr, Shining the shortest flashes of light on the secret life of electrons, Advanced Photonics 5 (6) (2023) 060501–060501.

[7] F. Krausz, M. I. Stockman, Attosecond metrology: from electron capture to future signal processing, Nature Photonics 8 (3) (2014) 205–213.

[8] H. Fattahi, H. G. Barros, M. Gorjan, T. Nubbemeyer, B. Alsaif, C. Y. Teisset, M. Schultze, S. Prinz, M. Haefner, M. Ueffing, et al., Third-generation femtosecond technology, Optica 1 (1) (2014) 45–63.

[9] M. Tanter, M. Fink, Ultrafast imaging in biomedical ultrasound, IEEE transactions on ultrasonics, ferroelectrics, and frequency control 61 (1) (2014) 102–119.

[10] W. Kaiser, D. H. Auston, Ultrashort laser pulses: generation and applications, Springer, 1993.

[11] E. Goulielmakis, V. S. Yakovlev, A. L. Cavalieri, M. Uiberacker, V. Pervak, A. Apolonski, R. Kienberger, U. Kleineberg, F. Krausz, Attosecond control and measurement: lightwave electronics, Science 317 (5839) (2007) 769–775.

[12] R. Gutzler, M. Garg, C. R. Ast, K. Kuhnke, K. Kern, Light–matter interaction at atomic scales, Nature Reviews Physics 3 (6) (2021) 441–453.

[13] J. Weiner, P.-T. Ho, Light-matter interaction: fundamentals and applications, Vol. 1, John Wiley & Sons, 2008.

[14] A. Saleem, I. Afzal, Y. Javed, Y. Jamil, Fundamentals of light–matter interaction, in: Modern Luminescence from Fundamental Concepts to Materials and Applications, Elsevier, 2023, pp. 185–218.

[15] J. D. Cox, F. Javier García de Abajo, Electrically tunable nonlinear plasmonics in graphene nanoislands, Nature communications 5 (1) (2014) 5725.

[16] R. Santra, A. Gordon, Three-step model for high-harmonic generation in many-electron systems, Physical review letters 96 (7) (2006) 073906.

[17] A. Fleischer, Generation of higher-order harmonics upon the addition of high-frequency xuv radiation to ir radiation: Generalization of the three-step model, Physical Review A—Atomic, Molecular, and Optical Physics 78 (5) (2008) 053413.

[18] S. Ghimire, A. D. DiChiara, E. Sistrunk, P. Agostini, L. F. DiMauro, D. A. Reis, Observation of high-order harmonic generation in a bulk crystal, Nature physics 7 (2)

(2011) 138–141.

[19] P. B. Corkum, F. Krausz, Attosecond science, Nature physics 3 (6) (2007) 381–387.

[20] K. Blum, Density matrix theory and applications, Vol. 64, Springer Science & Business Media, 2012.

[21] L. D. Landau, E. M. Lifshitz, Quantum mechanics: non-relativistic theory, Vol. 3, Elsevier, 2013.

[22] B. Di Bartolo, Optical properties of excited states in solids, Vol. 301, Springer Science & Business Media, 2012.

[23] K. Ahnert, M. Mulansky, Odeint–solving ordinary differential equations in c++, in: AIP Conference Proceedings, Vol. 1389, American Institute of Physics, 2011, pp. 1586–1589.

[24] R. Mersereau, T. Speake, A unified treatment of cooley-tukey algorithms for the evaluation of the multidimensional dft, IEEE Transactions on Acoustics, Speech, and Signal Processing 29 (5) (1981) 1011–1018.

[25] P. Virtanen, R. Gommers, T. E. Oliphant, M. Haberland, T. Reddy, D. Cournapeau, E. Burovski, P. Peterson, W. Weckesser, J. Bright, et al., Scipy 1.0: fundamental algorithms for scientific computing in python, Nature methods 17 (3) (2020) 261–272.

[26] S. Gnawali, R. Ghimire, K. R. Magar, S. J. Hossaini, V. Apalkov, Ultrafast electron dynamics of graphene quantum dots: High harmonic generation, Phys. Rev. B 106 (2022) 075149. doi:10.1103/PhysRevB.106.075149.

URL https://link.aps.org/doi/10.1103/PhysRevB.106.075149

[27] F. Krausz, M. Ivanov, Attosecond physics, Reviews of modern physics 81 (1) (2009) 163.

[28] S. Y. Kruchinin, F. Krausz, V. S. Yakovlev, Colloquium: Strong-field phenomena in periodic systems, Reviews of Modern Physics 90 (2) (2018) 021002.

[29] A. Schiffrin, T. Paasch-Colberg, N. Karpowicz, V. Apalkov, D. Gerster, S. Mühlbrandt, M. Korbman, J. Reichert, M. Schultze, S. Holzner, et al., Optical-field-induced current in dielectrics, Nature 493 (7430) (2013) 70–74.

[30] J. Kiemle, P. Zimmermann, A. W. Holleitner, C. Kastl, Light-field and spin-orbit-driven currents in van der waals materials, Nanophotonics 9 (9) (2020) 2693–2708.

[31] T. Paasch-Colberg, A. Schiffrin, N. Karpowicz, S. Kruchinin, Ö. Sağlam, S. Keiber, O. Razskazovskaya, S. Mühlbrandt, A. Alnaser, M. Kübel, et al., Solid-state light-phase detector, Nature Photonics 8 (3) (2014) 214–218.

[32] T. Higuchi, C. Heide, K. Ullmann, H. B. Weber, P. Hommelhoff, Light-field-driven currents in graphene, Nature 550 (7675) (2017) 224–228.

[33] E. Gruber, R. A. Wilhelm, R. Pétuya, V. Smejkal, R. Kozubek, A. Hierzenberger, B. C. Bayer, I. Aldazabal, A. K. Kazansky, F. Libisch, et al., Ultrafast electronic response of graphene to a strong and localized electric field, Nature communications 7 (1) (2016) 13948.

[34] S. Sederberg, D. Zimin, S. Keiber, F. Siegrist, M. S. Wismer, V. S. Yakovlev, I. Floss, C. Lemell, J. Burgdörfer, M. Schultze, et al., Attosecond optoelectronic field measurement in solids, Nature communications 11 (1) (2020) 430.

[35] G. Vampa, J. Lu, Y. S. You, D. R. Baykusheva, M. Wu, H. Liu, K. J. Schafer, M. B. Gaarde, D. A. Reis, S. Ghimire, Attosecond synchronization of extreme ultraviolet high harmonics from crystals, Journal of Physics B: Atomic, Molecular and Optical Physics 53 (14) (2020) 144003.

[36] M. Trushin, A. Grupp, G. Soavi, A. Budweg, D. De Fazio, U. Sassi, A. Lombardo, A. C. Ferrari, W. Belzig, A. Leitenstorfer, et al., Ultrafast pseudospin dynamics in graphene, Physical Review B 92 (16) (2015) 165429.

[37] S. A. Oliaei Motlagh, J.-S. Wu, V. Apalkov, M. I. Stockman, Femtosecond valley polarization and topological resonances in transition metal dichalcogenides, Physical Review B 98 (8) (2018) 081406.

[38] D. Sun, J.-W. Lai, J.-C. Ma, Q.-S. Wang, J. Liu, Review of ultrafast spectroscopy studies of valley carrier dynamics in two-dimensional semiconducting transition metal dichalcogenides, Chinese Physics B 26 (3) (2017) 037801.

[39] F. Gesuele, Ultrafast hyperspectral transient absorption spectroscopy: Application to single layer graphene, in: Photonics, Vol. 6, MDPI, 2019, p. 95.

[40] J. Zhang, H. Ouyang, X. Zheng, J. You, R. Chen, T. Zhou, Y. Sui, Y. Liu, T. Jiang, et al., Ultrafast saturable absorption of mos 2 nanosheets under different pulse-width excitation conditions, Optics Letters 43 (2) (2018) 243–246.

[41] R. W. Boyd, A. L. Gaeta, E. Giese, Nonlinear optics, in: Springer Handbook of Atomic, Molecular, and Optical Physics, Springer, 2008, pp. 1097–1110.

[42] J. L. Krause, K. J. Schafer, K. C. Kulander, High-order harmonic generation from

atoms and ions in the high intensity regime, Physical Review Letters 68 (24) (1992) 3535.

[43] D. Von der Linde, T. Engers, G. Jenke, P. Agostini, G. Grillon, E. Nibbering, A. Mysyrowicz, A. Antonetti, Generation of high-order harmonics from solid surfaces by intense femtosecond laser pulses, Physical Review A 52 (1) (1995) R25.

[44] P. Norreys, M. Zepf, S. Moustaizis, A. Fews, J. Zhang, P. Lee, M. Bakarezos, C. Danson, A. Dyson, P. Gibbon, et al., Efficient extreme uv harmonics generated from picosecond laser pulse interactions with solid targets, Physical Review Letters 76 (11) (1996) 1832.

[45] G. Vampa, T. Hammond, N. Thiré, B. Schmidt, F. Légaré, C. McDonald, T. Brabec, P. Corkum, Linking high harmonics from gases and solids, Nature 522 (7557) (2015) 462–464.

[46] G. Ndabashimiye, S. Ghimire, M. Wu, D. A. Browne, K. J. Schafer, M. B. Gaarde, D. A. Reis, Solid-state harmonics beyond the atomic limit, Nature 534 (7608) (2016) 520–523.

[47] H. Liu, Y. Li, Y. S. You, S. Ghimire, T. F. Heinz, D. A. Reis, High-harmonic generation from an atomically thin semiconductor, Nature Physics 13 (3) (2017) 262–265.

[48] Y. S. You, Y. Yin, Y. Wu, A. Chew, X. Ren, F. Zhuang, S. Gholam-Mirzaei, M. Chini, Z. Chang, S. Ghimire, High-harmonic generation in amorphous solids, Nature communications 8 (1) (2017) 724.

[49] N. Klemke, N. Tancogne-Dejean, G. M. Rossi, Y. Yang, F. Scheiba, R. Mainz, G. Di Sci-

acca, A. Rubio, F. Kärtner, O. Mücke, Polarization-state-resolved high-harmonic spectroscopy of solids, Nature communications 10 (1) (2019) 1319.

[50] M. Lewenstein, P. Balcou, M. Y. Ivanov, A. L'huillier, P. B. Corkum, Theory of high-harmonic generation by low-frequency laser fields, Physical Review A 49 (3) (1994) 2117.

[51] D. Golde, T. Meier, S. W. Koch, High harmonics generated in semiconductor nanostructures by the coupled dynamics of optical inter-and intraband excitations, Physical Review B 77 (7) (2008) 075330.

[52] N. Klemke, O. Mücke, A. Rubio, F. X. Kärtner, N. Tancogne-Dejean, Role of intraband dynamics in the generation of circularly polarized high harmonics from solids, Physical Review B 102 (10) (2020) 104308.

[53] I. Kilen, M. Kolesik, J. Hader, J. V. Moloney, U. Huttner, M. K. Hagen, S. W. Koch, Propagation induced dephasing in semiconductor high-harmonic generation, Physical review letters 125 (8) (2020) 083901.

[54] Z. Xie, F. Zhang, Z. Liang, T. Fan, Z. Li, X. Jiang, H. Chen, J. Li, H. Zhang, Revealing of the ultrafast third-order nonlinear optical response and enabled photonic application in two-dimensional tin sulfide, Photonics Research 7 (5) (2019) 494–502.

[55] L. Lu, W. Wang, L. Wu, X. Jiang, Y. Xiang, J. Li, D. Fan, H. Zhang, All-optical switching of two continuous waves in few layer bismuthene based on spatial cross-phase modulation, Acs Photonics 4 (11) (2017) 2852–2861.

[56] L. Wu, Y. Dong, J. Zhao, D. Ma, W. Huang, Y. Zhang, Y. Wang, X. Jiang, Y. Xiang,

J. Li, et al., Kerr nonlinearity in 2d graphdiyne for passive photonic diodes, Advanced Materials 31 (14) (2019) 1807981.

[57] L. Gao, C. Li, W. Huang, S. Mei, H. Lin, Q. Ou, Y. Zhang, J. Guo, F. Zhang, S. Xu, et al., Mxene/polymer membranes: synthesis, properties, and emerging applications, Chemistry of Materials 32 (5) (2020) 1703–1747.

[58] R. Ashoori, Electrons in artificial atoms, Nature 379 (6564) (1996) 413–419.

[59] T. Chakraborty, Quantum dots: A survey of the properties of artificial atoms (1999).

[60] Y. Arakawa, H. Sakaki, Multidimensional quantum well laser and temperature dependence of its threshold current, Applied physics letters 40 (11) (1982) 939–941.

[61] D. Loss, D. P. DiVincenzo, Quantum computation with quantum dots, Physical Review A 57 (1) (1998) 120.

[62] X. Michalet, F. F. Pinaud, L. A. Bentolila, J. M. Tsay, S. Doose, J. J. Li, G. Sundaresan, A. Wu, S. Gambhir, S. Weiss, Quantum dots for live cells, in vivo imaging, and diagnostics, science 307 (5709) (2005) 538–544.

[63] V. Veeramani, Z. Bao, M.-H. Chan, H.-C. Wang, A. Jena, H. Chang, S.-F. Hu, R.-S. Liu, Quantum dots for light conversion, therapeutic and energy storage applications, Journal of Solid State Chemistry 270 (2019) 71–84.

[64] Q. Liu, J. Sun, K. Gao, N. Chen, X. Sun, D. Ti, C. Bai, R. Cui, L. Qu, Graphene quantum dots for energy storage and conversion: from fabrication to applications, Materials Chemistry Frontiers 4 (2) (2020) 421–436.

[65] K. K. Hansen, D. Bauer, L. B. Madsen, Finite-system effects on high-order harmonic

generation: From atoms to solids, Physical Review A 97 (4) (2018) 043424.

[66] D. Pan, J. Zhang, Z. Li, M. Wu, Hydrothermal route for cutting graphene sheets into blue-luminescent graphene quantum dots, Advanced materials 22 (6) (2010) 734–738.

[67] S. Chung, R. A. Revia, M. Zhang, Graphene quantum dots and their applications in bioimaging, biosensing, and therapy, Advanced Materials 33 (22) (2021) 1904362.

[68] H. Sun, L. Wu, W. Wei, X. Qu, Recent advances in graphene quantum dots for sensing, Materials today 16 (11) (2013) 433–442.

[69] M. Bacon, S. J. Bradley, T. Nann, Graphene quantum dots, Particle & Particle Systems Characterization 31 (4) (2014) 415–428.

[70] K. S. Novoselov, A. K. Geim, S. V. Morozov, D.-e. Jiang, Y. Zhang, S. V. Dubonos, I. V. Grigorieva, A. A. Firsov, Electric field effect in atomically thin carbon films, science 306 (5696) (2004) 666–669.

[71] A. K. Geim, K. S. Novoselov, The rise of graphene, Nature materials 6 (3) (2007) 183–191.

[72] A. C. Neto, F. Guinea, N. M. Peres, K. S. Novoselov, A. K. Geim, The electronic properties of graphene, Reviews of modern physics 81 (1) (2009) 109.

[73] D. Abergel, V. Apalkov, J. Berashevich, K. Ziegler, T. Chakraborty, Properties of graphene: a theoretical perspective, Advances in Physics 59 (4) (2010) 261–482.

[74] S. D. Sarma, S. Adam, E. Hwang, E. Rossi, Electronic transport in two-dimensional graphene, Reviews of modern physics 83 (2) (2011) 407.

[75] A. F. Young, P. Kim, Electronic transport in graphene heterostructures, Annu. Rev.

Condens. Matter Phys. 2 (1) (2011) 101–120.

[76] H. K. Kelardeh, V. Apalkov, M. I. Stockman, Graphene in ultrafast and superstrong laser fields, Physical Review B 91 (4) (2015) 045439.

[77] S. A. Oliaei Motlagh, F. Nematollahi, V. Apalkov, M. I. Stockman, Topological resonance and single-optical-cycle valley polarization in gapped graphene, Physical Review B 100 (11) (2019) 115431.

[78] S. A. Oliaei Motlagh, V. Apalkov, Absorption properties of graphene quantum dots under ultrashort optical pulses, Physical Review B 104 (4) (2021) 045421.

[79] S. Hossaini, R. Ghimire, V. Apalkov, Ultrafast nonlinear absorption of tmdc quantum dots, Physica E: Low-dimensional Systems and Nanostructures 142 (2022) 115239.

[80] Z.-Y. Chen, R. Qin, High harmonic generation in graphene–boron nitride heterostructures, Journal of Materials Chemistry C 8 (35) (2020) 12085–12091.

[81] G. Vampa, C. McDonald, G. Orlando, P. Corkum, T. Brabec, Semiclassical analysis of high harmonic generation in bulk crystals, Physical Review B 91 (6) (2015) 064302.

[82] Y. W. Kim, T.-J. Shao, H. Kim, S. Han, S. Kim, M. Ciappina, X.-B. Bian, S.-W. Kim, Spectral interference in high harmonic generation from solids, ACS Photonics 6 (4) (2019) 851–857.

[83] M. Ivanov, O. Smirnova, Opportunities for sub-laser-cycle spectroscopy in condensed phase, Chemical Physics 414 (2013) 3–9.

[84] E. Goulielmakis, T. Brabec, High harmonic generation in condensed matter, Nature Photonics 16 (6) (2022) 411–421.

[85] S. Gnawali, V. Apalkov, High harmonic generation governed by edge states in triangular graphene quantum dots, Phys. Rev. B 108 (2023) 115434. doi:10.1103/PhysRevB.108.115434.

URL https://link.aps.org/doi/10.1103/PhysRevB.108.115434

[86] J. Fernández-Rossier, J. J. Palacios, Magnetism in graphene nanoislands, Physical Review Letters 99 (17) (2007) 177204.

[87] K. Nakagawa, H. Hirori, S. A. Sato, H. Tahara, F. Sekiguchi, G. Yumoto, M. Saruyama, R. Sato, T. Teranishi, Y. Kanemitsu, Size-controlled quantum dots reveal the impact of intraband transitions on high-order harmonic generation in solids, Nature Physics 18 (8) (2022) 874–878.

[88] S. Gnawali, V. Apalkov, High-order harmonic generation in graphene quantum dots in the field of an elliptically polarized pulse, Phys. Rev. B 109 (2024) 165121. doi:10.1103/PhysRevB.109.165121.

URL https://link.aps.org/doi/10.1103/PhysRevB.109.165121

[89] M. Lewenstein, P. Balcou, M. Y. Ivanov, A. L'Huillier, P. B. Corkum, Theory of high-harmonic generation by low-frequency laser fields, Phys. Rev. A 49 (1994) 2117–2132. doi:10.1103/PhysRevA.49.2117.

URL https://link.aps.org/doi/10.1103/PhysRevA.49.2117

[90] G. Vampa, C. R. McDonald, G. Orlando, D. D. Klug, P. B. Corkum, T. Brabec, Theoretical analysis of high-harmonic generation in solids, Phys. Rev. Lett. 113 (2014) 073901. doi:10.1103/PhysRevLett.113.073901.

URL https://link.aps.org/doi/10.1103/PhysRevLett.113.073901

[91] B. Dromey, M. Zepf, A. Gopal, K. Lancaster, M. Wei, K. Krushelnick, M. Tatarakis, N. Vakakis, S. Moustaizis, R. Kodama, et al., High harmonic generation in the relativistic limit, Nature physics 2 (7) (2006) 456–459.

[92] S. Kim, J. Jin, Y.-J. Kim, I.-Y. Park, Y. Kim, S.-W. Kim, High-harmonic generation by resonant plasmon field enhancement, Nature 453 (7196) (2008) 757–760.

[93] G. Vampa, B. Ghamsari, S. Siadat Mousavi, T. Hammond, A. Olivieri, E. Lisicka-Skrek, A. Y. Naumov, D. Villeneuve, A. Staudte, P. Berini, et al., Plasmon-enhanced high-harmonic generation from silicon, Nature Physics 13 (7) (2017) 659–662.

[94] L. Yue, M. B. Gaarde, Characterizing anomalous high-harmonic generation in solids, Phys. Rev. Lett. 130 (2023) 166903. doi:10.1103/PhysRevLett.130.166903.

URL https://link.aps.org/doi/10.1103/PhysRevLett.130.166903

[95] E. N. Osika, A. Chacón, L. Ortmann, N. Suárez, J. A. Pérez-Hernández, B. Szafran, M. F. Ciappina, F. Sols, A. S. Landsman, M. Lewenstein, Wannier-bloch approach to localization in high-harmonics generation in solids, Phys. Rev. X 7 (2017) 021017. doi:10.1103/PhysRevX.7.021017.

URL https://link.aps.org/doi/10.1103/PhysRevX.7.021017

[96] J. Li, J. Lu, A. Chew, S. Han, J. Li, Y. Wu, H. Wang, S. Ghimire, Z. Chang, Attosecond science based on high harmonic generation from gases and solids, Nature Communications 11 (1) (2020) 2748.

[97] M. Mrudul, N. Tancogne-Dejean, A. Rubio, G. Dixit, High-harmonic generation from

spin-polarised defects in solids, npj Computational Materials 6 (1) (2020) 10.

[98] O. Schubert, M. Hohenleutner, F. Langer, B. Urbanek, C. Lange, U. Huttner, D. Golde, T. Meier, M. Kira, S. W. Koch, et al., Sub-cycle control of terahertz high-harmonic generation by dynamical bloch oscillations, Nature photonics 8 (2) (2014) 119–123.

[99] S. Cha, M. Kim, Y. Kim, S. Choi, S. Kang, H. Kim, S. Yoon, G. Moon, T. Kim, Y. W. Lee, et al., Gate-tunable quantum pathways of high harmonic generation in graphene, Nature Communications 13 (1) (2022) 6630.

[100] H. K. Avetissian, G. F. Mkrtchian, A. Knorr, Efficient high-harmonic generation in graphene with two-color laser field at orthogonal polarization, Physical Review B 105 (19) (2022) 195405.

[101] M. Mrudul, G. Dixit, High-harmonic generation from monolayer and bilayer graphene, Physical Review B 103 (9) (2021) 094308.

[102] R. Zhou, T. Guo, L. Huang, K. Ullah, Engineering the harmonic generation in graphene, Materials Today Physics 23 (2022) 100649.

[103] C. Liu, Y. Zheng, Z. Zeng, R. Li, Polarization-resolved analysis of high-order harmonic generation in monolayer mos2, New Journal of Physics 22 (7) (2020) 073046.

[104] B. Avchyan, A. Ghazaryan, K. Sargsyan, K. V. Sedrakian, On laser-induced high-order wave mixing and harmonic generation in a graphene quantum dot, JETP Letters 116 (7) (2022) 428–435.

[105] X. Zhang, T. Zhu, H. Du, H.-G. Luo, J. van den Brink, R. Ray, Extended high-harmonic spectra through a cascade resonance in confined quantum systems, Phys.

Rev. Res. 4 (2022) 033026. doi:10.1103/PhysRevResearch.4.033026.
URL https://link.aps.org/doi/10.1103/PhysRevResearch.4.033026

[106] A. D. Güçlü, P. Potasz, M. Korkusinski, P. Hawrylak, et al., Graphene quantum dots, Springer, 2014.

[107] B. Avchyan, A. Ghazaryan, K. Sargsyan, K. V. Sedrakian, High harmonic generation in triangular graphene quantum dots, Journal of Experimental and Theoretical Physics 134 (2) (2022) 125–134.

[108] Y. Qin, X. Feng, Y. Liu, Nonlinear refractive index in rectangular graphene quantum dots, Applied Sciences 9 (2) (2019) 325.

[109] T. Brixner, G. Krampert, T. Pfeifer, R. Selle, G. Gerber, M. Wollenhaupt, O. Graefe, C. Horn, D. Liese, T. Baumert, Quantum control by ultrafast polarization shaping, Physical review letters 92 (20) (2004) 208301.

[110] S. Kerbstadt, L. Englert, T. Bayer, M. Wollenhaupt, Ultrashort polarization-tailored bichromatic fields, Journal of Modern Optics 64 (10-11) (2017) 1010–1025.

[111] N. Tancogne-Dejean, O. D. Mücke, F. X. Kärtner, A. Rubio, Ellipticity dependence of high-harmonic generation in solids originating from coupled intraband and interband dynamics, Nature communications 8 (1) (2017) 745.

[112] R. Cireasa, A. Boguslavskiy, B. Pons, M. Wong, D. Descamps, S. Petit, H. Ruf, N. Thiré, A. Ferré, J. Suarez, et al., Probing molecular chirality on a sub-femtosecond timescale, Nature Physics 11 (8) (2015) 654–658.

[113] G. Sansone, E. Benedetti, F. Calegari, C. Vozzi, L. Avaldi, R. Flammini, L. Poletto,

P. Villoresi, C. Altucci, R. Velotta, et al., Isolated single-cycle attosecond pulses, Science 314 (5798) (2006) 443–446.

[114] H. Mashiko, S. Gilbertson, C. Li, S. D. Khan, M. M. Shakya, E. Moon, Z. Chang, Double optical gating of high-order harmonic generation with carrier-envelope phase stabilized lasers, Physical review letters 100 (10) (2008) 103906.

[115] X. Feng, S. Gilbertson, H. Mashiko, H. Wang, S. D. Khan, M. Chini, Y. Wu, K. Zhao, Z. Chang, Generation of isolated attosecond pulses with 20 to 28 femtosecond lasers, Physical review letters 103 (18) (2009) 183901.

[116] B. Shan, S. Ghimire, Z. Chang, Effect of orbital symmetry on high-order harmonic generation from molecules, Physical Review A 69 (2) (2004) 021404.

[117] N. H. Burnett, C. Kan, P. B. Corkum, Ellipticity and polarization effects in harmonic generation in ionizing neon, Phys. Rev. A 51 (1995) R3418–R3421. doi:10.1103/PhysRevA.51.R3418.

URL https://link.aps.org/doi/10.1103/PhysRevA.51.R3418

[118] C. Liu, Y. Zheng, Z. Zeng, R. Li, Effect of elliptical polarization of driving field on high-order-harmonic generation in semiconductor zno, Phys. Rev. A 93 (2016) 043806. doi:10.1103/PhysRevA.93.043806.

URL https://link.aps.org/doi/10.1103/PhysRevA.93.043806

[119] Y. S. You, D. A. Reis, S. Ghimire, Anisotropic high-harmonic generation in bulk crystals, Nature physics 13 (4) (2017) 345–349.

[120] N. Yoshikawa, T. Tamaya, K. Tanaka, High-harmonic generation in graphene enhanced

by elliptically polarized light excitation, Science 356 (6339) (2017) 736–738.

[121] S. A. Sato, H. Hirori, Y. Sanari, Y. Kanemitsu, A. Rubio, High-order harmonic generation in graphene: Nonlinear coupling of intraband and interband transitions, Phys. Rev. B 103 (2021) L041408. doi:10.1103/PhysRevB.103.L041408.
URL https://link.aps.org/doi/10.1103/PhysRevB.103.L041408

[122] Z.-Y. Chen, R. Qin, Circularly polarized extreme ultraviolet high harmonic generation in graphene, Optics express 27 (3) (2019) 3761–3770.

[123] T. Tamaya, A. Ishikawa, T. Ogawa, K. Tanaka, Higher-order harmonic generation caused by elliptically polarized electric fields in solid-state materials, Phys. Rev. B 94 (2016) 241107. doi:10.1103/PhysRevB.94.241107.
URL https://link.aps.org/doi/10.1103/PhysRevB.94.241107

[124] M. D. Stoller, S. Park, Y. Zhu, J. An, R. S. Ruoff, Graphene-based ultracapacitors, Nano letters 8 (10) (2008) 3498–3502.

[125] C. H. Lui, L. Liu, K. F. Mak, G. W. Flynn, T. F. Heinz, Ultraflat graphene, Nature 462 (7271) (2009) 339–341.

[126] S. Manzeli, D. Ovchinnikov, D. Pasquier, O. V. Yazyev, A. Kis, 2d transition metal dichalcogenides, Nature Reviews Materials 2 (8) (2017) 1–15.

[127] Q. H. Wang, K. Kalantar-Zadeh, A. Kis, J. N. Coleman, M. S. Strano, Electronics and optoelectronics of two-dimensional transition metal dichalcogenides, Nature nanotechnology 7 (11) (2012) 699–712.

[128] W. Choi, N. Choudhary, G. H. Han, J. Park, D. Akinwande, Y. H. Lee, Recent de-

velopment of two-dimensional transition metal dichalcogenides and their applications, Materials Today 20 (3) (2017) 116–130.

[129] Y.-W. Son, M. L. Cohen, S. G. Louie, Energy gaps in graphene nanoribbons, Physical review letters 97 (21) (2006) 216803.

[130] B. Gerislioglu, A. Ahmadivand, N. Pala, Hybridized plasmons in graphene nanorings for extreme nonlinear optics, Optical Materials 73 (2017) 729–735.

[131] P. Tian, L. Tang, K. Teng, S. Lau, Graphene quantum dots from chemistry to applications, Materials today chemistry 10 (2018) 221–258.

[132] Y.-C. Lin, T. Björkman, H.-P. Komsa, P.-Y. Teng, C.-H. Yeh, F.-S. Huang, K.-H. Lin, J. Jadczak, Y.-S. Huang, P.-W. Chiu, et al., Three-fold rotational defects in two-dimensional transition metal dichalcogenides, Nature communications 6 (1) (2015) 6736.

[133] R. Lv, H. Terrones, A. L. Elias, N. Perea-Lopez, H. R. Gutierrez, E. Cruz-Silva, L. P. Rajukumar, M. S. Dresselhaus, M. Terrones, Two-dimensional transition metal dichalcogenides: Clusters, ribbons, sheets and more, Nano Today 10 (5) (2015) 559–592.

[134] X. Cao, C. Ding, C. Zhang, W. Gu, Y. Yan, X. Shi, Y. Xian, Transition metal dichalcogenide quantum dots: synthesis, photoluminescence and biological applications, Journal of materials chemistry B 6 (48) (2018) 8011–8036.

[135] J. Son, S. Lee, S. J. Kim, B. C. Park, H.-K. Lee, S. Kim, J. H. Kim, B. H. Hong, J. Hong, Hydrogenated monolayer graphene with reversible and tunable wide band

gap and its field-effect transistor, Nature communications 7 (1) (2016) 13261.

[136] Y. Zhang, T.-T. Tang, C. Girit, Z. Hao, M. C. Martin, A. Zettl, M. F. Crommie, Y. R. Shen, F. Wang, Direct observation of a widely tunable bandgap in bilayer graphene, Nature 459 (7248) (2009) 820–823.

[137] M. Y. Han, B. Özyilmaz, Y. Zhang, P. Kim, Energy band-gap engineering of graphene nanoribbons, Physical review letters 98 (20) (2007) 206805.

[138] Y. Yan, J. Chen, N. Li, J. Tian, K. Li, J. Jiang, J. Liu, Q. Tian, P. Chen, Systematic bandgap engineering of graphene quantum dots and applications for photocatalytic water splitting and co2 reduction, ACS nano 12 (4) (2018) 3523–3532.

[139] Z. Jin, P. Owour, S. Lei, L. Ge, Graphene, graphene quantum dots and their applications in optoelectronics, Current Opinion in Colloid & Interface Science 20 (5-6) (2015) 439–453.

[140] X. Yan, B. Li, X. Cui, Q. Wei, K. Tajima, L.-s. Li, Independent tuning of the band gap and redox potential of graphene quantum dots, The journal of physical chemistry letters 2 (10) (2011) 1119–1124.

[141] H. Avetissian, A. Ghazaryan, K. V. Sedrakian, G. Mkrtchian, Long-range correlation-induced effects at high-order harmonic generation on graphene quantum dots, Physical Review B 108 (16) (2023) 165410.

[142] T. Popmintchev, M.-C. Chen, D. Popmintchev, P. Arpin, S. Brown, S. Ališauskas, G. Andriukaitis, T. Balčiunas, O. D. Mücke, A. Pugzlys, et al., Bright coherent ultrahigh harmonics in the kev x-ray regime from mid-infrared femtosecond lasers, science

336 (6086) (2012) 1287–1291.

[143] D. G. Lee, J.-H. Kim, K.-H. Hong, C. H. Nam, Coherent control of high-order harmonics with chirped femtosecond laser pulses, Physical Review Letters 87 (24) (2001) 243902.

[144] W. Hayes, A. M. Stoneham, Defects and defect processes in nonmetallic solids, Courier Corporation, 2012.

[145] D. Rhodes, S. H. Chae, R. Ribeiro-Palau, J. Hone, Disorder in van der waals heterostructures of 2d materials, Nature materials 18 (6) (2019) 541–549.

[146] X. Zou, B. I. Yakobson, An open canvas 2d materials with defects, disorder, and functionality, Accounts of chemical research 48 (1) (2015) 73–80.

[147] S. M. Tan, M. Pumera, Two-dimensional materials on the rocks: Positive and negative role of dopants and impurities in electrochemistry, ACS nano 13 (3) (2019) 2681–2728.

[148] J. Jiang, T. Xu, J. Lu, L. Sun, Z. Ni, Defect engineering in 2d materials: precise manipulation and improved functionalities, Research (2019).

[149] J. Bardeen, W. H. Brattain, Physical principles involved in transistor action, Physical Review 75 (8) (1949) 1208.

[150] M. W. Doherty, N. B. Manson, P. Delaney, F. Jelezko, J. Wrachtrup, L. C. Hollenberg, The nitrogen-vacancy colour centre in diamond, Physics Reports 528 (1) (2013) 1–45.

[151] J. R. Maze, P. L. Stanwix, J. S. Hodges, S. Hong, J. M. Taylor, P. Cappellaro, L. Jiang, M. G. Dutt, E. Togan, A. Zibrov, et al., Nanoscale magnetic sensing with an individual electronic spin in diamond, Nature 455 (7213) (2008) 644–647.

[152] T. T. Tran, K. Bray, M. J. Ford, M. Toth, I. Aharonovich, Quantum emission from hexagonal boron nitride monolayers, Nature nanotechnology 11 (1) (2016) 37–41.

[153] S. Xu, J. Yu, C. Ye, H. Zhang, Z. Wang, J. Hu, The defect-state-assisted enhancement of high harmonic generation in bulk zno, Applied Physics Letters 122 (18) (2023).

[154] H. Avetissian, G. Musayelyan, G. Mkrtchian, Intense anomalous high harmonics in graphene quantum dots caused by disorder or vacancies, Physical Review B 109 (8) (2024) 085417.

[155] C. Yu, K. K. Hansen, L. B. Madsen, Enhanced high-order harmonic generation in donor-doped band-gap materials, Physical Review A 99 (1) (2019) 013435.

[156] S. Reich, C. Thomsen, J. Maultzsch, Carbon nanotubes: basic concepts and physical properties, John Wiley & Sons, 2008.